

Analysis of universal trap states in organic semiconductors

Von der Fakultät für Ingenieurwissenschaften,
Abteilung Elektrotechnik und Informationstechnik
der Universität Duisburg-Essen

zur Erlangung des akademischen Grades

Doktor der Ingenieurwissenschaften

genehmigte Dissertation

von

Karsten Rojek

aus Bremen

Gutachter: Prof. Dr.-Ing. Niels Benson

Gutachter: Prof. Dr. rer. nat. Gerd Bacher

Tag der Mündlichen Prüfung: 17.02.2021

Abstract

Organic semiconductors are promising materials for LEDs, solar cells, field-effect transistors or sensors. Although these materials have been studied thoroughly, a lack of understanding the origin of trap states prohibit the widespread use.

In recent years, trap states caused by oxygen and water are discussed to be universal for all organic semiconductors and the reason for lower electron mobility compared to holes. However, this assumption is based on simple voltage current measurements at unipolar devices and theoretical simulations. For the simplified description of the devices, a single trap level is assumed. Furthermore, a direct measurement of the energetic trap depth distribution is not done yet. Thus, it is still unclear, if these oxygen and water dependent universal trap states have a major influence on the charge carrier transport in organic semiconductors.

For the investigation of the universal trap states, a direct measurement of the unipolar energetic trap distribution is done in this thesis. For this purpose, the well-known thermally stimulated current method is modified by using a metal insulator semiconductor structure instead of a diode. The measured trap distributions are correlated to the charge carrier mobility determined with the transient space charge limited method. This method is challenging for semiconductor thin films because of the need for a low RC time constant for sample charging. A measurement circuit is developed here to improve the limits of this method by reducing this RC time constant. Additionally, a device simulation is done to analyze the physical limits of this method in terms of minimum measurable film thickness.

The well-known materials P3HT, PCPDTBT and MDMO-PPV in pristine and controlled aged (with oxygen and water) states are analyzed. The measurement of the unipolar trap distributions and charge carrier mobilities of these materials allows for analyzing the suggested universal trap levels and its influence on the charge carrier transport.

Contents

Contents	iii
Acknowledgments	vii
Publications	ix
1 Introduction	1
2 Theory	5
2.1 Charge carrier transport in organic semiconductors	5
2.1.1 Gaussian density of states	5
2.1.2 Hopping mobility	6
2.1.3 Trap states in organic semiconductors	7
2.1.4 Schottky contacts and surface potential	9
2.2 Thermally stimulated current (TSC)	9
2.2.1 Measurement principle for enveloping TSC	9
2.2.2 Trap filling	10
2.2.3 Heating procedure for enveloping TSC measurement	11
2.2.4 Heating procedure for fractional TSC measurement	11
2.2.5 Determining the total density of trap states	12
2.3 Space charge limited current (SCLC)	13
2.3.1 Ideal steady state SCLC	14
2.3.2 Ideal transient SCLC	16
2.3.3 Qualitative discussion of non-ideal device parameters influencing the space charge limited current	19
3 SCLC Simulation method	23
3.1 models	23
3.2 Device parameters	26
4 Materials and sample layout	31
4.1 Materials under examination	31
4.2 Structure for SCLC samples	32
4.2.1 Hole only devices	32
4.2.2 Electron only devices	33
4.3 Structure of TSC samples	34
4.3.1 Diode structure	35

4.3.2	Metal semiconductor insulator structure	35
4.4	Production procedures for samples	35
4.4.1	Spin coating processes	36
4.4.2	Evaporation processes	38
4.4.3	Aging of semiconductors	39
5	Measurement setups and procedures	41
5.1	Thickness measurement	41
5.2	Current- and capacitance-voltage measurements	41
5.3	TSC setup	42
6	Results	45
6.1	Thermally stimulated current method for unipolar measurements	45
6.1.1	MIS-TSC method	45
6.1.2	How trap states are filled during charging	46
6.1.3	Heating procedure and measuring the TSC	47
6.1.4	Measurement procedure for determining trap distributions	48
6.2	Verification of the MIS TSC principle	48
6.2.1	Analyzing substrate influences	48
6.2.2	Benchmarking the MIS-TSC method in comparison to the classical TSC method	49
6.2.3	Calcium passivation of SiO ₂	51
6.2.4	Fractional MIS-TSC	52
6.2.5	Dependence of TSC on the charging procedure	55
6.3	Transient SCLC measurement circuit	57
6.3.1	Details of the voltage step generation circuit part	60
6.3.2	Details of the sample connection circuit part	61
6.3.3	Details of the current measurement circuit part	62
6.4	Benchmarking of the transient SCLC circuit	64
6.4.1	Mobility from steady state SCLC	64
6.4.2	Transient SCLC measurement procedure	65
6.4.3	Mobility results from transient SCLC measurements of MTDATA	68
6.4.4	Measurement range of the transient SCLC circuit	70
6.5	Simulation of space charge limited current	71
6.5.1	Steady state and transient SCLC in the basic device	71
6.5.2	Influence of doping and parallel current paths on the transient SCLC mobility	74
6.5.3	Influence of built-in field on transient SCLC	75
6.5.4	Influence of injection barrier on transient SCLC	76
6.5.5	Influence of a non-ideal voltage step on the transient SCLC mobility	77
6.6	Analysis of universal trap levels	82
6.6.1	Difference of electron and hole mobility in pristine semiconductors	83
6.6.2	MIS-TSC Measurements	84
6.6.3	Analysis of SCLC measurements	89

6.6.4	Correlation of trap distribution and mobility	94
7	Summary	97
8	Appendix	101
8.1	Theory: Equations for electrons	101
8.2	Details of sample layout, sample production and materials	103
8.3	Details of the SCLC simulation	108
8.3.1	Atlas program code	109
8.3.2	Algorithm for finding transient peak	116
8.3.3	Algorithm for fitting the simulated normalized mobility	117
8.4	Details of the SCLC measurement and control circuits	118
8.5	FFT filter for smoothing of the transient SCLC signal	123
8.6	Enveloping TSC of PCPDTBT/ MDMO-PPV and original fractional TSC signals	125
8.7	Appendix SCLC results	128
8.7.1	Fits for mobility values determined with the transient SCLC method	128
8.7.2	Original SCLC measurement results of PCPDTBT and MDMO- PPV without normalization	129
	Abbreviations and variables	133
	List of Figures	141
	List of Tables	145
	Bibliography	147

Acknowledgments

At first, I thank my Ph. D. supervisor Niels Benson for the opportunity of doing my Ph. D. and his help in the research and writing. Special thanks also to Roland Schmechel for the chance to work in his group "Institute of Technology for Nanostructures", his ideas when I had problems in my experiments and critical reviews. Additionally, I thank Gerd Bacher for his willingness to be the second assessor and his review of my thesis.

Furthermore, I thank all my colleagues in the group for the scientific discussions and for the nice working atmosphere including a lot of fun. In this context I would like to highlight my Ph. D. colleagues Damian Pandel, Fabian Langer, Franziska Maculewicz, Julia Stötzel, Julian Neises, Laura Kühnel and Svetlana Sirotinskaya. It was nice working together with you in the lab. Also thanks to Miriam Engel for her job training at the beginning of the project in the context of organic semiconductors.

An experimental Ph. D. is not possible without the help of other specialists from different fields. Andreas Trampe helped me a lot with the development of the measurement circuit. Felix Bense did much work for developing and installing the measurement boxes and setups. Martin Dehnen had always ideas in case of chemical process problems and generally, without him, the lab wouldn't work at all. Dagma Kamin-Düster, Heidi Giesen and Nadine Abbing helped me with all administrative challenges, which sometimes seem more difficult than the research. I thank all of you, as without you, the research would not be possible.

To get a result in the context of this project, a lot of experimental work was necessary. I got a lot of help from students here. Ali Salehi Sadaghiani and Damian Pandel did experiments as research assistants. James Souverain and Liu Tong did their Bachelor theses in the context of my Ph. D. project and found helpful results for processing samples. Again, thank you for your help.

Doing a Ph. D. is a lot of work and stress and needs a lot of social backup. Here, I thank my family and friends for their assistance and their understanding when I had no time for them. Especially, I thank Anja Budde for her support during the hardest times of my Ph. D. in the final stage, where great changes happen in the private life.

Publications

The following publications (also listed in the bibliography) were done in the context of this Ph. D. project:

”MIS-TSC: A combination of the thermally stimulated current method and a metal-insulator-semiconductor device for unipolar trap spectroscopy” [132]

Citation: *K. Rojek, R. Schmechel, N. Benson; Appl. Phys. Lett. 114, 152104 (2019)*

Submitted: *31 January 2019*

Accepted: *03 April 2019*

”Ultra-fast measurement circuit for transient space charge limited current in organic semiconductor thin films” [133]

Citation: *K. Rojek, R. Schmechel, N. Benson; 2020 Meas. Sci. Technol. 31 015901*

Submitted: *18 April 2019*

Accepted: *14 August 2019*

And the conference contribution:

”Ultra-fast measurement circuit for transient space charge limited current in organic semiconductor thin films”

conference: *EMRS 2018, Spring Meeting*

date: *18 - 22 June 2018*

1 Introduction

Organic semiconductors, which are conjugated small molecules or conjugated polymers, are widely used as active materials for organic light emitting diodes (OLED) in the display technology. Furthermore, they are promising materials for solar cells, field-effect transistors (FETs) or sensors [26, 64, 134, 139, 158, 159, 163]. Although organic semiconductors have been studied thoroughly, the wide use in these devices is still not accomplished. This is primarily caused by the lack of understanding degradation processes. The charge carrier trap states resulting from degradation significantly decrease the performance of organic devices [25, 112, 183]. E. g., trap states cause non radiative recombination (Shockley–Read–Hall recombination) which decreases the quantum efficiency of OLEDs [23, 90, 151]. Another effect of trap states is the reduction of the charge carrier mobility. Especially, the generally lower mobility of electrons compared to holes is a challenge [25, 112, 179]. E. g. for OLEDs, the imbalance of carrier mobilities is another major cause for a low quantum efficiency [160].

The reason for degradation, hence the origin of trap states can be multifaceted, but oxygen and water are discussed to be main causes [88, 114, 115]. In recent years, trap states caused by oxygen and water are discussed to be material independent. Thus, they are potential universal trap states for all materials. In this respect, Nicolai et al. [112] suggested oxygen containing functional groups at the molecules as universal origin for electron trap states, causing the lower mobility of electrons (compared to holes [102]) in organic semiconductors. They found an electron trap level at -3.6 eV below vacuum level for many different polymers. In contrast, Zuo et al. [183] suggested the incorporation of water molecules to be the cause for universal trap states. In their argumentation, the dipole of a water molecule shifts the next neighbor orbitals in direction of the Fermi level, creating a trap level 0.3 eV below the lowest unoccupied molecular orbital (LUMO) or above the highest occupied molecular orbital (HOMO). This effect would be similar for electrons and holes, thus it is no explanation for the lower electron mobility.

Nicolai et al. as well as Zuo et al. used voltage current measurements at unipolar devices combined with simulations to analyze the energetic depth of trap states indi-

rectly. A direct measurement of the energetic trap depth is not done yet in this context. Furthermore, only pristine materials are investigated without controlled generation of oxygen and water dependent trap states in the organic semiconductors. Thus, it is still unclear if the suggested universal trap states are the cause for the degradation of organic semiconductors and for the lower electron mobility. For clarification, a direct measurement of the unipolar energetic trap distribution of pristine and aged materials is done in this thesis. To correlate these energetic trap distributions to the charge carrier mobility, the unipolar mobility of the same materials is determined. Thus, it is investigated, if the universal trap states are the origin for the generally lower electron mobility.

For analyzing whether the determined trap states are potentially universal for all materials, three well-known polymers are investigated here:

- *Poly(3-hexylthiophene-2,5-diyl)* (P3HT),
- *Poly[2,6-(4,4-bis-(2-ethylhexyl)-4H-cyclopenta[2,1-b;3,4-b']dithiophene)-alt-4,7(2,1,3-benzothiadiazole)]* (PCPDTBT) and
- *Poly[2-methoxy-5-(3',7'-dimethyloctyloxy)-1,4-phenylenevinylene]* (MDMO-PPV).

P3HT is a well-known organic semiconductor, which is often used as reference material as it is done here [121, 124, 140]. The other two polymers are investigated as example materials used in current device research. In this respect, PCPDTBT got much interest in organic solar cells in recent years [70, 87, 109] and different PPV derivatives are often used in OLEDs. As a well-known PPV, MDMO-PPV is used here [6, 72, 125].

Furthermore, controlled aging of these materials is done in this thesis. With the exposure to oxygen and water as well as UV light, additional trap states are introduced into the materials by photo oxidation [68, 101, 140]. With these aging treatments, oxygen and water as the origin of trap states are investigated.

For the purpose of directly measuring the energetic distribution of trap levels, the well known thermally stimulated current (TSC) method is applied [17, 33, 150]. Although the classical TSC method has the advantage of the direct measurement of the activation energy for exciting trapped charge carriers, which is assigned to the energetic trap depth, it implies challenges. The classical measurement of a bipolar diode does not avoid recombination of complementary charge carriers, which falsifies the activation energy and trap level distribution information [14, 17]. Additionally, the unipolar evaluation of electron and hole trap states is not possible without further analysis. However, this aspect is crucial to analyze the influence of trap states on the charge carrier mobility. To overcome this challenge, a modification of the TSC method is developed in this thesis. This modification is the use of a metal insulator semiconductor (MIS) device

structure instead of the diode (MIS-TSC method). As the semiconductor can be unipolar charged by choosing the direction of the charging voltage, the MIS-TSC method allows for unipolar trap occupation and subsequent measurement. Furthermore, recombination of complementary charge carriers is avoided [132].

Additionally, the mobility of electrons and holes has to be measured for correlation between trap states and mobility differences in dependence of aging. Preferably, the measurement direction should be in line with the current direction in typical device architectures. For e. g. OLEDs or solar cells, this is perpendicular to thin films. Consequently, the field- or Hall-effect methods [76, 105, 123], which are often used for mobility determination, are not applicable as the measurement in the device plane might cause false results. Alternatives with a perpendicular measurement direction are the time of flight (ToF) [89] or space charge limited current (SCLC) methods [22, 59, 89, 95]. In case of ToF, the measured currents are small compared to typical device currents, which influences the mobility, as the mobility in organic semiconductors depends on the charge carrier density [11]. Furthermore, there are high requirements for the sample structure to ensure efficient light incorporation. In contrast, the SCLC method is an appropriate choice as high current densities are required and the sample structure is simpler [1, 22]. For SCLC, there is the steady state and transient method. The steady state SCLC method lacks of precision and the correct data analysis is difficult [22]. Thus, this method is only usable for the determination of reference values. In contrast, the transient SCLC method has a higher accuracy [1]. A major challenge for the transient SCLC method is the required low RC time constant for device charging.

As the reduction of sample capacitance is technologically limited in case of organic thin films [62], the crucial challenge for using the transient SCLC method is the minimization of the serial resistance to the device under test. To overcome this problem, a measurement circuit for fast sample charging is developed here. However, the influences of non-ideal device parameters become prominent for semiconductor thin films. For investigation of these non-ideal influences, e. g. build-in field or injection barrier, a transient SCLC simulation addressing these issues is done in this thesis.

In conclusion, the correlation of trap distribution and mobility information of three different organic polymer semiconductors is used in this thesis to investigate the origin of low electron mobility compared to hole mobility. Furthermore, for analyzing degraded polymers, the materials are exposed to oxygen, water and UV light. This allows for correlation between degradation causes and reduced mobility as well as for investigating the suggested universal trap states.

2 Theory

2.1 Charge carrier transport in organic semiconductors

Organic semiconductors are polymers or small molecules with double covalent bonds between carbon atoms, which are sp^2 -hybridized [142]. These bonds consist of strong σ bonds and weaker π bonds. The π bonds form transport states on a molecule [26]. These are localized states in the semiconductor bulk and the charge carrier transport between molecules is possible via hopping [156]. This hopping process describes the tunneling of charge carriers between the localized states of two molecules [26]. The transport states in organic semiconductors are subdivided into the highest occupied molecular orbital (HOMO) for holes and the lowest unoccupied molecular orbital (LUMO) for electrons. These orbitals are often seen as the equivalent to valence band and conduction band in inorganic semiconductors [152]. In the following, the HOMO and LUMO (Chap. 2.1.1) states as well as the hopping process (Chap. 2.1.2) are discussed in more detail. Furthermore, the influence of trap states on the charge carrier transport is discussed in chapter 2.1.3 [94, 122, 153] and the contacts to organic layers in chapter 2.1.4 [26].

2.1.1 Gaussian density of states

The transport states (HOMO and LUMO) are distributed over the energy, which is caused by structural disorder within organic semiconductors [26, 183]. This energy distribution of the density of states (DOS) can be assumed to be of Gaussian shape [13, 31, 119, 164]. Often, an exponential tail is assumed for the Gauss profile, which accounts for e. g. doping [111, 183]. However, in case of high charge carrier density, the influence of this tail is neglectable for charge carrier transport analyses. As the tail states are completely filled, hopping is impossible at this energy because of the absence of free transport states [15]. This high charge carrier density is a crucial assumption for the space charge limited current (SCLC) concept used in this thesis (Chap. 2.3). Thus, the assumption of a Gauss profile for the DOS is reasonable here. Equation 2.1 describes this DOS ($g(E)$), where N is the total number of available states, σ the width of the

Gaussian profile and E the energy. Here, $E = 0$ eV is the center of the profile. As a material parameter, this center is the HOMO or LUMO level.

$$g(E) = \frac{N}{\sqrt{2\pi} \cdot \sigma} \cdot e^{-\frac{(E)^2}{2\sigma^2}} \quad (2.1)$$

The occupation probability f_{fd} of free states at E is given by the Fermi-Dirac relation (Equ. 2.2) with E_F as the Fermi level, k_B as the Boltzmann constant and T as the temperature [111]. At non-equilibrium, e. g. in case of an applied voltage, E_F can be replaced by the quasi Fermi levels for electrons and holes [26]. These describe the occupation probability for the HOMO and LUMO levels separately, accounting for the non-equilibrium. The density of occupied states is given by $f_{fd}(E) \cdot g(E)$.

$$f_{fd}(E) = \left(1 + e^{\frac{E - E_F}{k_B T}} \right)^{-1} \quad (2.2)$$

2.1.2 Hopping mobility

The tunneling probability of charge carriers between one occupied and one empty localized state depends on the energetic difference of and distance between those states. As a tunneling process is isoenergetic, a phonon has to be involved in the tunneling process to compensate for an energetic difference [69, 172].

For the purpose of simpler description of the charge transport via hopping, an effective transport energy E_{tr} can be defined [11, 18]. The assumption for this concept is, that a charge carrier at or above E_{tr} will hop to the next empty state immediately. In this case, the probability that there is at least one free adjacent state at or below E_{tr} (nearer to E_F) has to be 1 [83]. The target free state has to be within the localization radius γ which is the decay length of the wave function of the localized charge carrier [106]. For these assumptions, E_{tr} can be derived with equation 2.3 [116], with the DOS $g(E)$ (Chap. 2.1.1). As high charge carrier densities are given for SCLC methods, equation 2.3 do account for occupied states and only free states are considered as target [11].

$$\int_{-\infty}^{E_{tr}} \frac{g(E') \cdot (E_{tr} - E')^3}{1 + e^{-\frac{E' - E_F}{k_B T}}} dE' = \frac{6}{\pi} \cdot (\gamma \cdot k_B T)^3 \quad (2.3)$$

Because of the energetic difference of occupied and unoccupied state, a hopping event is triggered by a phonon. Therefore, the attempt to jump frequency f_{atj} is equal to the phonon frequency and the mobility μ is proportional to f_{atj} (Equ. 2.4) [11]. Furthermore, μ depends on the distance to the target state and on the necessary activation energy, which is the difference between the current energy of a charge carrier and E_{tr} . The charge carrier density η can either be the hole or electron density.

$$\mu = \underbrace{\frac{q \cdot f_{atj}}{\eta k_B T}}_{\text{frequency}} \cdot \underbrace{\left(\int_{-\infty}^{E_{tr}} g(E') dE' \right)^{-\frac{2}{3}}}_{\text{jump distance}} \cdot \underbrace{\int_{-\infty}^{E_{tr}} \frac{g(E') \cdot e^{\frac{E' - E_{tr}}{k_B T}}}{1 + e^{-\frac{E' - E_F}{k_B T}}} dE'}_{\text{activation energy}} \quad (2.4)$$

2.1.3 Trap states in organic semiconductors

Trap states have a significant influence on the charge carrier transport and device performance. For inorganic semiconductors, a trap state is described as a localized state within the band gap. In contrast, the exact definition of a band gap is difficult for organic semiconductors, because of the Gaussian DOS. Furthermore, distinguishing between transport and trap states is not trivial, as all states are localized [75].

With the assumption of the effective transport energy, the states below this energy can be related to trap states. This means, organic semiconductors have intrinsically shallow trap states [175] and for each hopping event, a charge carrier has to be thermally excited. Deeper trap states will trap charge carriers for a longer time period as the probability of sufficient thermal excitation is lower compared to shallow trap states.

The origin of trap states within organic semiconductors can be intrinsic, which means dependent on the molecular states or semiconductor microstructure, or can be caused by impurities or chemical defects within the molecules [112, 168, 183]. For different materials, contaminants like unwanted molecules would have the same energetic depth in respect to the vacuum level, which can also be true for unwanted functional groups at the molecules [112, 114, 168]. However, there might be different contaminants present in the polymers depending on the production process. Furthermore, the interaction with other materials at interfaces may lead to defect states [101, 114, 141, 155].

In this context, water and oxygen are discussed to be the origin of universal trap states present in all organic materials. Nicolai et al. [112] suggested oxygen dependent functional groups (e. g. carbonyl or hydroxyl groups) on the organic molecule as the origin for universal trap states. Thy argument, that the electron affinity of these groups

Table 2.1: Proposed relative trap levels (energetic distance to HOMO or LUMO) by Nicolai et al. [112] (oxygen trap) and Zuo et al. [183] (water trap) for the investigated polymers in this thesis (Chap. 4.1).

material	water trap (h+)	water trap (e-)	oxygen trap (e-)
P3HT	0.15 eV	0.4 eV	0.6 eV
PCPDTBT	0.4 eV	0.32 eV	0.1 eV
MDMO-PPV			0.6 eV

is not significantly influenced by the organic molecule. Consequently, these groups form a universal electron trap at -3.6 eV in reference to the vacuum level. Thus, the relative depth depends on the LUMO level.

Zuo et al. [183] did a similar argumentation. Here, water molecules are incorporated into the organic semiconductor. The dipole of a water molecule causes an energetic shift of the HOMO and LUMO of the nearest neighbors of the water molecule, as confirmed by Nikolka et al. [114]. This shift is in direction of the Fermi level and causes both hole and electron trap states with a relative depth of 0.3 eV to 0.4 eV compared to the HOMO or LUMO level. Additionally, the auto ionization of water molecules may lead to different dipoles and hence to a different trap depth [114].

The relative trap depths for the polymers investigated in this thesis (Chap. 4.1) are summarized in table 2.1 as determined by Nicolai et al. (called oxygen trap in the following) and Zuo et al. (called water trap in the following). Here, the trap depth is assumed to be the activation energy E_a needed to excite a trapped charge carrier from this trap [73, 81]. However, for organic semiconductors, the trap depth can be influenced by e. g. coulomb interaction [126, 151, 167]. Nikitenko et al. discussed this issue and concluded, that in case of unipolar trap filling the differences in trap depth can be neglected [113]. Consequently, as the MIS-TSC used in this thesis is unipolar, E_a is used here as characteristic value of the trap depth.

2.1.4 Schottky contacts and surface potential

The contacts to an organic semiconductor can be described by Schottky contacts [127]. The surface potential Ψ_S is defined in equation 2.5 and depends on the electron affinity of the contact metal E_{aff} , the energetic distance between HOMO and LUMO E_g , the work function of the semiconductor W and the applied voltage V (q is the elementary charge). The surface potential defines the amount of charge carriers at the semiconductor/ metal interface, which results in space charge regions at the contacts [152].

$$\Psi_S = E_{aff} + \frac{E_g}{2q} - W - V \cdot q \quad (2.5)$$

2.2 Thermally stimulated current (TSC)

For the determination of the density of trap states and its energetic distribution, the thermally stimulated current (TSC) method is applied in this thesis [17, 33, 150]. This method is generally used for the characterization of semiconductors, both inorganic [166, 177], organic [86, 149] and hybrid materials like e.g. perovskites [170]. Classically, the method is applied using bipolar diode structures [14, 17]. The challenge for this classical method is the bipolar nature of the diode. For this device structure, recombination of complementary charge carriers influences the measurement and the unipolar trap depth determination is not possible without further analyses.

The principle of this method is the optical or electrical trap filling during sample cool down or at a constant low temperature and subsequent heating of the device under test after the trap filling. During heating, trapped charge carriers are thermally excited, which results in a temperature dependent current. This current is related to the amount of occupied trap states and their energetic depth.

2.2.1 Measurement principle for enveloping TSC

Only the electrical filling process is described here, although it is also possible with light [17, 83, 138]. Figure 2.1 shows the schematic sequence. At first, the trap states of the semiconductor under test are filled during cool down. The semiconductor is charged by a constant charging voltage V_{ch} at room temperature in forward bias, causing a high current density. The physics of trap filling is discussed in chapter 2.2.2. The charging voltage is applied a time span Δt_1 before start of the cool down with the rate β (Equ. 2.6).

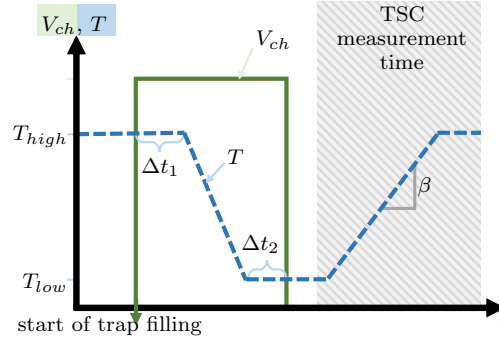


Figure 2.1: Schematic timing diagram of the enveloping TSC measurement sequence.

$$\beta = \frac{T_{end} - T_{start}}{t} \quad (2.6)$$

The charging voltage is applied until the temperature reaches the minimum temperature T_{low} and during another span of time Δt_2 . Then, the device under test is put into a short circuit. For the extraction of free excess charge carriers which are not trapped, the temperature is kept constant until the current is ideally zero. Practically, the current is below the noise level. Subsequently, the temperature is increased with a constant β and the TSC is measured as described further in chapter 2.2.3. Reaching room temperature, the current is measured until it is below noise level, meaning that all trap states are empty. The described measurement sequence is called enveloping measurement.

2.2.2 Trap filling

The measured TSC is strongly dependent on the effectiveness of the charging procedure, meaning the percentage of occupied in relation to the total amount of trap states after charging. In case of a diode, a constant current is flowing through the device, resulting in a high density of free charge carriers. The amount of free charge carriers is limited by the maximum applicable voltage without breaking the device. The trap occupation depends on the equilibrium of newly trapped and thermally freed charge carriers [17]. This equilibrium shifts to higher trap occupation during cooling. Additionally, the trap filling depends on the mobility of free charge carriers in the sense, that an unoccupied trap has to be found by a free charge carrier. As the mobility decreases with temperature, this process becomes ineffective. Therefore, the trap filling is more efficient if the charging voltage is applied during cool down compared to charging only at low temperature.

2.2.3 Heating procedure for enveloping TSC measurement

The device under test is kept in short circuit condition during heating for the enveloping TSC measurement. Within the diode structure, the build-in field will cause the charge carrier extraction [17, 33, 150].

Before heating, a sufficient time span has to be waited until free excess charge carriers are extracted and the measured current is ideally zero. Otherwise, this charge will be extracted during heating which falsifies the TSC signal. In praxis, a leakage current will remain caused by the burden voltage of the used electrometer. This leakage current increases with temperature, as the mobility and thus the conductivity of the semiconductor under test increases (Chap. 2.1.2).

During heating, trapped charge carriers are thermally excited causing current peaks if plotted over the temperature. The initial rise of the resulting TSC (I_{TSC}) peak depends on the activation energy E_a as in equation 2.7, where T is the temperature and k_B is the Boltzmann constant [33, 73, 78, 150]. The energy needed to excite a trapped charge carrier is equal to E_a (Chap. 2.1.3). With the assumption of neglectable retrapping, recombination as well as a single trap level, E_a can be determined with a linear regression on the slope of $\ln(I_{TSC})$ over $\frac{1}{T}$.

$$I_{TSC} \propto e^{\frac{-E_a}{k_B T}} \quad (2.7)$$

For the practical measurement, a time delay before the ejection of excited charge carriers has to be considered. This delay is caused by the charge carrier mobility and retrapping. Consequently, higher β will cause a shift of a TSC signal peak to higher temperatures. Simultaneously, there is an increase of the peak, as the same amount of charge is extracted over a shorter time period. In consideration of an appropriate β , there is the advantage of an improved signal to noise ratio in case of high β . In contrast, the disadvantage is a worse resolution of multiple and overlapping TSC peaks.

2.2.4 Heating procedure for fractional TSC measurement

Multiple TSC peaks are the result trap states with an energetic distribution (Chap. 2.1.3). This distribution can be determined with the fractional method [33, 73, 150], which differs from the enveloping measurement only by the heating process. For the fractional TSC method, multiple subsequent heating and cooling steps are used, which have the

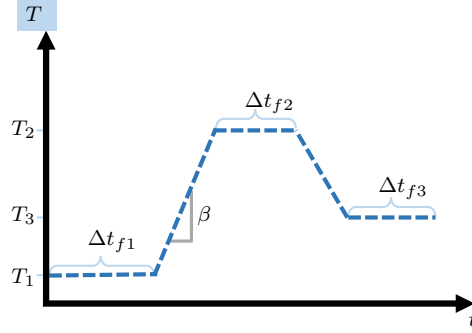


Figure 2.2: Schematic timing diagram of the fractional TSC measurement sequence

same β . This is described schematically in figure 2.2, where the starting temperature T_1 is the end temperature T_3 of the sequence before.

With the fractional method, the TSC signal of one temperature sequence ($T_2 - T_1$) can be related to a single trap level, as only a small range of the trap distribution is analyzed. Thus, equation 2.7 can be applied to calculate this trap level. For extraction of all charges of this trap level, the time span Δt_{f2} must be long enough that I_{TSC} drops down to noise level when the temperature is at T_2 . The time spans Δt_{f1} and Δt_{f3} are necessary for temperature stabilization. The resolution of the determined density of trap states by this method is therefore depending on the magnitude of $T_2 - T_1$.

2.2.5 Determining the total density of trap states

The integration of I_{TSC} over time t gives the total extracted charge which resembles the number of occupied trap states $N_{trap,occ}$ with the assumption that all trap states will be emptied during heating [24]. This assumption is valid, as permanently occupied trap states can not trap free charge carriers and do not influence the charge carrier mobility. Consequently, the trap filling probability during charging (Chap. 2.2.2) defines $N_{trap,occ}$.

The density of occupied trap states $n_{trap,occ}$ is calculated with equation 2.8 [78]. Here, V_{vol} is the volume of the device under test and q the elementary charge. Practically, the integration is done from the time when I_{TSC} rises above noise level until it dropped back below noise level.

$$n_{trap,occ} = \frac{N_{trap,occ}}{V_{vol}} = \frac{1}{qV_{vol}} \cdot \int_0^{\infty} I_{TSC} dt \quad (2.8)$$

2.3 Space charge limited current (SCLC)

This chapter explains the theoretical concept of space charge limited current (SCLC), which is generally valid for all types of semiconductors. Starting with the general charge carrier transport within a semiconductor bulk, the conductivity depends on the charge carrier density (n for electrons and p for holes) and the charge carrier mobility μ (μ_n for electrons and μ_p for holes). The mobility is defined as the proportionality factor between the electric field strength F and the drift velocity v_{drift} (Equ. 2.9) [152].

$$v_{drift} = \mu \cdot F \quad (2.9)$$

The drift velocity is the average velocity of a charge carrier package moving through the semiconductor. The total current can be considered as a superposition of hole and electron current, thus the total specific conductivity σ_c is the superposition of both carrier types (Equ. 2.10) [152]. Here, q is the elementary charge.

$$\sigma_c = q(\mu_n n + \mu_p p) \quad (2.10)$$

By ohm's law, σ_c is the proportionality factor between the current density J and F (Equ. 2.11).

$$J = \sigma_c \cdot F \quad (2.11)$$

For a better understanding of the SCLC, the ideal theory is described in the following. The influences of non-ideal device parameters are discussed afterwards in chapter 2.3.3. Assuming ideal SCLC, there is one ideal injecting contact for majority charge carriers and one ideal blocking contact for minority charge carriers. Further assumptions for the ideal case are [22, 82, 120, 154]:

- There are no contact resistances.
- The device is unipolar and symmetric because of zero work function difference of the contacts.
- Consequently, there is no build-in field.
- Serial or parallel resistances are neglectable in comparison to the device resistance.

- The electric field strength and charge carrier density do not influence the mobility.
- The semiconductor is trap free.
- No doping and intrinsic charge carriers are only present due to thermal activation.

Consequently, it is sufficient to use only one term in equation 2.10. In the following, the equations for hole only devices are discussed. The equations for electron only devices are equivalent and given in the appendix (App. 8.1).

By applying a bias voltage on the unipolar device, charge carriers are injected additionally to the intrinsic charge carriers. In case of low bias voltage, the current is ohmic, as the amount of intrinsic charge carriers is larger than the amount of injected charge carriers. If the voltage is increased, the amount of intrinsic charge carriers can be neglected as it is significantly exceeded by the amount of injected charge carriers. This exceeding marks the beginning of the SCLC in terms of minimum bias voltage and the charge carrier density becomes dependent on F . For explanation of this dependents, a simplified picture of the semiconductor device as a capacitor is usable, where the number of introduced charges is proportional to F [144]. Consequently, from equation 2.10, σ_c is proportional to F which leads to equation 2.12.

$$J = q \cdot \mu_p \cdot p(F) \cdot F \propto q \cdot \mu_p \cdot F^2 \quad (2.12)$$

Generally, the SCLC can be measured either in steady state or transient mode. The steady state describes a current density-voltage (JV) curve and the transient method is a time dependent measurement of the current after applying a voltage step. The ideal assumptions, as listed before, are valid for both methods, which are described in the following chapters for hole only devices.

2.3.1 Ideal steady state SCLC

The current density J in the ideal steady state SCLC case depends on F^2 as described in equation 2.12. To calculate the analytical solution of the function $J(F)$, the Gauss relation in equation 2.13 and equation 2.14 result in the differential equation 2.15 [92]. Here, $\epsilon = \epsilon_0 \epsilon_r$ is the specific electric permittivity (ϵ_0 is the vacuum permittivity and ϵ_r the relative permittivity) and d the semiconductor thickness.

$$\eta(x) = \frac{\epsilon}{q} \cdot \frac{dF(x)}{dx} \quad (2.13)$$

$$J = q\mu\eta(x) \cdot F(x) \quad (2.14)$$

$$\frac{J}{\epsilon\mu} = F(x) \cdot \frac{dF(x)}{dx} \quad (2.15)$$

The solution for this differential equation is given in equation 2.16, where the boundary condition is $F(0) = 0$ (no contact resistance). Integrating this equation from 0 to d , the Mott-Gurney law results (Equ. 2.17) [92, 107].

$$F(x) = \sqrt{\frac{2J}{\epsilon\mu}} \quad (2.16)$$

$$J = \frac{9}{8} \frac{\epsilon}{d} \mu_p F(x)^2 \quad (2.17)$$

For a better understanding of equation 2.17, the device under test is considered as a capacitance and the charge within the semiconductor can be estimated with equation 2.18. In contrast to a capacitor, the charge is distributed over the semiconductor bulk. Thus, the effective thickness for the device capacitance is lower compared to d and the magnitude of the injected charge into the semiconductor is higher than in case of the capacitance [92].

$$C = \epsilon \cdot \frac{A}{d} \quad (2.18)$$

The injected charge into the semiconductor is higher than in case of the capacitance by the factor $9/8$ (Equ. 2.17). In equation 2.17, the term $\epsilon_0\epsilon_r/d$ is the capacitance per area. This capacitance multiplied with F replaces the charge $q \cdot p$ of equation 2.10.

In conclusion, if ϵ_r and the device geometry is known, equation 2.17 can be used to calculate the mobility from a JV curve. As an example JV curve, figure 2.3 shows a simulated JV curve (as described in chapter 3) in a linear and a double logarithmic plot. From the latter curve, the double logarithmic slope w (called "slope" in the following)

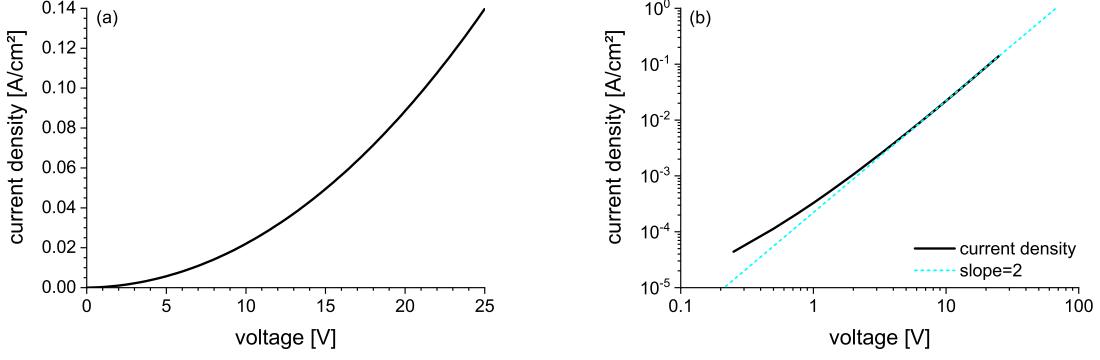


Figure 2.3: Ideal JV curve of steady state SCLC in (a) linear and (b) double logarithmic form. The data is simulated as described in chapter 3.2 for a 500 nm thick organic semiconductor with $f_{atj} = 1 \cdot 10^{12}$ Hz.

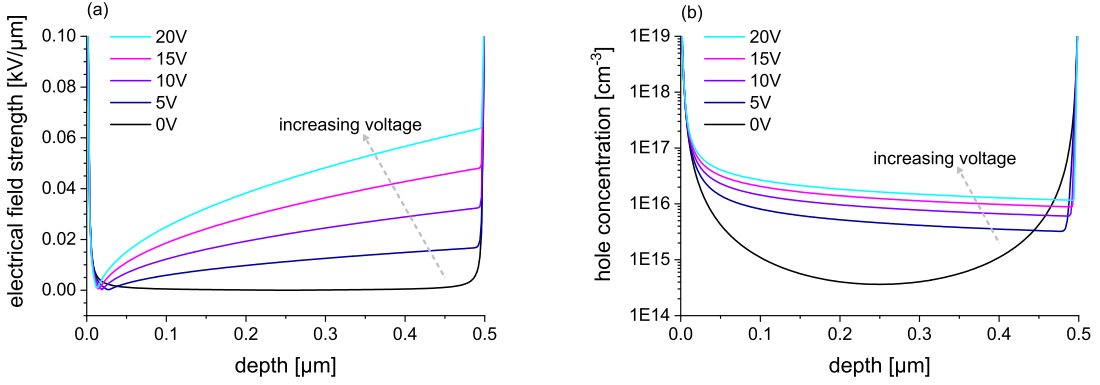


Figure 2.4: For steady state SCLC: (a) Ideal electric field strength and (b) distribution of charge carriers within the device for different applied voltages. The charge injecting contact is on the left side. The data is simulated as described in chapter 3.2 for a 500 nm thick organic semiconductor with $f_{atj} = 1 \cdot 10^{12}$ Hz.

can be determined. Ideally, $w = 2$ is valid as marked in figure 2.3b.

For the SCLC mode, the charge distribution and the electrical field strength is inhomogeneous over the semiconductor thickness [92], which is illustrated in figure 2.4. This is caused by the turn on process, as described in chapter 2.3.2

2.3.2 Ideal transient SCLC

For the transient SCLC measurement procedure, a voltage step from zero to V_S is applied to the unipolar device. For determining the transit time of the first injected charge carriers, the following derivation is done. Generally, for each point x in the depth of the semiconductor layer, the time dependent current density is the sum of displacement

($j_{displ}(x, t)$) and drift ($j_{drift}(x, t)$) current density as in equation 2.19. With the time dependent Gauss relation (Equ. 2.20), equation 2.21 results. Here, the chain rule is used for $\frac{dF^2(x, t)}{2dx} = F(x, t) \cdot \frac{dF(x, t)}{dx}$.

$$j(t) = j_{drift}(x, t) + j_{displ}(x, t) = q\eta(x, t)\mu F(x, t) + \epsilon \frac{dF(x, t)}{dt} \quad (2.19)$$

$$\epsilon \frac{dF(x, t)}{dx} = q\eta(x, t) \quad (2.20)$$

$$j(t) = \epsilon \left(\frac{\mu}{2} \cdot \frac{dF^2(x, t)}{dx} + \frac{dF(x, t)}{dt} \right) \quad (2.21)$$

Now, equation 2.21 is integrated over the total thickness d with the integrated Gauss relation in equation 2.22. Here, $q_{area}(t)$ is the total charge per unit area. The boundary condition is $F(0, t) = 0$, which means there is no contact resistance at the injection contact at $x = 0$. As the applied voltage is constant, the integration of the right part of the sum in equation 2.21 is zero. The result is given in equation 2.23.

$$F(d, t) = \frac{q_{area}(t)}{\epsilon} \quad (2.22)$$

$$j(t) = \frac{\epsilon\mu}{2d} F^2(d, t) \text{ with } \int_0^d \frac{dF(x, t)}{dt} dx = \frac{dv(t)}{dt} = 0 \quad (2.23)$$

At $x = d$, only $j_{displ}(x, t)$ is relevant as long as the charge carriers did not reach the ejection contact, as no charge carriers are at this point. Thus, for $x = d$, equation 2.19 and 2.23 result in the differential equation 2.24. This equation is valid for $t < t_{trans}$. For $t \geq t_{trans}$, the assumption of no charge carriers at $x = d$ is not valid any more. The solution for the differential equation is given in equation 2.25, with $F(d, 0) = \frac{V_S}{d}$ as boundary condition (V_S is the applied voltage on the device).

$$\frac{dF(d, t)}{dt} = \frac{\mu}{2d} F^2(d, t) \quad (2.24)$$

$$F(d, t) = \frac{2V_S d}{2d^2 - \mu V_S t} \quad (2.25)$$

Considering the first injected charge carrier package, F at the charge carrier front is equal to $F(d, t)$ at the ejection contact. The integration of $v_{drift} = \mu \cdot F$ from $t = 0$ to t_{trans} with F from equation 2.25 leads to equation 2.26. The numerical solution for μ is given in equation 2.27 [22, 92, 95, 103]. This equation is used for the mobility calculation in the transient SCLC method.

$$d = \mu \int_0^{t_{trans}} F(d, t) dt = \frac{2}{\mu V_S} \cdot \ln \left(1 - t_{trans} \frac{\mu V_S}{2d^2} \right)^{-1} \quad (2.26)$$

$$\mu = 0.786 \cdot \frac{d^2}{V_S t_{trans}} \quad (2.27)$$

The determination of t_{trans} is shown here with a simulated example (Chap. 3) for the current over time in figure 2.5. The first pronounced current peak of each curve (vertical dashed lines) is at t_{trans} for different V_S . Additionally, a slight oscillation is visible afterwards, which is also described by Schilling and Schachter [137] and Szymanski et al. [153].

For calculating the relation between peak current and steady state current, the equations 2.19 and 2.25 are used at $x = d$ and $t = t_{trans}$ to result in equation 2.28. With equations 2.17 and 2.28, the ideal factor 1.21 as relation between peak current and steady state current can be calculated [92, 95]. This means, ideally, the peak current is by factor 1.21 higher compared to the steady state current.

$$j(t) = \frac{\epsilon \mu}{2d} \cdot \left(\frac{2dV}{2d^2 - \mu V t_{trans}} \right) \quad (2.28)$$

For a better understanding of the origin of the current peak, a phenomenally explanation is done in the following. At $t = 0$, the electric field is homogeneous and the first charge carriers are injected (Fig. 2.6). While these move through the semiconductor, successive charge carriers are injected (Fig. 2.6b). With the increasing charge within the semiconductor, the electric field is shielded in the area where the first charge carriers

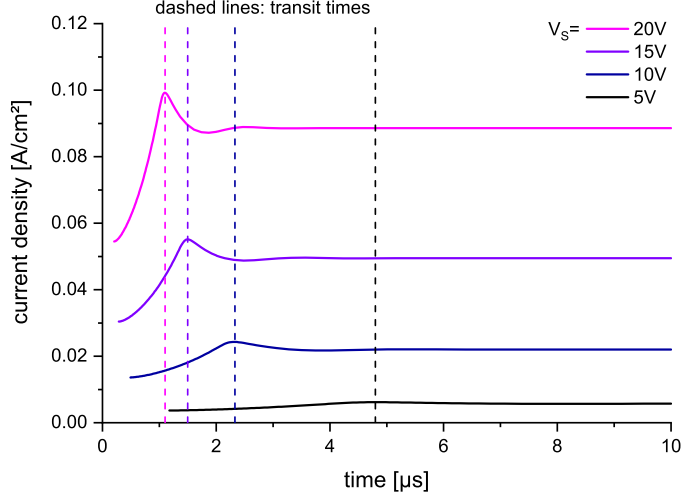


Figure 2.5: Ideal $J(t)$ curve of a transient SCLC signal. The data is simulated as described in chapter 3.2 for a 500 nm thick organic semiconductor with $f_{atj} = 1 \cdot 10^{12}$ Hz.

have passed through. As the over all voltage keeps constant, the electric field increases in the remaining space charge free region, which the charge carriers have not reached yet (Fig. 2.6a). This principle is valid until the first injected charge carriers reach the opposite electrode. Thus, these charge carriers are moved by a stronger average electric field than in the steady state at $t \rightarrow \infty$, causing the current peak at t_{trans} .

2.3.3 Qualitative discussion of non-ideal device parameters influencing the space charge limited current

There are many effects influencing both steady state and transient SCLC, which are correlated to non-ideal parameters. Generally, the influences of these parameters are stronger at thin layers [22, 31]. In this thesis, the measurement of thin organic polymers (< 300 nm) is necessary, as it is technologically difficult to produce thicker layers. Furthermore, thick layers are not needed in the application of organic semiconductor in devices. Consequently, the determined mobilities by both methods must be analyzed in respect to the following non-ideal parameters.

Starting with the steady state SCLC, the relation between current density and voltage is ideally $J \propto V^z$ with $z = 2$. For real devices, z is typically increased by the following aspects: the presence of an injection barrier and build-in field [4, 22], trap states [29, 120] and field dependence of the mobility [1, 4, 62, 119, 182]. A decrease of z can be caused by: diffusion [130], serial and shunt resistances [22], doping [12, 31] and space

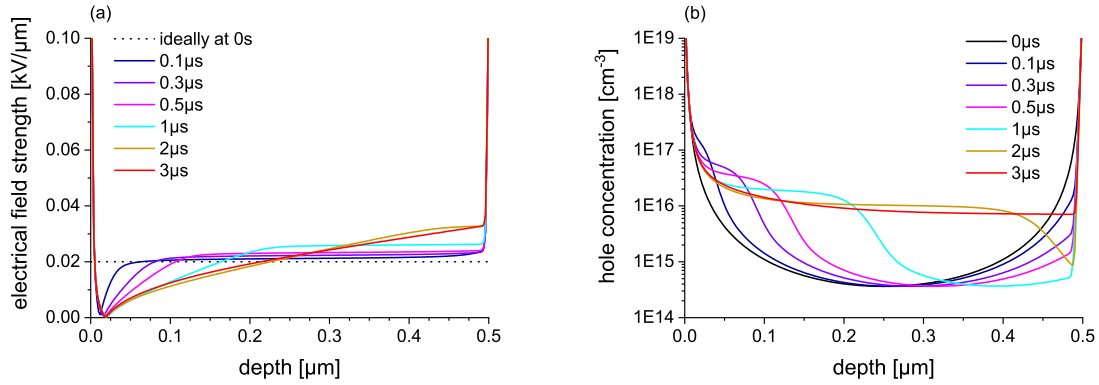


Figure 2.6: (a) Ideal electric field strength within the device and (b) distribution of charge carriers for subsequent time steps during a transient SCLC measurement. The data is simulated as described in chapter 3.2 for a 500 nm thick organic semiconductor with $f_{atj} = 1 \cdot 10^{12}$ Hz.

charge regions at the electrodes [130]. The effect of these non-ideal parameters varies in dependence of the semiconductor film thickness and increases mostly with thinner film thickness [22, 130, 182]. The discussed effects may cause a strong increase of z up to e.g. 6 and simultaneously limit the current, where a determination of the mobility with a quadratic fit by the Mott-Gurney law (Equ. 2.17) becomes invalid.

However, all discussed non-ideal parameters cause a decrease of the current in comparison to the ideal device. The only exception is a parallel current path with a low resistance, which is visible in the low voltage regime. Consequently, strong influences of a parallel current is visible in the JV curve. If $z > 2$, equation 2.17 can be used to determine a minimum μ for the mobility of the semiconductor bulk if fitted to a small voltage range.

A major difference between steady state and transient SCLC method is their dependency on the electric field strength. The mobility determined using the steady state measurement is a parameter independent of the electrical field strength, which is primarily useful for the material comparison of similar devices [22, 136]. In contrast, the mobility determined by the transient method is correlated to a certain average electrical field strength as a constant voltage is applied [153]. Thus, the field dependents of the mobility is directly visible with the transient method.

Considering the non-ideal parameters mentioned before for the steady state SCLC, there is always a decrease of the determined mobility by the transient method in comparison to the ideal device [62, 67]. However, the decrease is generally less pronounced for the transient method.

Special attention is needed for the influence of trap states on the transient signal. In case of shallow trap states, which are filled fast and cause a spreading of the first injected charge carrier package, slight shifts of the current peak to higher t_{trans} occur resulting in a lower determined mobility [103]. Typically, slowly filled deep trap states cause a slow attenuation of the current over much longer time scales than t_{trans} [95, 103, 120]. The reason is the slow reduction of the amount of free charge carriers contributing to the current. Consequently, there is little influence on the measured mobility.

A specific challenge for the transient SCLC method results from a high serial resistance and a consequently high RC time constant causing a wide charging current peak [62]. This peak may falsify the measurement by overlapping with the transient peak.

3 SCLC Simulation method

As the effects of non-ideal parameters on the SCLC increase with thinner semiconductor layers, a more precise analysis is necessary compared to the ideal theory discussed in chapter 2.3. For this purpose, the performed simulation investigates the influence of an injection barrier, external resistances, doping and built-in field on the SCLC in dependents of the semiconductor thickness. For the case of the time dependent transient SCLC, the influence of a parasitic capacitance and ramp time of a non-ideal voltage step is considered. The simulation, which is performed with the program Atlas (Silvaco, Inc.), uses the models described in the following. The complete code of the Atlas programming is given in the appendix (App. 8.3.1). As unipolar devices are considered, the simulation is performed only for holes. The results in case of electrons are equivalent. The corresponding equations for electrons are given in the appendix (App. 8.1).

3.1 models

For the stack structure of devices for SCLC measurements, a one dimensional simulation is sufficient. The following system of equations is solved for each point x in one dimension perpendicular to the layers. In the simulation, the Fermi level is replaced by the quasi Fermi level to account for the non-equilibrium caused by the applied voltage (Chap. 2.1.1).

The equations for Gaussian DOS, hopping mobility and Schottky contacts given in chapter 2.1 are used in the simulation. Additionally, the calculation is based on Gauss's law (Equ. 3.1), which gives the relation between the local electric field strength F and space charge density φ [152]. Here, $\epsilon = \epsilon_0\epsilon_r$ is the specific dielectric constant (ϵ_0 is the vacuum permittivity and ϵ_r the relative permittivity).

$$\operatorname{div}(F) = \frac{\varphi}{\epsilon} \tag{3.1}$$

The electrical field is defined by the gradient of the potential Ψ (Equ. 3.2) [152].

$$\vec{F} = -\nabla\Psi \quad (3.2)$$

These equations are complemented by the charge carrier continuity which describes, that the total number of charge carriers is only changed by generation, recombination or the change of current density [152]. Equation 3.3 shows the corresponding relation for holes. Here, p is the hole density and q the elementary charge, while J_p is the hole current density, $G_{gen,p}$ is the generation rate and $R_{rec,p}$ the recombination rate. As minority charge carriers are neglected in the simulation (unipolar device), only the equation of the majority charge carriers (holes in this case) is needed and $R_{rec,p}$ and $G_{gen,p}$ can be neglected, as all measurements are performed in darkness.

$$\frac{\delta p}{\delta t} = -\frac{1}{q} \cdot \text{div}\vec{J}_p + G_{gen,p} - R_{rec,p} = -\frac{1}{q} \cdot \underbrace{\text{div}\vec{J}_p}_{G_{gen,p}=R_{rec,p}=0} \quad (3.3)$$

Furthermore, the drift diffusion model is used with equation 3.4 (for holes and μ_p as hole mobility). The current is the sum of drift (left hand side of the sum) and diffusion current (right hand side of the sum).

$$\vec{J}_p = qp\mu_p\vec{F} + qD_p\nabla p \quad (3.4)$$

The diffusion coefficient D_p is given by the generalized Einstein equation (Equ. 3.5) at the temperature T with k_B as the Boltzmann constant [31]. This is the correlation between mobility and diffusion coefficient. The term $g_{3,p}$ (Equ. 3.6) describes the dependency of the diffusion coefficient on the charge carrier density and its change with the quasi Fermi level E_F and is valid in the specified limits for the charge carrier densities [131]. The parameters $c_{p,min}$ and $c_{p,max}$ are set to 0.5 for maximum and to 10^{-10} for minimum values and N_H is the total density of states for the HOMO. If either value c_i is out of any limit, it will be calculated at this limit which is a simplification of the calculation to reach convergence easier. Practically, there is neglectable change of D_p outside these limits [131] and the charge carrier density in the performed simulation does

not reach these limits.

$$D_p = k_B T \cdot g_{3,p} \cdot \frac{\mu_p}{q} \quad (3.5)$$

$$g_{3,p} = \frac{1}{k_B T} \cdot \frac{p}{\frac{dp}{E_F}} \quad \text{for} \quad (c_{p,min} N_H) < p < (c_{p,max} N_H) \quad (3.6)$$

To simulate the Gaussian DOS (for HOMO states) of an organic semiconductor, equation 3.7 is used by Atlas for holes (Chap. 2.1.1), where σ_H is the profile width and E_H the HOMO level.

$$g_H(E' - E_H) = \frac{N_H}{\sqrt{2\pi} \cdot \sigma_H} \cdot e^{-\frac{(E' - E_H)^2}{2\sigma_H^2}} \quad (3.7)$$

Because of convergence problems, the analytical approximation $p(E_{norm}) = N_H \cdot G_a(E_{norm}, s_{norm})$ is used for the calculation of the Gauss-Fermi integral (Equ. 3.8) as proposed by Paasch and Scheinert [118]. The normalized, thus dimensionless, values for the energy E_{norm} and for the width s_{norm} are given in equation 3.9.

$$p = \int_{-\infty}^{\infty} g_H(E' - E_H) f_{fd}(E_F - E') dE' \quad (3.8)$$

$$E_{norm} = \frac{E' - E_H}{k_B T} \quad \text{and} \quad s_{norm} = \frac{\sigma_H}{k_B T} \quad (3.9)$$

Two regions are defined for $G_a(E_{norm}, s_{norm})$ (equ. 3.10 and 3.11). Here, $E_{norm} \leq -s_{norm}^2$ corresponds to the nondegenerate limit of the semiconductor [152], where the Gaussian DOS decreases faster than the tail of the Fermi-Dirac distribution. Thus, the density of occupied states is defined by the DOS. For $E_{norm} \geq -s_{norm}^2$ in the degenerate limit, the full Fermi-Dirac distribution has to be considered [118].

$$G_a(E_{norm}, s_{norm}) = e^{\left(\frac{s_{norm}^2}{2} + E_{norm}\right)} \cdot \frac{1}{e^{(K_a(s_{norm}^2) \cdot (E_{norm} + s_{norm}^2))} + 1} \text{ for } E_{norm} \leq -s_{norm}^2 \quad (3.10)$$

$$G_a(E_{norm}, s_{norm}) = \frac{1}{2} \cdot \operatorname{erf}\left(-\frac{E_{norm}}{s_{norm}\sqrt{2}} H_a(s_{norm})\right) \text{ for } E_{norm} \geq -s_{norm}^2 \quad (3.11)$$

The factors $H_a(z)$ and $K_a(z)$ are given in equation 3.12, where $\operatorname{erf}(z)$ is the error function (Equ. 3.13).

$$H_a(z) = \frac{\sqrt{2}}{z} \operatorname{erf}^{-1}\left(e^{-\frac{z^2}{2}}\right) \quad \text{and} \quad K_a(z) = 2 - \frac{H_a(z)}{z} \cdot \sqrt{\frac{8}{\pi}} \cdot e^{\frac{z}{2} \cdot (1 - H_a^2(z))} \quad (3.12)$$

$$\operatorname{erf}(x) = \frac{1}{\sqrt{\pi}} \cdot \int_x^{-x} e^{-z^2} dz \quad (3.13)$$

In case of the time (t) dependent simulation for transient SCLC, all discussed equations are considered as time dependent. Additionally, the displacement current (\vec{J}_{dis}) equation is used [152] (Equ. 3.14).

$$\vec{j}_{dis} = \epsilon \cdot \frac{\delta \vec{F}}{\delta t} \quad (3.14)$$

3.2 Device parameters

Here, hole only devices with different thicknesses d are simulated. The energetic difference of the HOMO level to the vacuum level is irrelevant. The energetic distance to the LUMO level is set to a typical value of 2 eV, which defines the position of the Fermi level and therefore the intrinsic charge carrier density.

A basic device is defined, which considers as non-ideal parameters diffusion and the charge carrier density dependent mobility by using the hopping mobility described in chapter 2.1.2 as well as space charge regions at the contacts. In other aspects, the device

Table 3.1: Characteristic values of the simulated basic device.

parameter	value	comment and references
ϵ_r	3	as a typical value for organic semi-conductors [22, 29, 120, 153, 165, 180]
d	25 nm to 1 μm	with the values 50 nm, 100 nm, 300 nm and 500 nm in between
f_{atj}	10^{11} Hz to 10^{13} Hz	with the values $3 \cdot 10^{11}$ Hz, 10^{12} Hz and $3 \cdot 10^{12}$ Hz in between [7, 10, 19, 66, 148, 156]
total DOS	$10^{20} \frac{1}{\text{cm}^3}$ to $10^{21} \frac{1}{\text{cm}^3}$	with the value $5 \cdot 10^{20} \frac{1}{\text{cm}^3}$ in between [7, 8, 11, 131, 161, 165]
σ	0.1 eV	[11, 89, 102, 111, 112, 145, 153]
γ	10^{-7} cm^{-1}	[7, 8, 10, 156]
average F	$0.01 \frac{\text{kV}}{\mu\text{m}}$ to $0.05 \frac{\text{kV}}{\mu\text{m}}$	with $0.01 \frac{\text{kV}}{\mu\text{m}}$ steps in between
HOMO	5 eV	
LUMO	2 eV	

is considered to be ideal. The characteristic values for the basic device are given in table 3.1. The simulated device has an area of $10^4 \mu\text{m}^2$ and all parameters and results are normalized to this area, resulting in an area independent analyses. Examples for the simulated steady state and transient SCLC of the basic device are shown in figures 2.3 and 2.5.

Simulations with other non-ideal parameters are done only for the transient SCLC, as the steady state mobility is only used as a minimum reference value here. Figure 3.1 shows schematically the analyzed non-ideal parameters for the transient SCLC simulation, which are described in the following:

1. The influence of a non-ideal voltage step (V_S) is analyzed with the voltage ramp $v(t)(t) = a_{ramp} \cdot t$, where $a_{ramp} = V_S/t_{rise}$ is the slope of the ramp and t_{rise} the rise time.
2. The parallel resistance is simulated with a highly doped silicon parallel layer with ohmic behavior.
3. For doping, a typical charge carrier density, caused by doping, with the concentration

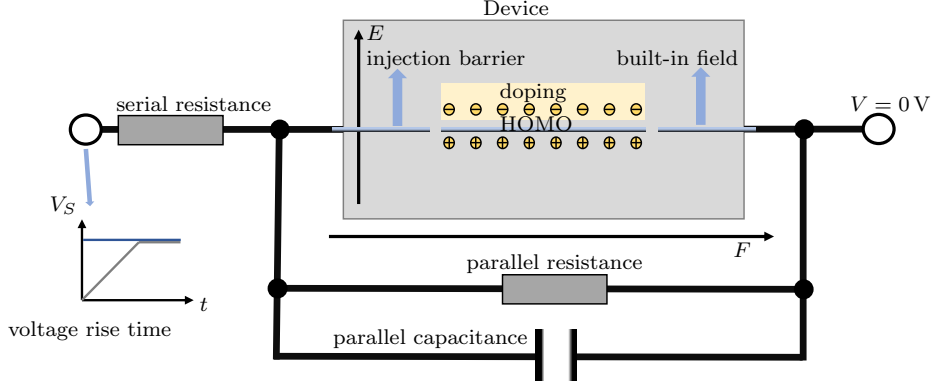


Figure 3.1: Schematic presentation of non-ideal parameters analyzed with the simulation.

of $10^{16} \frac{1}{\text{cm}^3}$ is simulated [29, 93, 120, 153]. This is simulated by adding a homogeneously distributed acceptor charge and an equal amount of free charge carriers. Generally, doping is only relevant, if the doping concentration is similar to the amount of injected charge carriers. Here, a doping concentration of $10^{15} \frac{1}{\text{cm}^3}$ has no influence as the amount of injected charge carriers is significantly higher. A doping concentration of $10^{17} \frac{1}{\text{cm}^3}$ already shows ohmic behaviour, as the charge carrier density of the material dominates compared to the injected amount.

4. The ejection electrode work function sets the built-in (energetic difference of the work functions) field to 0.2 V, 0.5 V or 1 V.
5. By choosing lower work functions of the injection electrode, injection barriers (energetic difference of work function and HOMO level) of 0.1 eV, 0.3 eV and 0.5 eV are considered.
6. For defining the serial resistance, it is multiplied with the device area. Using this concept, the RC time constant for device charging becomes independent on the device area. Here, the simulated values are: $7.5 \Omega \text{mm}^2$, $75 \Omega \text{mm}^2$, $1875 \Omega \text{mm}^2$ and $3750 \Omega \text{mm}^2$. At the same time, a parasitic capacitance normalized to the device area of $13.33 \frac{\text{pF}}{\text{mm}^2}$ is assumed. This correlates to the possible parasitic capacitance in the developed measurement circuit for transient SCLC.

From the simulated transient SCLC, the mobility μ is determined from the transient peak with equation 2.27. Here, only the mobility from $t_{trans} > 100 \text{ ns}$ is considered. Lower t_{trans} are not relevant in praxis, as they are not measurable considering the sample charging. For identical f_{atj} and F , μ is normalized to the value determined at $d = 1 \mu\text{m}$. A plot of this normalized $\mu(d)$ shows the influence of lower d on the determined mobility. This approach is only usable if the considered parameter does not influence the determined mobility at $1 \mu\text{m}$ thickness compared to the basic device.

For interpolation of the mobility data points depending on d (in μm), f_{atj} (in Hz) and average F (in $\frac{\text{kV}}{\mu\text{m}}$), the normalized mobility is fitted with equation 3.15 if possible. This fit is only usable in the case of a constant trend, which can either be increasing or decreasing for lower thicknesses. It is not appropriate for the case of e. g. a maximum mobility at a certain thickness. The variables A_{simu} , B_{simu} and C_{simu} are the fit parameters. In case of steady state SCLC (for the basic device), the term considering f_{atj} and F is not considered. In the appendix 8.3.3, the algorithm used for determining the fit parameters is described and the resulting parameters are given in table 8.8 (App. 8.3).

$$\mu_{norm} = 1 + A_{simu} \cdot \left(1 - \frac{d}{1 \mu\text{m}}\right)^{B_{simu}} \cdot \frac{\left(\frac{F}{1 \frac{\text{kV}}{\mu\text{m}}}\right)^{C_{simu}}}{\underbrace{\ln\left(\frac{f_{atj}}{1 \text{ Hz}}\right)}_{\text{only trans. SCLC}}} \quad (3.15)$$

4 Materials and sample layout

This chapter introduces the materials and samples used for evaluation of the proposed universal trap levels (Chap. 2.1.3). The measured materials are described in chapter 4.1. The device structures for the SCLC and TSC measurements are discussed afterwards in the chapters 4.2 and 4.3. In chapter 4.4, the production procedures for all samples are describes, as the processes are partly identical for SCLC and TSC samples.

4.1 Materials under examination

For the investigation of the proposed universal trap levels (Chap. 2.1.3), three different organic semiconducting polymers are analyzed in this thesis: *Poly(3-hexylthiophene-2,5-diyl)* (P3HT from Hübler Group, TU Chemnitz) [100, 109, 117, 121, 124, 128], *Poly[2,6-(4,4-bis-(2-ethylhexyl)-4H-cyclopenta[2,1-b;3,4-b']dithiophene)-alt-4,7(2,1,3-benzothiadiazole)]* (PCPDTBT from one Material) [70, 87, 100, 108, 109, 117, 176] and *Poly[2-methoxy-5-(3',7'-dimethyloctyloxy)-1,4-phenylenevinylene]* (MDMO-PPV from Sigma Aldrich) [6, 65, 72, 100, 117, 125, 128]. The molecular and structural formulas as well as HOMO and LUMO levels are given in table 8.2 in the appendix (App. 8.2). All these materials are typically used e. g. within active layers of LEDs and solar cells and therefore this is a good reference system.

Additionally, for validation purposes of the developed circuit for transient SCLC measurements, 4,4',4''-Tris[phenyl(m-tolyl)amino]triphenyl-amine (MTDATA from Sigma Aldrich) is investigated by the SCLC methods (Chap. 2.3). MTDATA is a small molecule that is well known from usage as hole injection or electron blocking layer [85, 91, 142, 145]. As the material is deposited by evaporation, a wide range of different layer thicknesses without changes in the microstructure is possible [27]. Consequently, MTDATA is an ideal choice for the investigation of thickness dependent effects on the SCLC signals.

All materials are kept in nitrogen atmosphere and under yellow light to exclude environmental influences on the materials.

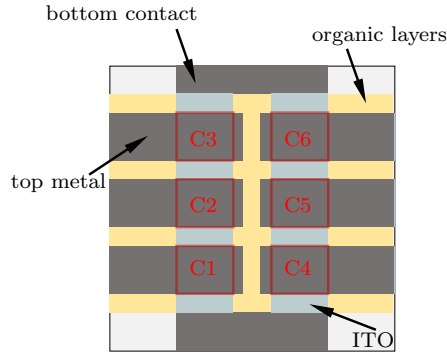


Figure 4.1: Sample layout for SCLC devices

4.2 Structure for SCLC samples

All SCLC devices are built on the same substrates, independent on the material. The used ITO substrates are glass plates with a pre-structured indium tin oxide (ITO) layer as shown in figure 8.1a in the appendix (App. 8.2) and are available from Naranjo BV. The ITO is 180 nm thick and has a sheet resistance of $15 \frac{\Omega}{\square}$. The active device area of 7.5 mm^2 is defined by the overlap of the ITO bottom and the metal top contact (Fig. 4.1). On one sample, six separate devices are realized named C1 to C6.

4.2.1 Hole only devices

Figure 4.2a shows the general device structure of the hole only SCLC devices in a cross cut view. For injecting holes, a Poly(3,4-ethylenedioxythiophene) polystyrene sulfonate (PEDOT:PSS, HIL-E100 from Haereus [40]) layer on top of ITO is used for all materials [77, 89, 165]. In case of the MTDATA hole only devices, an Aluminum (Al) top metallization is used. In this case, no additional electron blocking layer is necessary, as the resulting energy barrier for electrons is 2.15 eV (Fig. 4.2b). Generally, an energy barrier larger than 1 eV is considered as charge carrier blocking [145].

For the three polymers (P3HT, PCPDTBT, MDMO-PPV), this is not sufficient due to lower LUMO levels (Fig. 4.4). Therefore, a thin layer of 4,4'-Cyclohexylidenebis[N,N-bis(4-methylphenyl) benzenamine] (TAPC, Sigma Aldrich) is introduced on top of the polymers as electron blocking layer (Fig. 4.2a). The top electrode is Nickel (Ni, 50 nm), which results in an energy barrier of approximately 3 eV for electrons. The Ni layer is covered with a 300 nm Al layer to increase the conductivity of the metallization, as depositing thick Ni layers is challenging as discussed in chapter 4.4.

4.2.2 Electron only devices

Figure 4.3a shows the device structure of electron only devices. Compared to the hole only devices (Chap. 4.2.1), the top metallization is replaced by subsequent Calcium (Ca, 30 nm) and Al (300 nm) layers for electron injection (Fig. 4.4). In this case, Al protects the Ca from oxidation and provides an increased conductivity compared to only 30 nm Ca. The hole blocking layer is 30 nm 4,7-Diphenyl-1,10-phenanthroline (Bphen, Sigma Aldrich) on top of ITO creating an energy barrier of 1.7 eV [85, 97, 142]. As this layer would be damaged during the production process of the polymer layer (Chap. 4.4), a 5 nm thick layer of Aluminum-tris(8-hydroxyquinolin) (Alq3, Sigma Aldrich) is added, which protects the Bphen layer [3, 60, 142, 147, 169].

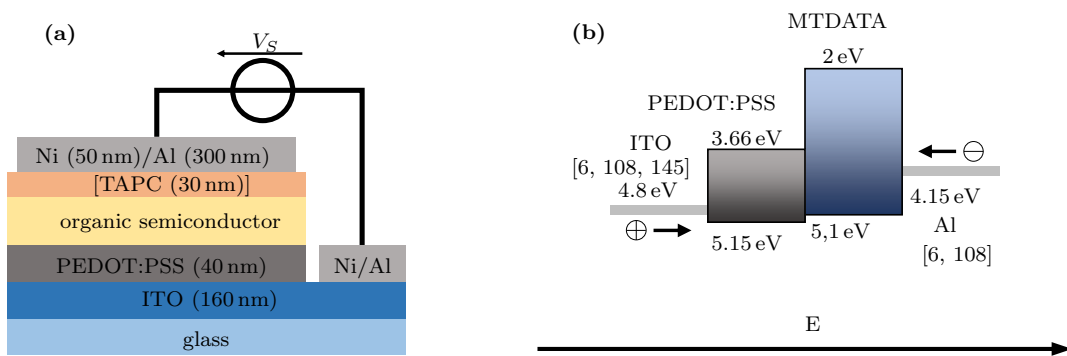


Figure 4.2: (a) Structure of SCLC hole only devices (the TAPC layer is not used for MTDATA diodes). The thickness of the organic semiconductor varies between 25 nm and 500 nm. (b) Energy alignment within the MTDATA hole only device. The literature references for HOMO/ LUMO levels are in tables 8.2 and 8.3 in the appendix 8.2.

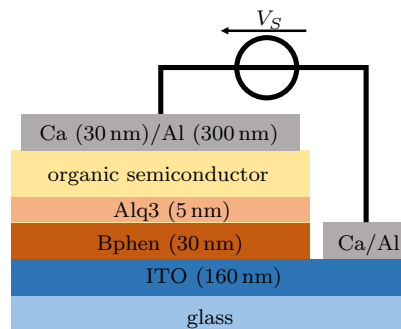


Figure 4.3: Side view of the electron only SCLC device structure. The thickness of the organic semiconductor varies between 25 nm and 500 nm.

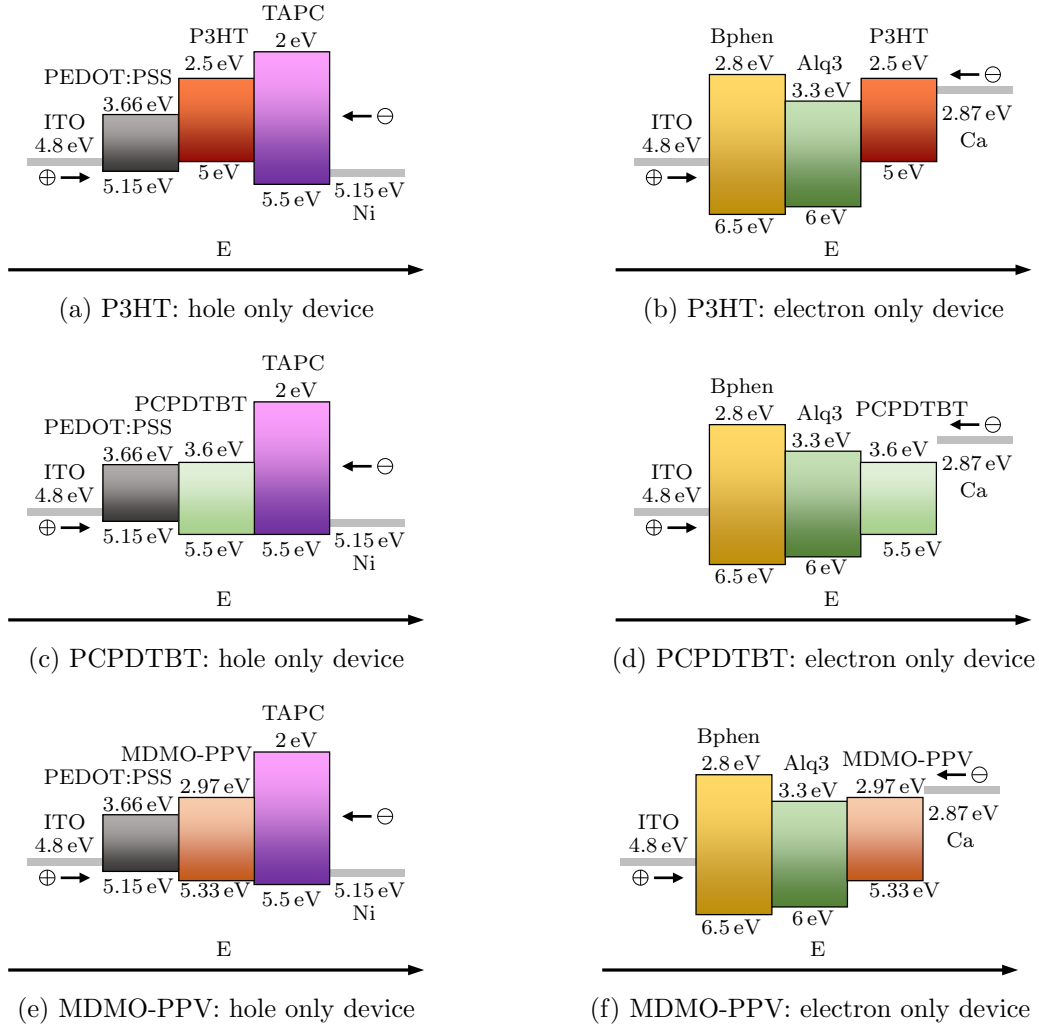


Figure 4.4: Produced SCLC samples for investigating the polymers: unipolar devices of P3HT, PCPDTBT and MDMO-PPV. The literature references for HOMO and LUMO levels are given in tables 8.2 and 8.3 in the appendix 8.2. The literature reference for the ITO work function is given in figure 4.2, for Nickel and Calcium it is [104, 152].

4.3 Structure of TSC samples

The classical TSC method (Chap. 2.2) is used in this thesis as a reference for the newly introduced MIS-TSC method (Chap. 6.1). The diode structure measured with the classical TSC method and the metal insulator semiconductor (MIS) structure measured with the MIS-TSC method are explained in the following.

4.3.1 Diode structure

The diode structure has the same layout as the devices for SCLC measurements (Chap. 4.2) with the difference that both contacts are injecting. The hole injecting contact is a PEDOT:PSS layer as described in chapter 4.2.1. The electron injecting contact is a Ca/Al top metallization, which is described in chapter 4.2.2. The organic semiconductor is a 80 nm thick layer of the organic semiconductor P3HT (Sepiolid P200, BASF). The total layer stack is from bottom to top: ITO/PEDOT:PSS/P3HT/Ca/Al.

4.3.2 Metal semiconductor insulator structure

In this chapter, the developed MIS structure for the MIS-TSC measurement is explained. For all MIS samples, the substrate is a $10^{15} \frac{1}{\text{cm}^3}$ n-doped silicon wafer with a 200 nm thick thermal oxide layer (SiO_2). The silicon is contacted with an Aluminum layer on the backside of the sample (Fig. 4.5a). On top of the SiO_2 , the organic semiconductor is located in three smaller areas as shown in figure 4.5b. These areas are completely covered by subsequent layers of silver (Ag, 100 nm) and Al (300 nm). Ag has a work function of 4.3 eV [61], which is in between the HOMO and LUMO levels of the polymers under investigation (Fig. 4.4), resulting in similar injection barriers (> 0.7 eV) for electrons and holes. The Al is necessary as a protection layer for the Ag as the used silver epoxy for contacting the devices, which is described in chapter 5.3, would dissolve the Ag layer.

For benchmarking the MIS-TSC, an additional layer of 0.5 nm Ca is introduced on top of the SiO_2 layer for passivation of surface trap states [20, 80, 155]. This increases the comparability of the MIS-TSC with the classical TSC results as well as with literature data as discussed in chapter 6.2. For the investigation of the oxygen and water traps (Chap. 2.1.3), the Ca layer is not used. As this analysis comparative between samples with the same interfaces, a passivation is not necessary in this case.

4.4 Production procedures for samples

Before deposition of any layer, all substrates are cleaned subsequently in an ultrasonic bath with acetone, soap (Mucasol, Sigma Aldrich), twice distilled water, mixture of isopropanol and acetone, ethanol and again twice distilled water. The detailed process is described in table 8.4 in the appendix 8.2.

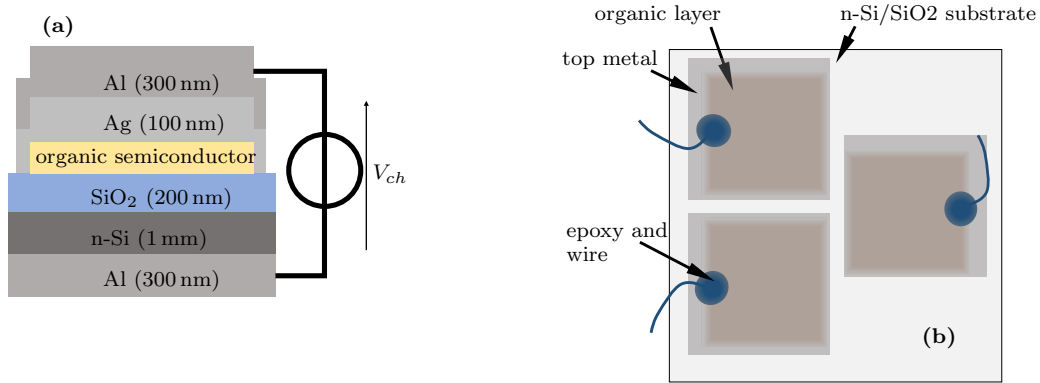


Figure 4.5: Sample layout for MIS-TSC measurements in (a) crosscut and (b) top view. The layout results in three separate measurable devices.

4.4.1 Spin coating processes

In this chapter, the spin coating processes for the three polymers (P3HT, PCPDTBT and MDMO-PPV) and for the contact material PEDOT:PSS is described. An overview for the deposition processes and parameters for the deposition of PEDOT:PSS and the polymers is given in the appendix 8.2 in tables 8.5, 8.6 and 8.7.

First, for PEDOT:PSS deposition, which is done in ambient atmosphere, the ITO substrate is UV light- and ozone-treated at 110 °C for 15 minutes prior to further processing [146]. The PEDOT:PSS solution HIL-E100 (Haereus) is diluted with twice distilled water in the ratio of 1:1. This results in a 40 nm thick layer on the substrate with the spin coating parameters 5 s (500 rpm) followed by 40 s (5000 rpm) at an acceleration of $5000 \frac{\text{rpm}}{\text{s}}$.

Second, for deposition of the polymers, each one is dissolved in chlorobenzene with the concentration $20 \frac{\text{mg}}{\text{ml}}$ for PCPDTBT and P3HT and $5 \frac{\text{mg}}{\text{ml}}$ for MDMO-PPV [108, 125, 135, 176]. For all materials, the solution was heated for 2 hours at 60 °C and then dissolved further using a Vortex Genie 2 for 3 days. For deposition, the solution was again heated to 60 °C. The following spin coating of the polymers was performed under nitrogen atmosphere with a maximum Oxygen concentration of 30 ppm and maximum water concentration of 5 ppm.

For the TSC samples, the spin coating was done with 50 μl solution and the parameters 40 s (1200 rpm) followed by 15 s (3000 rpm) at an acceleration of $120 \frac{\text{rpm}}{\text{s}}$. The solution dries at the low spin coating velocity and the faster velocity dries residual drops at the edges. The resulting layer thicknesses are below 100 nm. For the structure shown in figure 4.5b, material is wiped away with a cloth soaked with chlorobenzene.

Table 4.1: Spincoating parameters for thick layers of P3HT and PCPDTBT used for SCLC samples.

step	velocity	acceleration	time	explanation
1	200 rpm	$120 \frac{\text{rpm}}{\text{s}}$	10 s	homogeneous distribution of solution
2	75 rpm	$120 \frac{\text{rpm}}{\text{s}}$	60 s to 600 s	evaporation of solvent and consequently increase of concentration; longer times result in thicker layers
3	200 rpm	$120 \frac{\text{rpm}}{\text{s}}$	30 s	prohibits drying of solution at the edges
4	75 rpm	$120 \frac{\text{rpm}}{\text{s}}$	10 s	mixing solution flowing back from the sides with the middle to increase homogeneity
5	500 rpm	$120 \frac{\text{rpm}}{\text{s}}$	40 s	actual drying of the solution
6	3000 rpm	$1200 \frac{\text{rpm}}{\text{s}}$	20 s	drying of residual droplets of the solution

For SCLC samples, thicker films are required compared to TSC samples (Chap. 2.3). To achieve this, higher concentrations of the solutions are necessary [74]. Unfortunately, it is not possible to use solution with a higher concentration, as the viscosity gets too high and the solution dries too fast for spreading it homogeneously on the substrate. Therefore, a complex spin coating process is developed here, which increases the concentration due to evaporation of chlorobenzene during the spin coating process explained in the following. After spreading 50 μl of the solution over the sample, the spin coating is directly started. The individual steps of the spin coating and their explanations are given in table 4.1 for P3HT and PCPDTBT and table 4.2 for MDMO-PPV. The difference in the processes result from the higher viscosity of the MDMO-PPV solution compared to the P3HT and PCPDTBT solutions, which are similar to each other. With the variable time step 2 (for P3HT and PCPDTBT) and 1 (for MDMO-PPV), different film thicknesses can be achieved. Longer times and therefore higher concentrations result in thicker layers. The layer thicknesses of each produced sample is measured individually (Chap. 5.1). One exception from the described processes are MDMO-PPV layers which are thinner than 50 nm. For these samples, the same process as for the TSC samples was applied.

Table 4.2: Spincoating parameters for thick layers of MDMO-PPV used for SCLC samples.

step	velocity	acceleration	time	explanation
1	75 rpm	$120 \frac{\text{rpm}}{\text{s}}$	180 s to 480 s	evaporation of solvent and consequently increase of concentration; longer times result in thicker layers
2	200 rpm	$120 \frac{\text{rpm}}{\text{s}}$	20 s	intermediate step for slower increase of the rotation velocity for more homogeneity
3	600 rpm	$120 \frac{\text{rpm}}{\text{s}}$	40 s	actual drying of the solution
4	3000 rpm	$1200 \frac{\text{rpm}}{\text{s}}$	20 s	drying of residual droplets of the solution

Table 4.3: Evaporation parameters of metals and small molecules.

material	deposition rate	maximum pressure
Ca	0.3 to $1.3 \frac{\text{\AA}}{\text{s}}$	$6 \cdot 10^{-6}$ mbar
Ca (passivation)	below $0.1 \frac{\text{\AA}}{\text{s}}$	$4 \cdot 10^{-6}$ mbar
Al (first 30 nm)	0.5 to $2 \frac{\text{\AA}}{\text{s}}$	$6 \cdot 10^{-6}$ mbar
Al (remaining thickness)	up to $50 \frac{\text{\AA}}{\text{s}}$	$2 \cdot 10^{-5}$ mbar
Ag	0.5 to $2 \frac{\text{\AA}}{\text{s}}$	$6 \cdot 10^{-6}$ mbar
Ni	0.2 to $1 \frac{\text{\AA}}{\text{s}}$	$1 \cdot 10^{-5}$ mbar
MTDATA	0.2 to $1.3 \frac{\text{\AA}}{\text{s}}$	$2 \cdot 10^{-6}$ mbar
TAPC, Bphen, Alq3	0.2 to $0.8 \frac{\text{\AA}}{\text{s}}$	$2 \cdot 10^{-6}$ mbar

4.4.2 Evaporation processes

For evaporation of any layer, the samples were moved from nitrogen atmosphere with both water and oxygen below 1 ppm into the evaporation chamber. Small molecules and metals were evaporated with the parameters shown in table 4.3. The film thicknesses are measured in-situ with an oscillating crystal. The base pressure when starting the evaporation process was in all cases $2 \cdot 10^{-6}$ mbar or below.

In case of aluminum layers, it is crucial that the layer is closed for the protection of the underlying layer as discussed in chapters 4.2 and 4.3. For this purpose, the first 30 nm of the Al layer were evaporated slowly. Further thickness was achieved by much higher

evaporation rates. The Ca passivation for benchmark MIS-TSC samples (Chap. 4.3.2) was evaporated much slower than other Ca layers because of the low thickness of 0.5 nm. For all metals evaporated here, Ni is the most difficult as it has the highest boiling point which results in a low deposition rate.

The small molecules TAPC, Bphen and Alq3 for blocking layers are evaporated all with the same parameters. In contrast, MTDATA was evaporated faster to deposit thicker layers up to nearly 1 μm within reasonable time scales.

4.4.3 Aging of semiconductors

For the investigation of the universal trap states, additional oxygen and water trap states (Chap. 2.1.3) are introduced into the polymers (P3HT, PCPDTBT and MDMO-PPV). For this purpose, different aging processes are done by exposing the samples to oxygen, moist nitrogen and UV light as listed in table 4.4. This exposure was done after the spin-coating of a polymer and before deposition of any subsequent layer.

The aging was done within an airtight chamber, which was loaded within nitrogen atmosphere. Afterwards, the gases for aging are led into the box. For the UV light, the LEDs 260018 from Optosource [58] are used in a distance of 0.5 cm above the treated sample with a driving voltage of 3.5 A and current of 17 mA. After the aging process, the samples are moved back into nitrogen atmosphere.

The gas exposure time of 2 hours is sufficient for saturation of the oxygen or water concentration in the organic semiconductor [110, 143]. It is known that oxygen and water diffuses out of the semiconductor in inert atmosphere and hence the caused degradation is reversible [110, 114, 140, 178]. Thus, the samples are exposed to UV light (370 nm) during the last 5 minutes of gas exposure [143]. This leads to photo oxidation and creation of oxygen dependent functional groups [68, 101, 140, 161]. As a reference, samples with only UV light treatment without oxygen or water exposure are produced.

Table 4.4: Aging processes for the polymers (P3HT, PCPDTBT, MDMO-PPV).

process	description
UV light treatment	600 s UV light exposure
oxygen treatment	2 hours exposure to technical air (20.5 % oxygen and 79.5 % nitrogen) and subsequent 600 s UV light exposure
water treatment	2 hours exposure to moist nitrogen (moisture > 90 %) and subsequent 600 s UV light exposure

5 Measurement setups and procedures

For the evaluation of the polymers, the steady state and transient SCLC as well as TSC signals were measured in this thesis. Because of the need for low RC time constant, a circuit is developed, which is discussed in chapter 6.3. The standard measurement setups are described in the following.

5.1 Thickness measurement

The profilometer Ambios XP-100 is used for measuring surface profiles. For the thickness measurement of deposited organic layers, scratches are made into the layers. These scratches are located in between the metal top contacts. The profiles are measured at 12 points for determination of the depth of these scratches. As the thicknesses of PEDOT:PSS, TAPC, Bphen and Alq₃ are known from the evaporation (Chap. 4.4.2), the corresponding values are subtracted from the measured thickness.

5.2 Current- and capacitance-voltage measurements

The SCLC in the steady state is measured with a parameter analyzer 4200-SCS from Keithley. The samples are contacted with spring contacts inside a nitrogen filled chamber. Current-voltage (IV) curves were measured for each sample beginning at 0 V with a sweeping mode and a total measurement time of at least 60 s. This relatively slow measurement for IV curves is necessary, as the current through organic semiconductors reaches the steady state slowly [22]. The maximum voltage differs for each sample, as the maximum tolerable voltage without breaking the sample depends on the film thickness.

Using the same parameter analyzer, capacitance-voltage (CV) curves are measured for evaluation of the Calcium passivation used in the MIS-TSC device structure (Chap. 4.3.2). For this purpose, a 50 kHz and 50 mV excitation is applied in the bias voltage range -30 V to 30 V. The CV signals were independent on the used frequency in the range 10 kHz to 100 kHz. Thus, only the results from applying 50 kHz are used here.

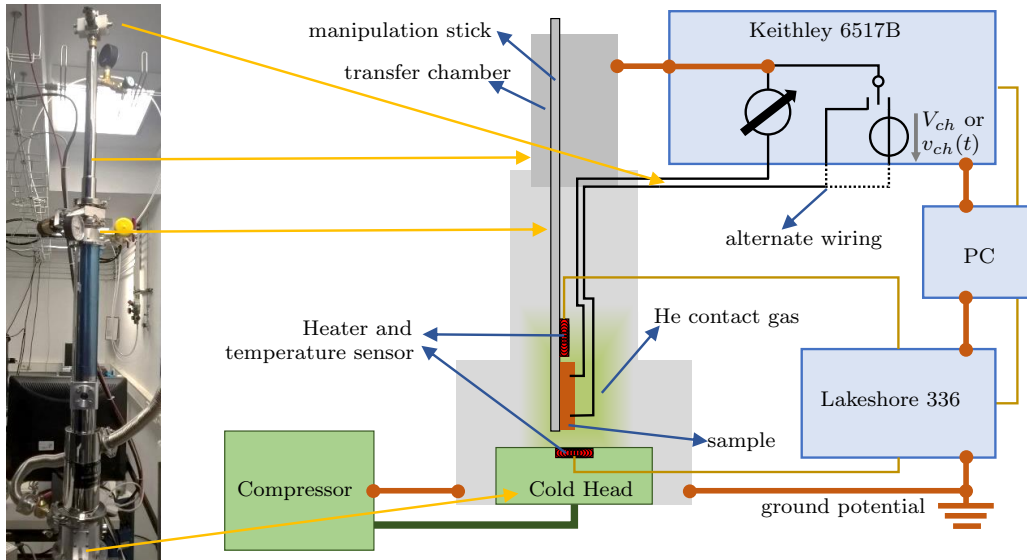


Figure 5.1: Setup for the TSC measurements.

5.3 TSC setup

The setup (Fig. 5.1) for the TSC measurements consists of a contact gas (Helium, He) cryostat (model CCS-500/204N, Janis Research), a temperature controller (Lakeshore model 336) and an electrometer (Keithley model 6517B).

The sample under test is transferred without air exposure into the cryostat with a transfer chamber which is loaded within nitrogen atmosphere. For the electrical contact, wires are glued on top of the contacts with the silver epoxy EPO-TEK H21D (Epoxy Technology) [41]. The samples are heated for 720s at 130 °C for hardening the epoxy.

In the cryostat, the temperature is set by two heaters, while the cold head (CH-204SFF-N, Sumitomo) provides constant cooling. One sensor near the sample and another one within the cold head measure the temperature. The temperature of the cold head is always set 2K below the temperature of the other sensor. This sensor is in metallic contact to the device under test, which provides low thermal resistance. Thus, the temperature measured by this sensor is used for the interpretation of the data.

For the TSC measurement procedure as described in chapter 2.2, the device under test is charged by the voltage source of the electrometer. During the measurement, this source is externally, by changing wires, and internally disconnected from the measurement circuit. This reduces the noise level of the TSC signal. For further reduction of the noise level, the outer conductor of the coaxial wires, common potential of the measurement loop and all enclosures are connected to the same mass potential.

The parameters for the enveloping and fractional TSC measurements, as described in chapter 2.2, are given in table 5.1. For the fractional measurement, the effective temperature step width is 20 K. The heating rates and the cool down processes are identical for enveloping and fractional measurements.

Table 5.1: Parameters for TSC measurements as they are described in chapter 2.2.

parameter	value
Δt_1	600 s
Δt_1	600 s
V_{ch}	-3 V
time for extracting excess charge	1800 s
β (cool down)	$0.05 \frac{\text{K}}{\text{s}}$
β (heating)	$0.02 \frac{\text{K}}{\text{s}}$
Δt_{f1}	300 s
Δt_{f2}	600 s
Δt_{f3}	900 s (for benchmarking) and 2800 s (for universal trap analysis)
T_2	$T_1 + 50 \text{ K}$
T_2	$T_3 + 20 \text{ K}$

6 Results

In this thesis, the recently discussed universal trap states in organic semiconductors are investigated [111, 183] (Chap. 2.1.3). For this purpose, the trap distribution and charge carrier mobility is determined for three different polymers (Chap. 4.1) in dependence on controlled aging (Chap. 4.4.3). The trap distribution of the materials is analyzed with TSC measurements (Chap. 2.2) and the mobility is measured with the steady state and transient SCLC method (Chap. 2.3).

6.1 Thermally stimulated current method for unipolar measurements

The classical TSC method as described in chapter 2.2 has the advantage of a direct access to the activation energy E_a of trapped charge carriers, which is assigned to the energetic trap depth. However, the measurement of a bipolar diode is a significant disadvantage, as the separate determination of electron and hole trap states is not possible [63]. Furthermore, classical TSC approaches are utilizing the device built-in field for charge extraction, which leads to special requirements for the contact materials. Additionally, recombination of complementary charge carriers is possible, which falsifies the trap depth and distribution information [14, 17].

Consequently, for the determination of the unipolar trap distribution required in this thesis, the classical TSC method is not suitable due to the bipolar nature of the results. This challenge is solved by a modification the classical method, as described in the next chapter (Chap. 6.1.1).

6.1.1 MIS-TSC method

The modification of the classical TSC method for unipolar measurement is introduced in this chapter. Here, the diode used for the classical TSC method as described in chapter 2.2 is replaced by a metal-insulator-semiconductor (MIS) structure [132]. This

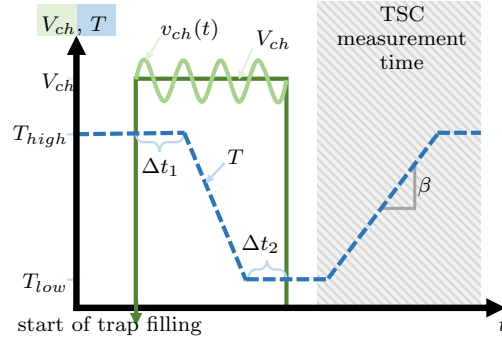


Figure 6.1: Schematic timing diagram of the MIS-TSC measurement: The difference to the classical TSC (Fig. 2.1) is the use of the oscillating $v_{ch}(t)$.

modification allows for unipolar trap occupation by choosing the polarity of the electric field during the electrical charging process. Consequently, this modification avoids recombination and bipolar contributions. Instead of being dependent on the built-in field for the charge extraction, the charge extraction is driven by the electric field introduced into the device by the trapped charges.

The sequence of the enveloping measurement is shown in figure 6.1. Principally, the enveloping and fractional measurement procedure for the MIS-TSC method is identical to the case of classical TSC (Chap. 2.2). Here, the charging voltage $V_{ch} < 0$ charges the semiconductor with holes and $V_{ch} > 0$ with electrons. Additionally to the constant V_{ch} , an oscillating charging voltage $v_{ch}(t)$ (Equ. 6.1) is tested in this thesis. With $v_{ch}(t)$, the trap occupation probability can be increased as discussed later in chapter 6.2.5. Here, A_{amp} is the amplitude of the oscillation and ω the angular frequency.

$$v_{ch}(t) = \pm V_{ch} + A_{amp} \cdot \sin(\omega t) \quad (6.1)$$

The charging mechanism and the extraction of trapped charge carriers are described in the following in chapters 6.1.2 and 6.1.3, respectively.

6.1.2 How trap states are filled during charging

The measurable TSC is strongly dependent on the effectiveness of the charging procedure, as it is the case for the classical TSC (Chap. 2.2.2). In contrast to a diode, there is no constant current through a MIS device by applying V_{ch} because of the insulating layer. For the case of maximum charge accumulation in this capacitor structure, the

introduced charge will accumulate at the semiconductor/ insulator interface. Consequently, the maximum charge $Q_{max,MIS}$ is defined by the insulator capacitance. The maximum charge per area (Equ. 6.2) is defined by the break down voltage of the insulator, the thickness d and the specific permittivity ϵ_r of the insulator.

$$Q_{max,MIS} = \frac{\epsilon_0 \epsilon_r}{d} \cdot V_{ch} \quad (6.2)$$

The occupation of trap states is dependent on the equilibrium between free and trapped charge carriers as discussed for the diode in chapter 2.2.2. By charging with a constant V_{ch} , the inhomogeneous charge distribution due to accumulation at the insulator interface may result in inhomogeneous trap occupation with lower occupation density in the bulk, which may falsify the trap distribution information. To increase the occupation of bulk trap states, the oscillating voltage $v_{ch}(t)$ can be applied (Chap. 6.1.1). A permanent charging and discharging current through the bulk is generated, which has a similar effect as the current through the diode structure for classical TSC. However, due to higher charge carrier density in the MIS structure compared to the diode, which is caused by higher V_{ch} , a higher trap filling probability for the MIS device is possible.

6.1.3 Heating procedure and measuring the TSC

The heating procedure is identical with the classical TSC method and the thermally excited charge carriers result in the TSC. Consequently, the same analysis with equation 2.7 is possible for the MIS structure as described in chapter 2.2.3.

As for the diode, the device under test is in a short circuit during the heating procedure, but the charge carrier extraction mechanism is different for the MIS-TSC. An electric field is introduced into the MIS devices by the trapped and free excess charge which causes the discharging. This discharging depends on the temperature dependent ejection RC time constant τ_e , which is primarily defined by the insulator capacitance and the semiconductor conductivity. As the mobility increases with the temperature (Chap. 2.1.2), the conductivity increases with the temperature, too.

The injection of complementary charge carriers and consequently unintentional recombination needs consideration. This can be avoided by a charge carrier injection time constant $\tau_i \gg \tau_e$. Also, τ_i has to be large in comparison to the total measurement duration. This can be achieved with an adequate contact metal with a work function in the middle of HOMO and LUMO resulting in a large injection but no ejection barrier.

6.1.4 Measurement procedure for determining trap distributions

As mentioned in chapter 6.1.1, the general measurement procedure for the MIS-TSC method is identical to the classical method described in chapter 5.3. The process parameters for the MIS-TSC measurement are generally the same as for the classical method given in table 5.1. The change of some parameters for different experiments done in this thesis are described in the following.

First, for benchmarking the MIS-TSC method, a constant charging voltage of $V_{ch} = 50 \text{ V}$ for electrons and $V_{ch} = -50 \text{ V}$ for holes is applied. Other parameters as they are described in chapter 5.3 are the same as for the classical method, apart from the heating rate $\beta = 0.015 \frac{\text{K}}{\text{s}}$. This lower β is possible due to the low noise level (Chap. 6.2.1) of the MIS-TSC method and increases the resolution of eventual overlapping TSC peaks.

Second, the effectiveness of different charging procedures is investigated in this thesis. For this purpose, the same procedure as described above is used, but with different $|V_{ch}|$ (20 V, 35 V, 50 V). Additionally, the use of an oscillating voltage with a constant bias is investigated with $v_{ch}(t) = \pm 40 \text{ V}$, $A_{amp} = 10 \text{ V}$ and $\omega = 0.005 \text{ Hz} \cdot 2\pi$. In this case, the fastest possible cooling with $0.07 \frac{\text{K}}{\text{s}}$, $\Delta t_1 = 1200 \text{ s}$ and $\Delta t_2 = 2000 \text{ s}$ is used.

Third, for the investigation of the oxygen and water traps, the charging process using $v_{ch}(t)$ is applied and a heating rate of $0.03 \frac{\text{K}}{\text{s}}$ as well as $\Delta t_{f2} = 2800 \text{ s}$.

The energetic trap depth distribution is determined with the fractional method (Chap. 2.2.4). Generally, for all fractional measurements, the same charging procedures and β are used as for the corresponding enveloping measurements.

6.2 Verification of the MIS TSC principle

As the MIS-TSC method is a newly developed technique, the proof of principle for this method is shown in the following. For this purpose, influences resulting from the sample structure have to be analyzed. These can be charge carrier trapping within the substrate (within the n-Si or its interfaces), causing additional TSC signals or thermally stimulated depolarization current (TSDC) [162] caused by polarization of the isolating SiO_2 .

6.2.1 Analyzing substrate influences

For the purpose of analyzing substrate influences, a reference sample was built using a Si/SiO₂ substrate and the described contact metallization only (Chap. 4.3.2). Figure 6.2 shows the TSC signal of this sample with and without charging. Both signals are iden-

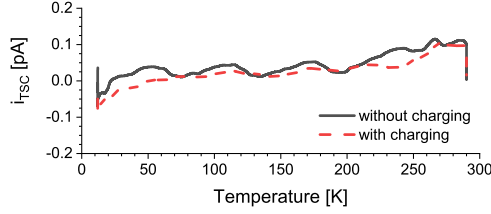


Figure 6.2: MIS-TSC measurement of a Al/n-Si/SiO₂/Ag device with $A = 16.25 \text{ mm}^2$.

tical in the 0.2 pA range which is within the noise level. In comparison to TSC signals of about 1 pA, there is a neglectable influence of charge trapping in the substrate and its interfaces. Furthermore, no TSDC contribution is visible.

The signals in figure 6.2 proof low leakage currents due to the high serial resistance of the MIS substrate. For the classical TSC method, the leakage current through the diode is in the range of several pA. Generally, leakage currents are caused by the burden voltage of the used electrometer (up to 100 μV), which also influences the TSC [84, 113, 167]. Therefore, precise measurements in the sub pA-range are possible with the MIS-TSC method.

6.2.2 Benchmarking the MIS-TSC method in comparison to the classical TSC method

In this chapter, the MIS-TSC method is compared to the classical TSC method. The measurement procedures are explained in chapters 5.3 for classical TSC and in chapter 6.1.4 for the MIS-TSC. As a benchmark, a classical TSC measurement of a P3HT diode (Chap. 4.3.1) is shown in figure 6.3a and discussed in the following. The current without sample charging $I_{TSC,without}$ (red dash/dotted line) is the consequence of the burden voltage of the electrometer and the temperature dependent low serial resistance of the device, thus changing with T [138]. The current with charging $I_{TSC,with}$ (dark gray dotted line) is the superposition of $I_{TSC,without}$ and the actual TSC signal I_{TSC} , which can be determined by equation 6.3 (solid blue line). For the comparison to the MIS-TSC measurement, the TSC signals are normalized to the active volume of the samples to account for different electrode areas and film thicknesses.

$$I_{TSC} = I_{TSC,with} - I_{TSC,without} \quad (6.3)$$

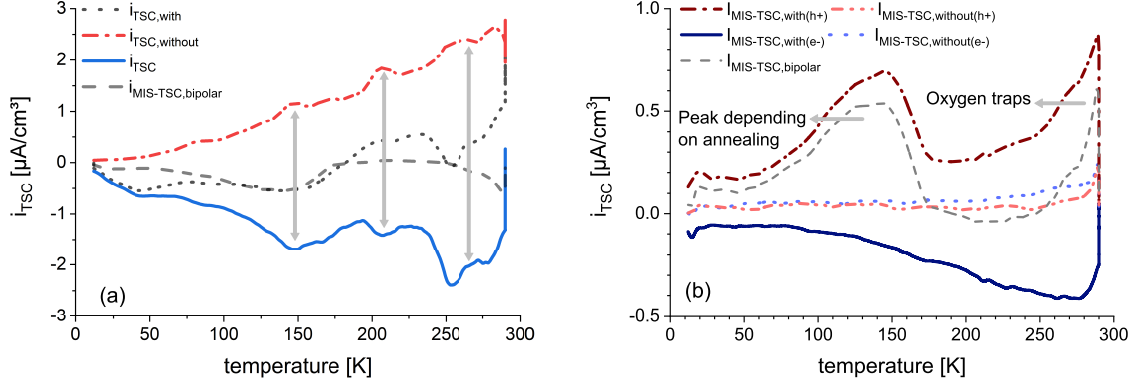


Figure 6.3: (a) Classical TSC measurement and (b) MIS-TSC measurement of P3HT.

Because of this correction, the measurement artifacts of $I_{TSC,without}$ cause false peaks in the determined I_{TSC} , as indicated by the gray arrows in figure 6.3a. However, the peaks of I_{TSC} at 150 K and 260 K are well in line with literature data. Yu et al. also found peaks at 170 K and 300 K, which they related to hole trap states [178]. In agreement, Souza et al. found a TSC peak between 170K and 220K, depending on a heating treatment of P3HT [149]. The lower peak positions in this thesis are caused by a lower heating rate. Yu et al. showed a peak at 220 K for PEDOT:PSS, which falsifies the TSC signal of P3HT in the range between 150 K and 260 K. Again, the peak position at a higher temperature is caused by a higher heating rate. Both contributions used a heating rate of $\beta = 0.1 \frac{\text{K}}{\text{s}}$ compared to $\beta = 0.015 \frac{\text{K}}{\text{s}}$ in this thesis.

Figure 6.3b illustrates the result of the MIS-TSC measurement of a P3HT MIS sample as it is described in chapter 4.3.2, which is comparable to the classical TSC measurement discussed before. Here, separate electron ($I_{MIS-TSC,with(e-)}$) and hole ($I_{MIS-TSC,with(h+)}$) signal are shown, in both cases without and with charging. The measurements without charging ($I_{MIS-TSC,without(e-)}$ and $I_{MIS-TSC,without(h+)}$) show the leakage currents, caused by the burden voltage. Compared to the signals with charging, $I_{MIS-TSC,with(h+)}$ and $I_{MIS-TSC,with(e-)}$, the leakage currents are neglectable proving the low noise level discussed in chapter 6.2.1. Thus, a correction as discussed for the classical TSC measurement is not required. Consequently, $I_{MIS-TSC,with(h+)}$ and $I_{MIS-TSC,with(e-)}$ originate from trap states within the P3HT, either from bulk or interface states. As the results for the hole and electron measurements are completely different, a polarization of P3HT is not present. This is confirmed by Yu et al., as they showed that polarization effects for P3HT are only relevant at temperatures far above 300 K [178].

The pronounced peaks originating from hole trap states ($I_{MIS-TSC,with(h+)}$, dark-red dash/dotted line) at 140 K and 300 K are in line with the peaks of I_{TSC} in figure 6.3a

and confirms the interpretation of Yu et al. as hole related trap states [178]. The electron only TSC ($I_{MIS-TSC,with(e-)}$, dark-blue solid line) demonstrates a wide peak at 270 K. Here, a possible explanation for this peak are interface states such as hydroxyl groups [30]. For a better comparability of the classical TSC and MIS-TSC signals, the bipolar MIS-TSC signal ($I_{MIS-TSC,bipolar}$, gray dashed line in both figures 6.3a and b) is calculated by assuming a recombination probability of 1 (Equ. 6.4). This means, simultaneously excited holes and electrons recombine before they are extracted from the device.

$$I_{MIS-TSC,bipolar} = I_{MIS-TSC,with(e-)} + I_{MIS-TSC,with(h+)} \quad (6.4)$$

Considering figure 6.3a, a good match of peak positions of $I_{MIS-TSC,bipolar}$ and I_{TSC} is evident. The slight difference in peak positions can be explained by the higher β chosen for the classical TSC. The lower $I_{MIS-TSC,bipolar}$ compared to I_{TSC} is a result of the burden voltage. An applied voltage on a diode during the classical TSC measurement results in a higher conductivity, originating from a higher charge carrier concentration and possibly a higher charge carrier mobility [17, 138, 177]. Thus, the TSC signal is increased. The absence of the elevated current level between 170 K and 270 K in $I_{MIS-TSC,bipolar}$ is expected, as no PEDOT:PSS was used in the MIS device [178].

The comparison between classical TSC and MIS-TSC showed, that in both cases similar TSC peaks are measurable. In comparison, the MIS-TSC signal shows much less unwanted contributions like leakage current or measurement artifacts. Furthermore, trap states can be measured unipolar with the MIS-TSC method, which is crucial for analyzing the oxygen and water dependent trap states in this thesis. For determining a trap level distribution, which is essential in case of several occurring trap levels, the fractional TSC method is applied as described in the next chapter.

6.2.3 Calcium passivation of SiO₂

In case of MIS-TSC measurements, it is unclear whether trap states are located at the semiconductor/ dielectric interface or in the semiconductor bulk. To reduce known interface trap states, such as hydroxyl groups, thus increasing the comparability to literature data, a calcium passivation is used for the benchmark measurements. The effect of this passivation is investigated with a capacitance-voltage (CV) measurement shown in figure 6.4 with the measurement procedure described in chapter 5.2.

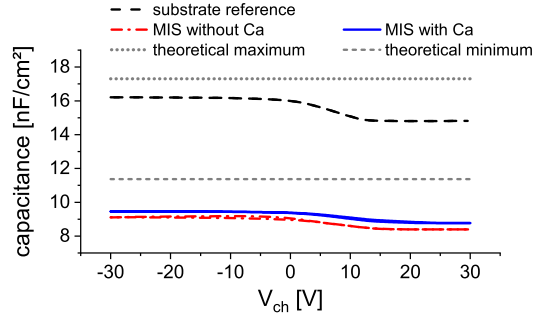


Figure 6.4: Voltage dependent capacitance measurement of a MIS device with and without Ca surface passivation as well as of the reference device without semiconductor as used in chapter 6.2.1.

The substrate reference is a CV measurement of only the substrate without a semiconductor as used for the substrate analysis in chapter 6.2.1. The theoretical maximum is the calculated capacitance of the SiO_2 and the theoretical minimum capacitance, assumes the organic semiconductor to be an insulator. Furthermore, CV measurements of P3HT MIS samples with and without Ca passivation of the SiO_2 are shown. For these curves, the capacitance contribution of metal contacts directly in contact with SiO_2 is subtracted from the measurements, using the substrate reference measurement.

The capacitance decrease for $V_{ch} > 0$ (electron accumulation) of 10% is the same for all three samples. This is caused by a space charge region in the n-Si substrate, increasing the thickness of the capacitance. The measured capacitance of both MIS devices is significantly lower than the substrate reference and the theoretical minimum. This can only be explained by trapped charge carriers within the P3HT. The extraction of this charge is not fast enough to follow the applied frequency.

There is a slight increase of the capacitance due to the passivation indicating successful passivation of hydroxyl groups [5, 20]. However, other defect states can be introduced by the calcium as discussed by Zhu et al. [181]. The large difference to the substrate reference can also be caused by bulk defect states, which are not influenced by interface passivation. In this case, interface trap states would be not relevant for the MIS-TSC analysis.

6.2.4 Fractional MIS-TSC

For the investigation of the energetic electron and hole trap level distribution, the fractional MIS-TSC method is used with the measurement procedure described in chapter 6.1.4. Figure 6.5 shows the fractional signals for electron and hole measurements as

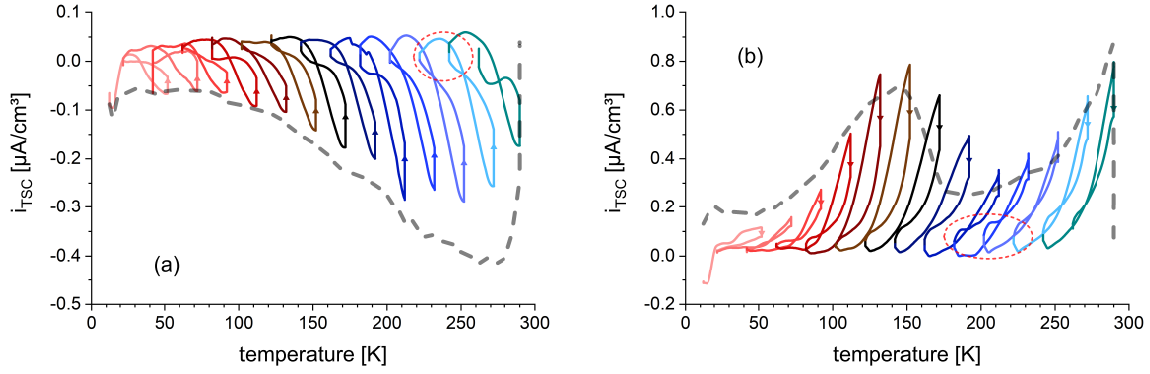


Figure 6.5: Fractional MIS-TSC measurements for (a) electrons and (b) holes are shown. The dashed lines are the corresponding enveloping measurements. The red dashed circles mark example ranges, where the signal during the cool down is larger than during the heating sequence.

well as the enveloping signals from figure 6.3 (dashed gray lines) for comparison.

Normally, the current maximum of fractional signals should be lower than the enveloping curve. This is caused by the waiting time Δt_{f2} at the maximum temperature of each temperature sequence (Chap. 2.2.4). During Δt_{f2} , additional charge carriers are extracted compared to the enveloping measurement causing the lower peak current. Here, this relation is true for electrons, but not for holes. The reason for this is the higher β for the fractional measurement (Chap. 6.1.4), which is applied to get a better signal to noise ratio. In case of electrons, the lower mobility compared to holes causes slow charge extraction and thus a low current peak. In contrast, the faster hole extraction causes the increased current peaks.

Occasionally, for a single temperature step, the current signal during cool down is larger than compared to the heating sequence, marked by the red dashed circle lines. This effect is caused by too slow charge extraction due to a low mobility or retrapping. This means, the waiting time Δt_{f2} is too short for complete charge extraction at the maximum temperature of each fractional step. However, as the current returns to zero at the beginning of each step, full charge extraction for the previous E_a level is achieved and therefore, there is no negative impact on the measurement.

For the trap level distribution, the energetic trap depth and the amount of trap states has to be calculated for every temperature step. The activation energy E_a , which is assumed to be the energetic trap depth (Chap. 2.1.3), is determined with a linear regression at the plot of $\ln(I_{TSC})$ over $1/T$ (Chap. 2.2.3). This is exemplarily shown in figure 6.6a. The range is chosen by using the linear part of the curve at the initial rise,

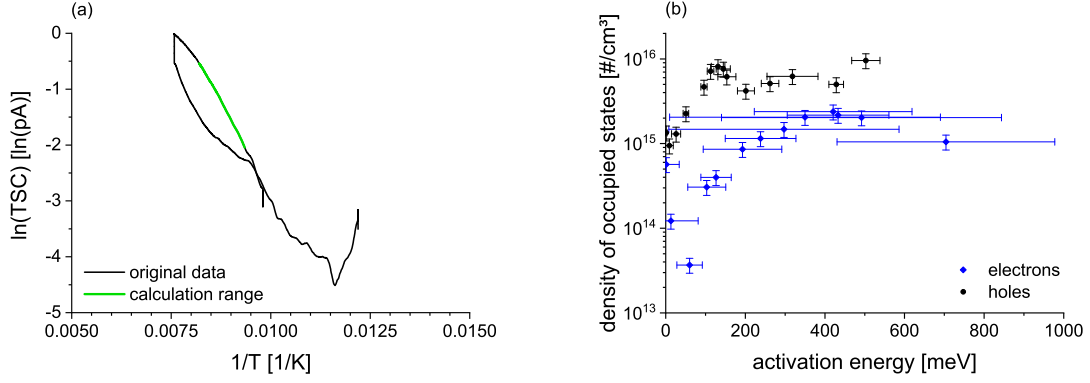


Figure 6.6: (a) Example plot for calculation of the activation energy. (b) Trap distribution determined from figure 6.5.

where the signal rises above the noise level.

This manual method may be vague, especially, if the linear part of the signal is short or includes measurement artifacts. For the estimation of the error the following method is used. the range of the regression, which is used to calculate E_a , is moved by 1 K up and down and E_a is calculated again. Additionally, the width of the regression range is increased 2 K for both moved ranges to get two more values for E_a . The resulting maximum deviation for E_a is chosen as the error.

The density of occupied trap states is calculated by integrating the current over time as described in chapter 2.2.5. The error for the density results from the uncertainty of the volume and current measurement.

For the approximation of the error caused by the current measurement and integration over time, the total amount of trapped charged carriers for the fractional and enveloping measurement can be compared. Ideally, the result from integrating both measurements over the total measurement time should be equal for the case at hand. In case of holes, it is $5.9 \cdot 10^{16} \frac{1}{\text{cm}^3}$ for the enveloping and $7 \cdot 10^{16} \frac{1}{\text{cm}^3}$ for the fractional method. This is an 18 % deviation for the total density of occupied trap states. However, this deviation is reduced if normalized to the amount of single fractional measurements, which is equal to 14. The resulting average deviation for the density of occupied trap states is 1.3 %.

The uncertainty of the volume measurement results from thickness and area uncertainties. The thickness is determined with profilometer measurements (Chap. 5.1), which has generally a deviation of 10 % caused by surface roughness. The area is determined by taking a picture of the whole sample. As the size of the substrate is known, the area of the semiconductor can be measured with this picture. Because of the width of the visible semiconductor edges, there is another 10 % uncertainty. The combined deviation

of 20 % is much larger than the deviation caused by current integration. Consequently, the latter can be neglected.

Figure 6.6b summarizes the densities of trapped charge carriers determined from the fractional MIS-TSC measurements of figure 6.5.

In case of the hole trap density distribution, a maximum at 170 meV and 400 meV is visible. The third peak at 500 meV is correlated with the maximum measured temperature of 300 K. The electron trap distribution shows a peak below 50 meV. This shallow trap level is not discussed in literature, probably because it is not visible using the classical TSC approach as a consequence of recombination.

The major peak with a broad distribution is at 450 meV. This level can be explained with the oxygen trap state at 600 meV discussed by Nicolai et al. [112] (Chap. 2.1.3). The difference to the Nicolai-level is almost within the error bars shown here and also explainable with the broad trap distribution.

With the MIS-TSC method it is not possible to determine if those defects are located in the bulk or on the P3HT / dielectric interface. To investigate the interface influences, a thorough analysis of different dielectric materials would be necessary. This aspect is not important in this thesis, as the trap distribution of pristine and degraded samples is compared, which have all the same interface. Consequently, the Calcium passivation (Chap. 6.2.3) is not used in the samples for the investigation of oxygen and water dependent trap states.

However, the trap occupation probability at the interface and in the bulk is unknown. This is important as the bulk trap states are essential for the correlation to the mobility. A method for increasing the bulk trap occupation probability is discussed in the following chapter 6.2.5

6.2.5 Dependence of TSC on the charging procedure

The total amount of trapped charge carriers ($5.9 \cdot 10^{16} \frac{1}{\text{cm}^3}$ for holes in chapter 6.2.4) is significantly lower than the maximum density of introduced charge carriers ($1.25 \cdot 10^{17} \frac{1}{\text{cm}^3}$ in case of an assumed homogeneously distributed charge density (Chap. 6.1.2)) during the charging process. Thus, a complete filling of all trap states is possible. However, as discussed in chapter 6.1.2, the inhomogeneous distribution of charges may cause an incomplete trap filling of the bulk.

For the charging procedure with constant V_{ch} as described in chapter 6.1.4, the amount of charge carriers at the organic semiconductor/ SiO_2 interface will increase with V_{ch} . As the sample is fully charged before cool down, the amount of charge carriers is constant at

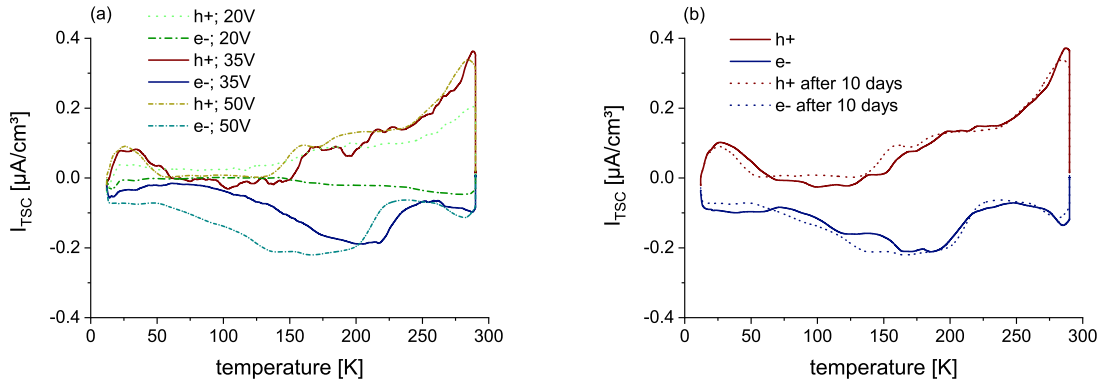


Figure 6.7: (a) Comparison of different V_{ch} and (b) comparison of two measurements before and after a 10 days long measurement sequence.

the interface during the charging procedure. An increased amount of charge carriers at the interface will cause higher diffusion currents and thus offers the possibility of higher bulk trap occupation.

Figure 6.7a shows MIS-TSC signals measured with different V_{ch} (20 V, 35 V, 50 V). In case of holes, the TSC is similar for 35 V and 50 V. Thus, a saturation is reached and a complete trap filling is assumed. For $V_{ch} = 20$ V, the TSC is lower and therefore, no complete filling is reached. Considering the electron signals in figure 6.7a, a larger dependency on V_{ch} is visible. At $V_{ch} = 20$ V, almost no trap states are filled. Possible explanations for this is the lower mobility of electrons compared to holes (Chap. 2.1.3), thus diffusion is less efficient because the diffusion coefficient is correlated to the mobility by the Einstein relation (Equ. 3.6). A further reason for the higher dependence on V_{ch} for the electron TSC might be the formation of space charge in the n-Si and thus capacitance reduction (Chap. 6.2.3). In agreement to the hole measurements, the most efficient filling is accomplished at the highest voltage of $V_{ch} = 50$ V. The higher TSC of $V_{ch} = 35$ V at around 220 K is caused by retrapping. As less trap states are filled for $V_{ch} = 35$ V compared to $V_{ch} = 50$ V, the free trap states cause a slower charge extraction by trapping and thus a shift of the signal to higher temperature.

Differences of the discussed signals may also be caused by aging, as the measurement duration for two curves is approximately 1 day. This aspect is analyzed with repeated measurements for both electron and hole trap states 10 days later (Fig. 6.7b). In between, the other measurements for evaluation of the charging process were done (fig. 6.7 and 6.8). Figure 6.7b substantiates neglectable aging influences as both signals are almost identical.

The low bulk occupation probability with constant V_{ch} can be increased by introducing

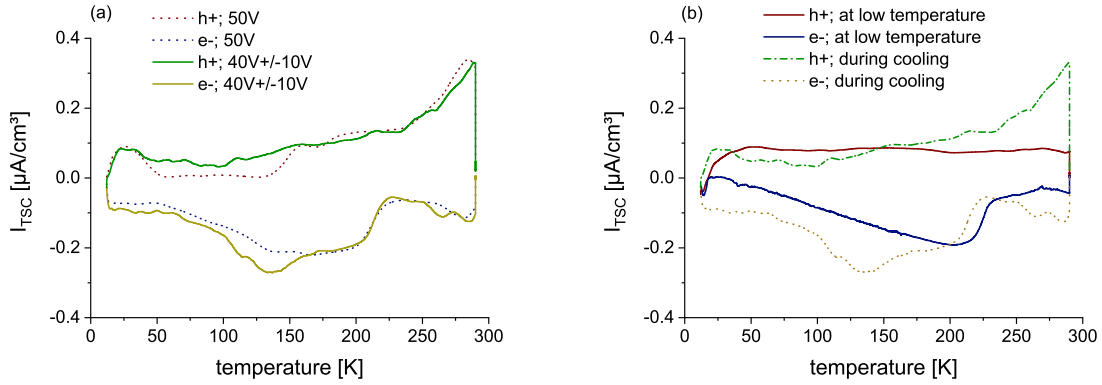


Figure 6.8: (a) Comparison of V_{ch} and $v_{ch}(t)$. (b) Comparison of using $v_{ch}(t)$ only at low temperature and during cool down.

drift currents. For this purpose, a slow oscillation of the charging voltage ($v_{ch}(t)$) during cool down can be applied (Chap. 6.1.4). This is shown in comparison to the measurement with $V_{ch} = 50\text{ V}$ in figure 6.8a. For both, electrons and holes, an even higher TSC is visible, substantiating a more efficient trap filling for both carrier types. Especially trap states located far away from the interface to SiO_2 are more likely occupied by this charging method as the charge carrier density caused by diffusion reduces strongly with the distance to the interface.

Principally, trap filling is also possible at low temperatures. If the trap filling with $v_{ch}(t)$ has a similar efficiency if performed at a constant low temperature is investigated in figure 6.8b. In the case of trap filling at low temperature, a considerably lower TSC signal is visible, especially for deep trap levels. As the mobility generally decreases with temperature (Chap. 2.1.2), the filling of trap states becomes less efficient at low temperatures, as discussed in chapter 2.2.2. Probably, with a longer charging time, the TSC becomes independent on whether $v_{ch}(t)$ is applied at low temperature or during cool down.

In conclusion, using $v_{ch}(t)$ during cool down is the most efficient charging process for bulk trap filling. Consequently, this process is used for the measurements analyzing oxygen and water dependent trap states.

6.3 Transient SCLC measurement circuit

In this thesis, the transient SCLC method as described in chapter 2.3.2 is used for determining the charge carrier mobility of organic semiconductors. The advantage of this method is the measurement direction of the current perpendicular to the thin film

plane, which is the current direction of typical device architectures, e. g. OLEDs or solar cells. Comparable to such devices, high current densities are required for this measurement method. As the mobility depends on the charge carrier density, the resulting mobility is a relevant material characteristic. Furthermore, the precision of this method is higher compared to the steady state SCLC method, which is analyzed in chapter 6.5.

However, a major drawback for transient SCLC is the need for a very low RC time constant for charging the device. For quantifying this challenge, a device with the following typical parameters is assumed: $d = 150 \text{ nm}$, $A = 2 \text{ mm}^2$, $\epsilon_r = 3$ and $\mu_0 = 10^{-4} \frac{\text{cm}^2}{\text{Vs}}$. With a step voltage of 5 V , a transit time of 360 ns results from equation 2.27. The RC time constant for this device with a serial resistance of 100Ω and the capacitance calculated with equation 2.18 is 33 ns . Szymanski et al. [154] showed that the transit time has to be at least 10 times larger than the RC time constant. Consequently, the assumed device would be on the edge of the measurement range while devices with higher mobility or lower film thickness are not measurable. For a larger range, a reduction of the RC time constant is necessary.

Apart from the device RC time constant, the measurement setup may have a large influence. Serial resistances and parasitic capacitances will increase the effective RC time constant. Consequently, this makes the use of a standard pulse generator with a typical 50Ω output resistance difficult. Additionally, the length of wires has to be as short as possible and the use of coaxial cables results in a high parasitic capacitance. Furthermore, the input capacitance and resistance of current measurement devices has to be considered, as well as the resistance and capacitance of the device under test contact metallization. In conclusion, the total RC time consisting of device charging and setup influences has to be reduced.

First, the device under test is considered for improving the total RC time. The sample capacitance can only be reduced by a smaller device area, as the film thickness is technologically limited (Chap. 4.4.1). However, the device area is limited by an increase in sample resistance and a consequent current signal reduction. Consequently, the measurement becomes more challenging in respect to the noise level. Furthermore, influences of device edges like spreading of the electrical field become more prominent with smaller areas. Thus, this concept of device capacitance reduction is not used in this thesis.

Minimizing the mostly setup dependent serial resistance is crucial for improving the minimum measurable transit time. There are approaches for solving this challenge, such as using bridge circuits [28, 89, 154] or an operational amplifier used as a trans-

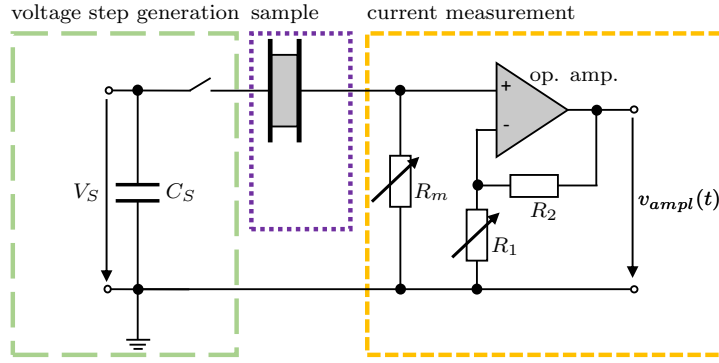


Figure 6.9: Simplified circuit for the transient SCLC measurement divided into three parts: step generation (Fig. 6.11), sample (Fig. 6.12) and current measurement (Fig. 6.13) [133].

impedance amplifier [154]. However, bridge circuits require a calibration for every new sample and trans-impedance amplifiers directly influence the SCLC signal, limiting the usefulness of the measurement [28, 154].

For quantifying the necessary voltage range for a measurement setup usable for a wide range of materials, the following example calculations are done. For the device described above, a current of 4.4 mA can be expected (Equ. 2.17). In case of a significantly lower mobility of $10^{-6} \frac{\text{cm}^2}{\text{Vs}}$, the current would be in the range of a few μA . Furthermore, as $I \propto d^{-3}$, the current increases strongly with thinner layers. If possible, measuring a thick layer is preferable as there are less non-ideal influences. To generate the same average electrical field strength compared to the 150 nm thick device at 5 V, 30 V are necessary for a 1 μm thick device.

Here, a transient SCLC measurement circuit is introduced in figure 6.9 [133], which allows for a low RC time constant even for thin semiconductor layers. Furthermore, the circuit meets the requirements of current and voltage range.

The circuit consists of three parts: voltage puls generation, sample connection and current measurement. The magnitude of the applied voltage step is set by the supply voltage V_S , which is stabilized by the capacitance C_S . In series to the voltage step generating switch, there is the sample and the measurement resistance R_m . The voltage over R_m is amplified by an amplification circuit using an operational amplifier (op. amp.). The amplification factor is set by choosing the resistance R_1 and the resulting voltage $v_{\text{ampl}}(t)$ is measured over time. The detailed function and layout of all three circuit parts is explained in the following chapters.

This circuit is implemented on a single printed circuit board (PCB) and positioned into an electromagnetically shielded box (Fig. 6.10). The resulting short wire length

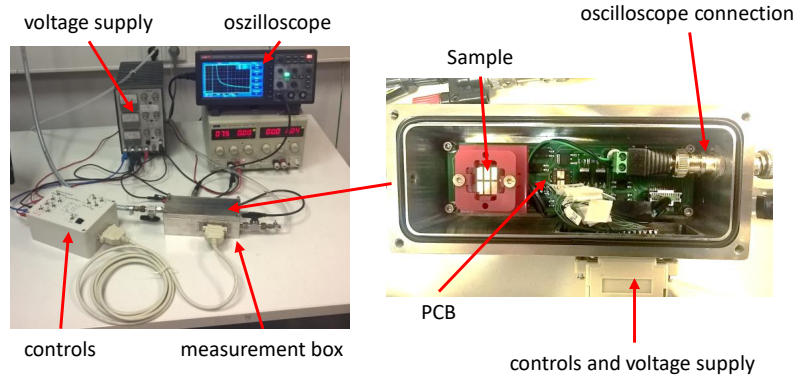


Figure 6.10: Picture of the transient SCLC measurement setup. The oscilloscope is the model UTD2052 from UNI-Trend.

and shielding reduces the influence of the environment. Furthermore, a pure nitrogen atmosphere can be ensured in this box and the sample loading can be done in nitrogen atmosphere within a glove box. The measurement circuit is manually controlled with an additional external box (App. 8.4).

The circuit and PCB layout is shown in the appendix 8.4. There, all devices used in the circuit are listed and the controls are described.

6.3.1 Details of the voltage step generation circuit part

Figure 6.11 illustrates the circuit part (Fig. 6.9) generating the voltage step. The voltage stabilizing C_S consists of an electrolyte ($C_{P,e} = 100 \mu\text{F}$), a foil ($C_{P,f} = 220 \text{ nF}$) and a ceramic capacitor ($C_{P,c} = 470 \text{ nF}$). This prohibits oscillations of V_S as the combination allows for a high total capacitance and simultaneously fast response time. The parallel resistor to C_S with $R_{dch1} = 5.36 \text{ M}\Omega$ enables C_S to discharge when V_S is turned off.

The voltage step is generated by switching the transistor T_{PULS} (55 ns rise time [44], IRFR9024NPBF, Infineon Technologies). To accomplish a wide voltage range of 3.5 V to 50 V, the gate potential of T_{PULS} is coupled to V_S . The transistor is switched on if the gate-source voltage is larger than 3.5 V (minimum of V_S), which is accomplished by applying 15 V to the gate of the transistor T_{20} by using a manual switch. With this, the gate of T_{PULS} is set to ground potential and the load current on this branch is limited by the resistance $R_{step} = 1 \text{ k}\Omega$. As the gate source voltage of T_{PULS} is limited to 20 V [44], which is guaranteed by the Zener diode Z_S , a second transistor circuit is used for $V_S > 20 \text{ V}$. By applying 15 V to the gate of the transistor T_{50} , the voltage divider with the resistors R_{step} and $R_{50} = 1.5 \text{ k}\Omega$ keeps the gate source voltage below 20 V.

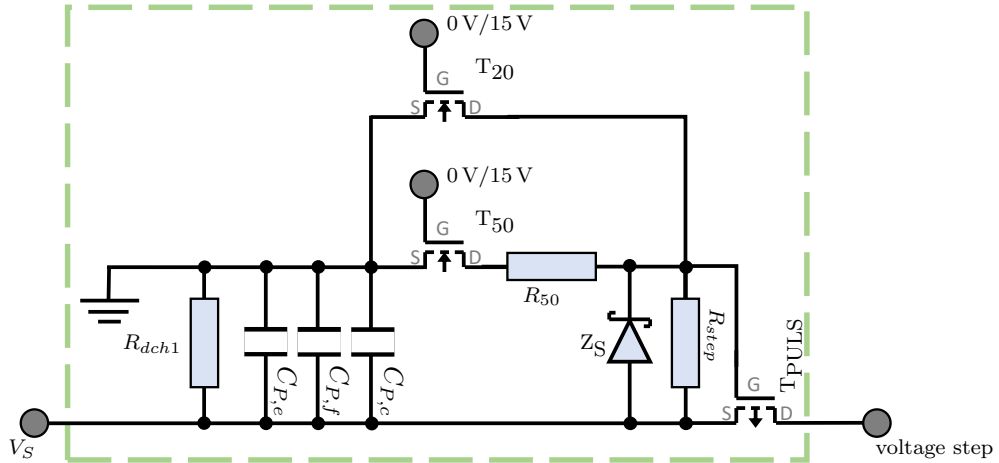


Figure 6.11: Circuit part: Voltage step generation of the circuit shown in figure 6.9. The voltage step is generated by opening the transistor T_{PULS} .

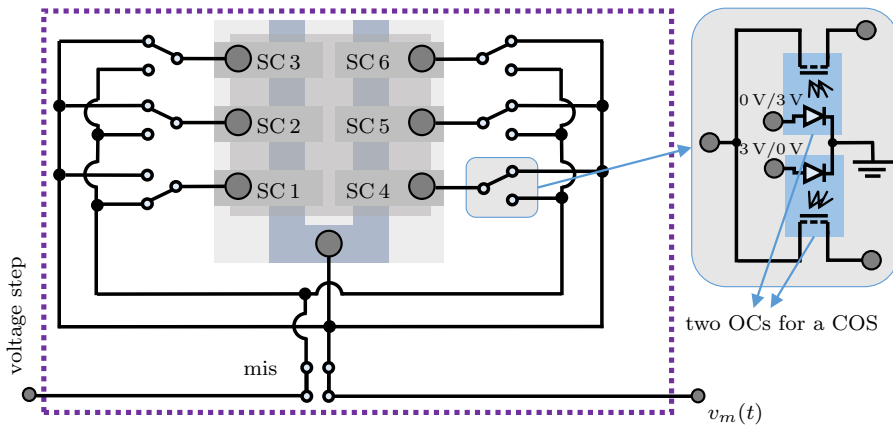


Figure 6.12: Circuit part: device connection in the circuit shown in figure 6.9. Every device (C1 to C6 (Fig. 4.1)) of the sample is connected to a changeover switch (COS) and each COS consist of two optocouplers (OC). When one OC is turned on and the other off, the device is either in shortcut with the bottom contact or it is measured. A mechanical intermediate switch (mis) allows for inverting the applied voltage and therefore, the measurement direction.

6.3.2 Details of the sample connection circuit part

Here, the connections to the device under test are described (Fig.6.12). For these connections, spring contacts (SC) are used for each metal pad of the sample. As the samples have six devices (Chap. 4.2), there have to be switches to choose any contact of those. To avoid parasitic capacitances, each device which is not measured is put

into a short circuit with the bottom contact. For low input capacitances of the switches, optocouplers (AQY212EHA, Panasonic) with naturally low capacitance (0.8 pF) and low on-state resistances (0.85Ω) are used [43]. The optocouplers are controlled by manually applied voltages. This setup allows for the parallel measurement of several devices, which can be used in case the current of one device is too low for the measurement. With the manual intermediate switch (mis), the direction of the voltage at the devices can be chosen in either direction.

6.3.3 Details of the current measurement circuit part

The circuit part in figure 6.13 is responsible for measuring the current. The voltage $v_m(t)$ over R_m is amplified by the op. amp. (LM6171, Texas Instruments [45]), which decouples the oscilloscope from the current signal. This allows for a low R_m and makes the influence of the amplification circuit on the current signal neglectable. The measurement resistance R_m can be chosen to be either 10Ω or 300Ω . Here, the same optocouplers as in chapter 6.3.2 are used to choose R_m and to reduce parasitic capacitances and serial resistances. The additional serial resistances to R_m including wiring and contact metallization is 7Ω .

Ideally, the amplification can be calculated with equation 6.5 [79]. To reduce back coupling between the oscilloscope and the op. amp., which would cause oscillations, an additional resistance $R_{osci} = 300 \Omega$ is set in between. The maximal allowed input voltage (which is $v_{ampl}(t)$ here) of the op. amp. is 15 V and is ensured by the Zener diode Z_M .

$$v_{ampl}(t) = \left(1 + \frac{R_2}{R_1}\right) \cdot R_{mess} \cdot i(t) \quad (6.5)$$

By using Ohm's law at R_m (Equ. 6.6), the analytical relation between the current $i_m(t)$ over R_m and $v_{ampl}(t)$ is given by equation 6.7.

$$v_m(t) = R_m \cdot i_m(t) \quad (6.6)$$

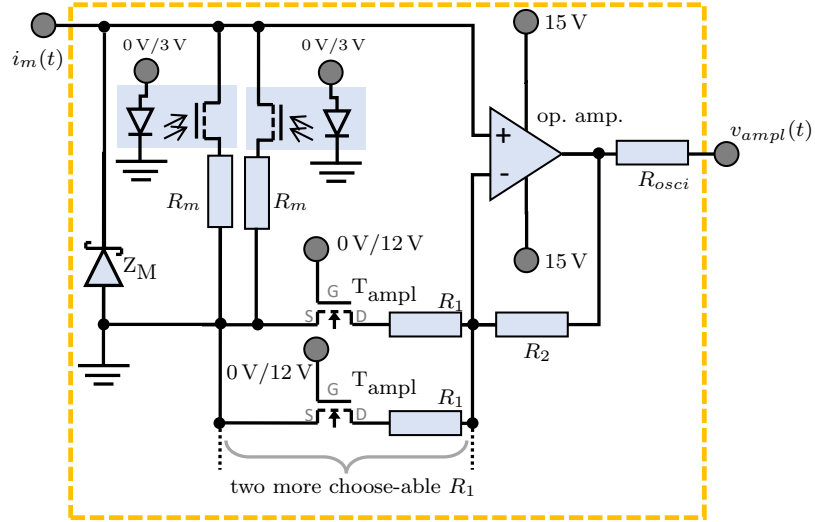


Figure 6.13: Circuit part: current measurement in the circuit shown in figure 6.9. The amplification can be chosen by changing the resistance R_1 .

$$v_{ampl}(t) = \left(1 + \frac{R_2}{R_1}\right) \cdot v_m(t) = \left(1 + \frac{R_2}{R_1}\right) R_m \cdot i_m(t) \quad (6.7)$$

There are 5 different selectable R_1 by manually applying 12 V to the transistors T_{ampl} : infinite resistance by open clamps ($\rightarrow \infty$), 174Ω , 34.8Ω , 8.06Ω and 2Ω . In figure 6.13, only two possible R_1 are shown, two more identical circuit parts consisting of T_{ampl} and R_1 are contacted in parallel. In combination with the two possible R_m , the measurable current ranges shown in table 6.1 are accomplished. The minimum detectable current is defined by the noise level of the oscilloscope, which is at $10 \mu\text{V}$ and used for the minimum $i_m(t)$ in table 6.1. Close to the noise level, an average signal of several measurements is necessary. For a measurement with a better signal to noise ratio, a higher amplification should be chosen if possible. The maximum voltage for $v_{ampl}(t)$ is 15 V, as that is the maximum output voltage of the op. amp., defining the maximum $i_m(t)$.

For calibration of this setup, a resistor in series with a parameter analyzer (Keithley 4200-SCS) is used instead of a sample. By using a linear regression, an exact relation between current and $v_{ampl}(t)$ is found (App. 8.4).

Table 6.1: Current range for all amplifications of the transient SCLC circuit.

R_m	R_1	amplification (Equ. 6.7)	minimum $i_m(t)$	maximum $i_m(t)$
10 Ω	$\rightarrow \infty$	10 $\frac{V}{A}$	1 μA	500 mA
10 Ω	174 Ω	44.7 $\frac{V}{A}$	224 nA	330 mA
10 Ω	34.8 Ω	184 $\frac{V}{A}$	54.3 nA	81 mA
10 Ω	8.06 Ω	759 $\frac{V}{A}$	13.2 nA	20 mA
10 Ω	2 Ω	3030 $\frac{V}{A}$	3.3 nA	5.0 mA
300 Ω	$\rightarrow \infty$	300 $\frac{V}{A}$	33.3 nA	50 mA
300 Ω	174 Ω	1341 $\frac{V}{A}$	7.46 nA	11 mA
300 Ω	34.8 Ω	5520 $\frac{V}{A}$	1.81 nA	2.7 mA
300 Ω	8.06 Ω	22770 $\frac{V}{A}$	0.439 nA	0.66 mA
300 Ω	2 Ω	90900 $\frac{V}{A}$	0.11 nA	0.17 mA

6.4 Benchmarking of the transient SCLC circuit

For benchmarking the developed circuit for transient SCLC measurements described in chapter 6.3, the hole mobility of MTDATA is measured as proof of principle. Furthermore, the measurement limits are determined. The MTDATA sample structure is described in chapter 4.2.1. Here, different thicknesses of the MTDATA layer are used: 76 nm, 123 nm, 253 nm, 322 nm, 642 nm and 904 nm.

6.4.1 Mobility from steady state SCLC

To validate the mobility determined by transient SCLC (Chap. 2.3.2), a reference mobility value is needed. This reference is the mobility determined with the steady state SCLC method (Chap. 2.3.1). For this purpose, the diode (JV) characteristics of the devices under test are illustrated in figure 6.14 in double logarithmic form. The measurement procedure is described in chapter 5.2. For thick samples (642nm and 904nm), the determined gradient of the double logarithmic plots is approximately 2.3, which marginally increases with high voltages because of the field dependence of the mobility (Chap. 2.3.3). These samples can be considered as almost ideal. Thus, the steady state

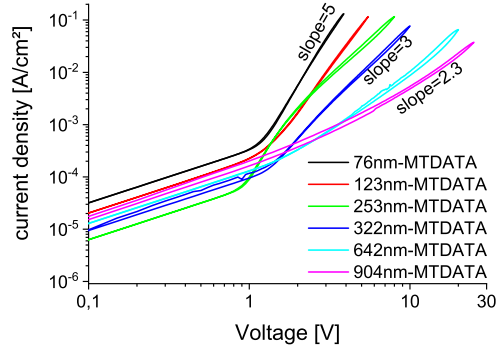


Figure 6.14: JV curves of MTDATA hole only devices with different film thicknesses of MTDATA in double logarithmic plot. The gradient increases for thinner layers.

mobility determined with equation 2.17 is a valid approximation. For thinner layers, the gradient of the JV-characteristic increases up to values of 5. As this is probably not the influence of a different microstructure of MTDATA for varying film thicknesses, as outlined in chapter 4.1, the influence of other non-ideal parameters is responsible. These parameters can be e. g. the existence of an injection barrier or the influence of a built-in field (Chap. 2.3.3) [1].

Despite a gradient larger than 2, equation 2.17 can be used to estimate a minimum mobility (Chap. 2.3.3). This ideal equation generally describes the maximum possible current for a device. In case of high influences of non-ideal parameters, the current will decrease compared to the ideal value. Consequently, if the mobility is calculated with this method, a too low value is determined.

The mobility values for the curves in figure 6.4.2 range from $2.5 \cdot 10^{-5} \frac{\text{cm}^2}{\text{Vs}}$ (for $d = 76 \text{ nm}$) to $1.4 \cdot 10^{-4} \frac{\text{cm}^2}{\text{Vs}}$ (for $d = 904 \text{ nm}$) with assumed $\epsilon_r = 3$ [22, 29].

6.4.2 Transient SCLC measurement procedure

For measuring the transient SCLC using the circuit outlined in chapter 6.3, a suitable amplification has to be chosen for every V_S . This means, that the amplified voltage $v_{\text{ampl}}(t)$ has to be in the measurement range of the oscilloscope. For measuring a single transient SCLC curve, five measurements are done with the same setting. If the five curves are similar to each other, an average curve of these five measurements is calculated.

Figure 6.15a illustrates an exemplary transient SCLC measurement of a 322 nm thick MTDATA device for V_S values ranging from 6 V to 14 V and $R_m = 10 \Omega$. For $V_S = 6 \text{ V}$ to 8 V, the amplification factor $759 \frac{\text{V}}{\text{A}}$ is used and for $V_S = 10 \text{ V}$ to 14 V the factor

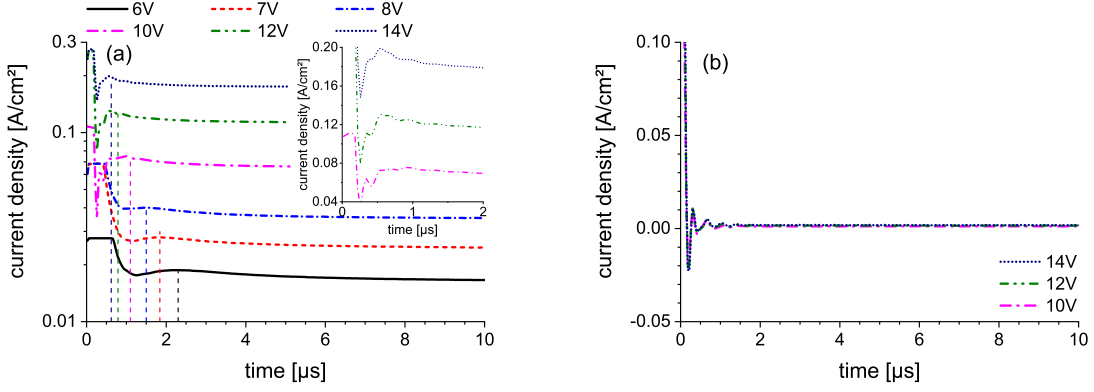


Figure 6.15: (a) Transient SCLC measurement of a 322 nm thick MTDATA layer. Voltages 6 V to 8 V are measured with high amplification of $759 \frac{\text{V}}{\text{A}}$ and voltages 10 V to 14 V are measured with low amplification of $184 \frac{\text{V}}{\text{A}}$. The inset shows the magnification of the 10 V, 12 V and 14 V measurements with the oscillation of the operational amplifier caused by low amplification (high band width). (b) Reference measurement: Result without any sample connected to the circuit (open clamps). The signal is almost the same for all voltages.

$184 \frac{\text{V}}{\text{A}}$. The vertical dashed lines indicate the positions of t_{trans} for each value of V_S .

For $V_S = 6 \text{ V}$, there is a smooth peak visible in the transient signal, from which the mobility can be calculated using equation 2.27. During the first 700 ns of the transient, $v_{ampl}(t)$ is in the oscilloscope compliance because of the high charging peak. This does not influence the device current as discussed in chapter 6.3. The width of this charging peak can be compared to the following theoretical estimation of the RC time constant t_{RC} . This constant can be calculated with the device capacitance (Equ. 6.8) with $\epsilon_r = 3$ [22, 29], thickness $d = 322 \text{ nm}$ and area $A = 7.5 \text{ mm}^2$. With the serial resistance of 17Ω (Chap. 6.3.3), the result is $t_{RC} = 11 \text{ ns}$. After approximately $10 \cdot t_{RC} = 110 \text{ ns}$, the charging peak should decline completely. In contrast, the measured charging peak is broader than 700 ns. This broadening of the charging peak results from the low band width and therefore slow response of the amplification circuit. Generally, the amplification factor influences the band width of the amplification circuit. A high amplification causes a low band width and vice versa [45].

$$C_{samp} = \epsilon_0 \cdot \epsilon_r \cdot \frac{A}{d} \quad (6.8)$$

The amplification used for $V_S = 6 \text{ V}$ works up to $V_S = 8 \text{ V}$. For $V_S > 8 \text{ V}$, the charging peak starts to overlap the transient peak. Consequently, a lower amplification is neces-

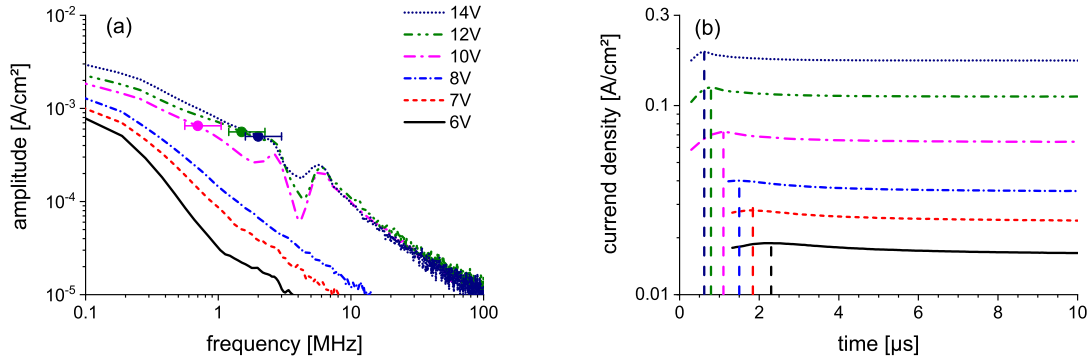


Figure 6.16: (a) Amplitude of the fast Fourier transformation of the transient SCLC signals from figure 6.15a. High voltages above 12 V show some peaks above a certain frequency. The dots mark the cut off frequency for the FFT low pass filter used for smoothed transient SCLC signals shown in (b). For estimation of the deviation of this filtering a range of -20 % to +50 % (horizontal error bars) of the cut off frequency is tested.

sary, which results in a higher bandwidth and faster response time of the amplification circuit. However, this causes an oscillation of the operational amplifier that overlaps the actual signal, which is better visible in the inset of figure 6.15a.

In order to analyze the origin of the oscillations in more detail, the measurement shown in figure 6.15a is repeated in open circuit conditions without a sample. This reference measurement (Fig. 6.15b) shows a similar oscillation, which is almost independent on V_S . In the case of open clamps, the oscillation is caused by charging parasitic capacitances within the circuit or by ground potential instability. By subtracting the open clamp reference from the actual transient measurements, the influence of the oscillation can be reduced, however, not completely avoided. In order to further improve the oscillation suppression, the transient signals from figure 6.15a are analyzed after open circuit correction in the frequency domain obtained by fast Fourier transformation (FFT) [32] (Fig. 6.16a).

For $V_S \leq 8$ V, the amplitude has a smooth, almost linear characteristic. For higher V_S , additional peaks occur which can be ascribed to the detected oscillations in the time domain. These peaks can be filtered with a low pass filter using a cut off frequency f_{cut} just below those peaks, which are indicated by the dots in figure 6.16a. Here, the FFT-filter for smoothing curves provided by OriginPro 2018b (OriginLab Corporation) is used. The mathematical principle of this filter is explained in the appendix 8.5.

The influence of using this filter in the time domain is illustrated in figure 6.16b. The signal is no longer influenced by parasitic oscillations and the calculation of the mobility

with equation 2.27 is now possible. However, the transient peak maximum required for the charge carrier mobility extraction is slightly influenced by f_{cut} , thus choosing the correct f_{cut} is not trivial. The magnitude of this influence is evaluated by calculating the mobility with $0.8 \cdot f_{cut}$ and $1.5 \cdot f_{cut}$. The deviation of the determined mobilities from these shifted cut off frequencies is calculated in respect to the original mobility data. This results in a standard deviation for the derived mobility of 7%.

In the following, this deviation is compared to the deviation caused by thickness uncertainty. Because of surface roughness, the thickness of a semiconductor layer can only be determined with a typical standard deviation of 10%. Considering the quadratic relation in equation 2.27 and the error propagation, the resulting standard deviation caused by thickness uncertainty is 20% [22]. Thus, the correction done in the frequency domain causes less deviation than the original data set and therefore, the use of this correction is tolerable. The uncertainties of determining t_{trans} and of V_S are at 1% or lower. Consequently, these influences on the total deviation can be neglected.

6.4.3 Mobility results from transient SCLC measurements of MTDATA

In this chapter, the mobility results for different MTDATA layer thicknesses (76 nm, 123 nm, 253 nm, 322 nm, 642 nm and 904 nm) are discussed. Figure 6.17 illustrates the charge carrier mobility extracted from the transient SCLC measurements in correlation to the average electrical field strength using the measurement procedure described in chapter 6.4.2. Half-full symbols mark the mobility determined from transient SCLC without FFT correction and full symbols mark the data with FFT correction. The error bars do include the uncertainty of the layer thickness of MTDATA and the deviation caused by the FFT correction if used. For comparison, the estimated mobility from the steady state SCLC in chapter 6.4.1 is marked by the empty symbols on the right side of the diagram, which can not be correlated to a certain electrical field strength. The error bars of the steady mobility values consider the measured thickness deviation and the standard deviation calculated from the measured 6 devices per sample.

The errors caused by idealization of the theory e.g. neglecting the contact resistance or trap states (Chap.2.3.3), are not considered for the mobility determination. Consequently, an increase of the mobility with higher electrical field strength is visible. Furthermore, the mobilities determined for thin layers (76nm and 123nm) are much smaller than for the thicker layers. This is the consequence of the large influence of the

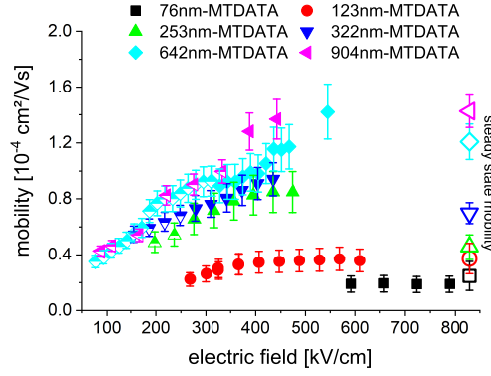


Figure 6.17: From transient SCLC measurements calculated mobility for different film thicknesses of MTDATA: The error bars result from the deviation of the FFT filtering and thickness uncertainty. Empty symbols mark the mobility determined from steady-state SCLC and are not correlated to a specific electrical field strength. Half-empty symbols mark measurements without FFT correction and full symbols with FFT correction.

serial resistance as it is discussed later in chapter 6.5.

In spite of the non-ideal influences of the measurement, these results can be used for benchmarking the circuit. The obtained transient mobility values are in good agreement to the steady state mobility, which has a high reliability for devices with thick layers as they have an almost ideal behavior as discussed in chapter 6.4.1. The steady state mobility correlates better with the transient mobility at high electrical field strength, which makes sense as the steady state mobility is from the part of the IV curve with a high electrical field strength, where the double logarithmic gradient is constant.

For further verification of the mobility results from the transient measurement, the values are compared to literature data in the following. So et al. found mobility values for MTDATA with the transient SCLC method of $6 \cdot 10^{-5} \frac{\text{cm}^2}{\text{Vs}}$ (at $0.036 \frac{\text{kV}}{\mu\text{m}}$) and $8 \cdot 10^{-5} \frac{\text{cm}^2}{\text{Vs}}$ (at $0.056 \frac{\text{kV}}{\mu\text{m}}$) [145]. These are similar to the mobility values obtained here for the thick MTDATA layers of more than 253 nm. The literature values are approximately 20% lower compared to the values obtained here. This might be caused by differences in the material or by the higher serial resistance of at least 50Ω and thus higher RC time constant in the measurement setup used by So et al. [145].

In conclusion, the accuracy of measuring thick samples is proven by these comparisons. The high variations of MTDATA sample thickness and consequently device resistances prove the significant flexibility of the circuit in terms of measurable currents and applicable voltages. As the current may change strongly with the mobility and film thickness of any semiconductor measured by the circuit, the implemented wide current

(1 μA to 0.5 A) and voltage range (3.5 to 50V) is a great advantage of the circuit.

However, for thin layers, the ideal theory is not applicable as the results for 76 nm and 123 nm are too low. This is not a problem with the measurement circuit, but with the used theory. The interpretation of the transit time has to be reworked, if thin and thick layers are to be compared. Nonetheless, the transient mobility of semiconductor layers of similar film thickness can be compared with this method and the circuit provide the possibility to measure the transit time of thin layers. The measurement limits are discussed in the following chapter 6.4.4.

6.4.4 Measurement range of the transient SCLC circuit

The measurements shown in chapter 6.4.3 suggest a minimum measurable transit time of $t_{trans} = 300$ ns. For lower t_{trans} , the transient current peak overlaps with the sample charging peak. Furthermore, this minimum t_{trans} can only be assumed, if the current is large enough for using a low amplification. However, in case of a high sample resistance at a thin layer, a high mobility is unlikely which would cause such a short transit time. Thus, using $t_{trans} = 300$ ns, the maximal measurable mobility can be estimated with equation 2.27, depending on V_S and d .

Figure 6.18 shows this maximum mobility. For thin layers of 100 nm to 250 nm, a mobility of $10^{-3} \frac{\text{cm}^2}{\text{Vs}}$ to $10^{-4} \frac{\text{cm}^2}{\text{Vs}}$ is measurable, which is a typical range for organic semiconducting polymers [22, 26, 29]. Thicker layers can be measured more easily, as t_{trans} increases with the thickness. In this case, high voltages are required, as a high enough amount of charge carriers has to be injected to generate the SCLC. As 50 V are possible with this circuit, thick layers of 1 μm with a mobility of $10^{-3} \frac{\text{cm}^2}{\text{Vs}}$ are measurable.

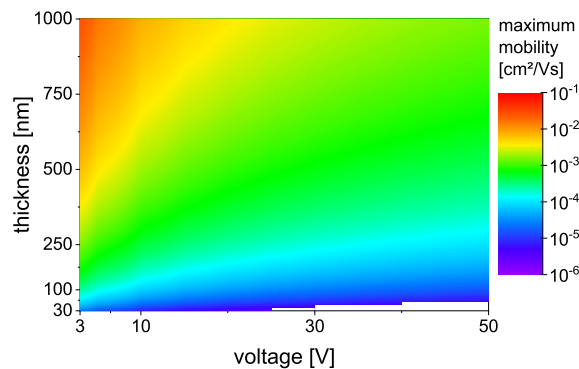


Figure 6.18: The minimum mobility measurable by the shown circuit in depends of applied voltage and device thickness with assumed $t_{trans} = 300$ ns

6.5 Simulation of space charge limited current

As discussed in chapter 2.3.3, the thickness has a significant influence on the determined transient mobility at thin films, causing too low mobility values. Here, the type of non-ideal influence responsible for the lower mobility is analyzed. For this purpose, the simulation method and parameter variations described in chapter 3 are used.

For reference purpose, an almost ideal, basic device is analyzed in chapter 6.5.1. With this devices, the transient and steady state SCLC methods are compared to each other. With this, the influence of the thickness on both methods is compared in order to characterize the accuracy of both methods at thin layers. In correlation to this basic device, each non-ideal parameter is analyzed separately for the transient SCLC method. These non-ideal parameters are: rise time of the voltage step function, intrinsic doping of the semiconductor, parallel resistance, built-in field, injection barrier and serial resistance.

6.5.1 Steady state and transient SCLC in the basic device

For the basic device, diffusion and space charge regions at contacts are considered as non-ideal parameters and which are neglected in the ideal theory (Chap. 2.3). Figure 6.19a shows the normalized transient mobility (as described in chapter 3.2) of all tested total density of states (DOS) and for $f_{atj} = 10^{12}$ Hz, $F = 0.03 \frac{\text{kV}}{\mu\text{m}}$. The marks are the simulated devices and the solid line the analytic fits, which are in good agreement with the data points with a standard deviation of 0.02. Figure 6.19b illustrates the normalized mobility determined from the steady state, calculated with equation 2.17, showing only the fit curves.

For comparison of the steady state and transient SCLC method, a 20 % deviation region is marked in figure 6.19. This range is typically caused by thickness uncertainty [22] (Chap. 6.4.2). Thus, a deviation caused by non-ideal parameters is neglectable if it is lower than 20 %.

The generally higher mobility visible for both methods at thin layers is primarily caused by the higher charge carrier density as visible in figure 6.20a. For a better comparability, the depth is normalized on the thickness of each device. The charge carrier density increases in the space charge regions at the contacts. Consequently, the transport energy is shifted in the direction of the middle of the Gauss profile, which is assumed in this simulation (Chap. 2.1.1). The larger amount of states available for the hopping process increases the hopping probability and hence the mobility. Furthermore,

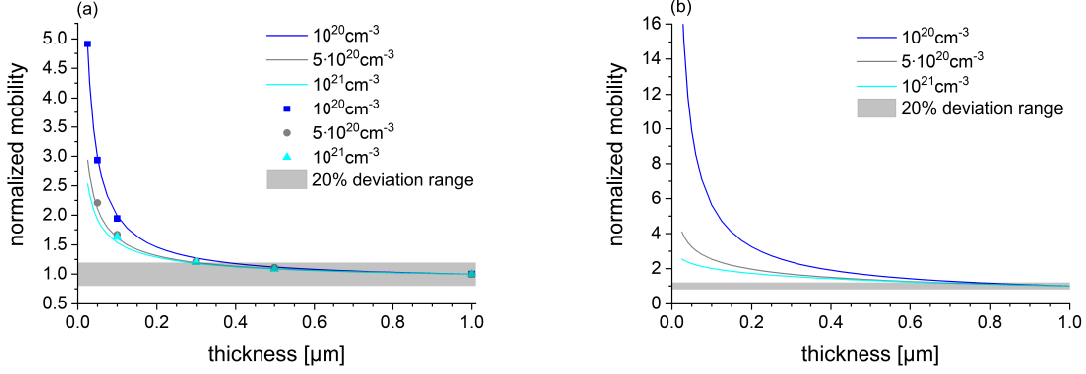


Figure 6.19: (a) Transient mobility normalized to the mobility of 1 μm thick layer. The solid lines are the fit (Chap. 3.2) and the symbols are the normalized mobility values determined from the simulated transient signal. (b) Normalized mobility determined from steady state IV curves.

the shift is larger for a low total DOS, as the same amount of charge carriers occupy the free states. Additionally, the gradient of the charge carrier density increases with lower thickness. This causes a higher contribution of the diffusion, which results in a faster transient of charge carriers [153]. Furthermore, the space charge regions at the contacts, due to the high conductivity here, cause a reduction of the effective thickness. For transient SCLC, as the determined mobility is proportional to d^2 , a too large d causes an overestimation of the mobility. For steady state SCLC, the proportionality is to d^3 and the effect even larger.

It is obvious, that the mobility increase at thin layers is much larger with the steady state approach than for the transient measurement. In case of steady state SCLC, the deviation is already larger than 20% at a relatively thick layer of 700 nm. Consequently, the transient method has the potential to be more accurate for thin layers compared to the steady state approach. Furthermore, from the shape of the signal, it is difficult to analyze non-ideal parameters as discussed in chapter 2.3.3. Thus, only the transient SCLC is considered in the following as it is more accurate at thin layers as also discussed by Weiß et. al [171].

As the average electrical field strength influences the charge carrier density, too, the mobility change at thin layers can be different for other field strength and f_{atj} than shown in figure 6.19a. Both parameters are considered in figure 6.21 for $N = 5 \cdot 10^{20} \frac{1}{\text{cm}^3}$. In both cases, the influence of the average F and f_{atj} is small.

Concerning figure 6.20a, for different average F at a 25 nm device, only a factor of 5 between intrinsic and injected charge carrier density is possible concerning $F = 0 \frac{\text{kV}}{\mu\text{m}}$

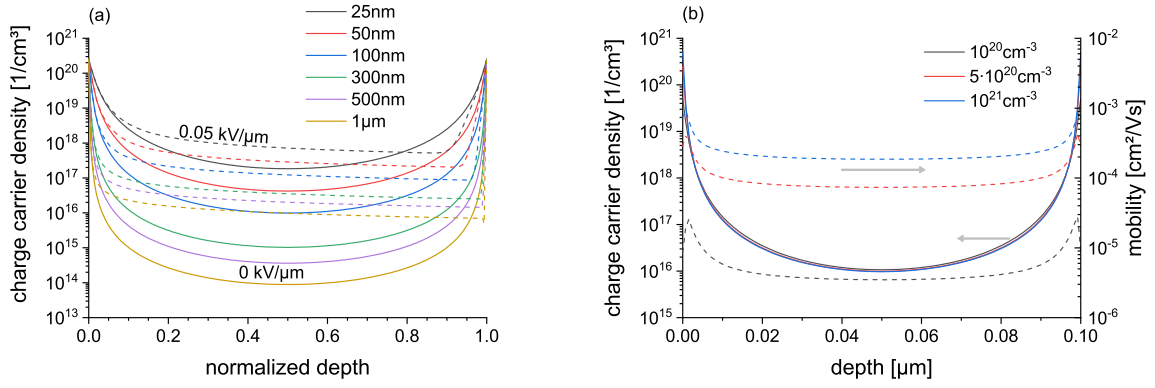


Figure 6.20: (a) Charge carrier density for $0 \frac{\text{kV}}{\mu\text{m}}$ (solid lines) and $0.05 \frac{\text{kV}}{\mu\text{m}}$ (dashed lines). Each curve is normalized to its device thickness. (b) Mobility and charge carrier density of a 100 nm thick device for different total DOS at $0 \frac{\text{kV}}{\mu\text{m}}$.

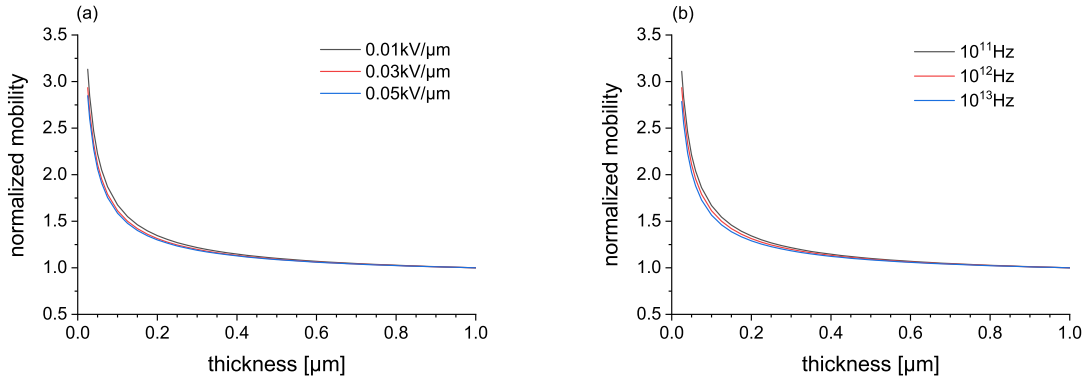


Figure 6.21: Influence of (a) F with $f_{atj} = 10^{12}$ Hz and (b) f_{atj} with $F = 0.03 \frac{\text{kV}}{\mu\text{m}}$ on the normalized mobility.

and $F = 0.5 \frac{\text{kV}}{\mu\text{m}}$. For $d = 1 \mu\text{m}$ and $F = 0.5 \frac{\text{kV}}{\mu\text{m}}$, there is a factor of 100 depending on the thickness. Thus, the magnitude of F has much less influence compared to d . Considering f_{atj} , the mobility is proportional to f_{atj} (Equ. 2.4) and the diffusion contribution does not change in the normalized plot. Furthermore, the change of mobility caused by injected charge carriers is independent on f_{atj} . The slightly lower mobility change for $f_{atj} = 13^{13}$ Hz at thin layers is caused by the lower device resistance and consequently lower influence of space charge regions at the contacts.

Consequently, the following analyses of other non-ideal parameters is done only with $F = 0.03 \frac{\text{kV}}{\mu\text{m}}$ and $f_{atj} = 10^{12}$ Hz. Furthermore, only $N = 5 \cdot 10^{20} \frac{1}{\text{cm}^3}$ is considered, as the general behavior is the same for all N .

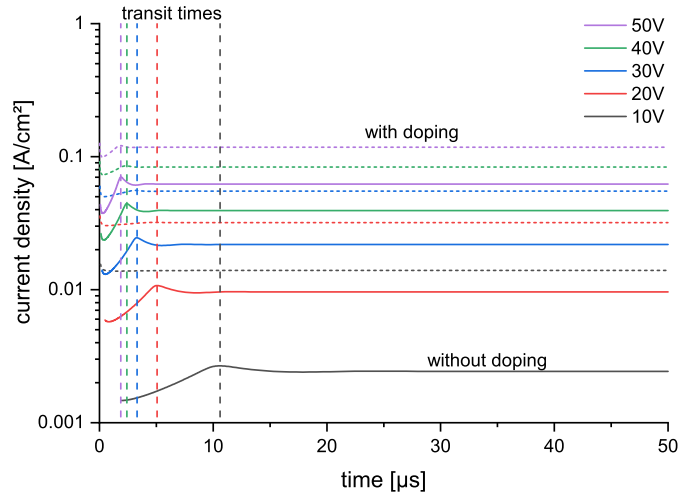


Figure 6.22: Transient signal of a 1 μm thick device: solid lines is without doping (basic device) and dashed lines is with a doping concentration of $10^{16} \frac{1}{\text{cm}^3}$.

6.5.2 Influence of doping and parallel current paths on the transient SCLC mobility

Usually, there is unintentional doping in real organic semiconductors [29, 93, 120, 153], which may influence the transient SCLC measurement. Here, this doping is assumed to be an additional amount of free charge carriers in the semiconductor. The effect of a doping concentration of $10^{16} \frac{1}{\text{cm}^3}$ on the transient signal of a 1 μm thick device is visible in figure 6.22. Here, the solid lines are the signal of the basic device and the vertical dotted lines mark the corresponding t_{trans} . It is obvious, that the position of the transient peak is not influenced by the doping. This is in line with the findings of Röhr et al. [129] for similar doping concentrations. However, the peak height is significantly decreased, which means the peak is no longer visible for a higher doping concentration. For lower doping concentrations, the effect will be reduced resulting in a signal more similar to the basic device.

In case of thinner layers, the effect of doping is smaller, as the injected amount of charge carriers is larger (Fig. 6.20a). Furthermore, the amount of charge carriers introduced by the contact space charge regions becomes larger than $10^{16} \frac{1}{\text{cm}^3}$ at layers thinner than 100 nm. Consequently, the discussed doping concentration has no effect.

Mathematically, the effect of doping on the transient current signal can be seen as a parallel current path which does not influence the transient current peak. The total signal is the superposition of the transient SCLC and the parallel current. This reduces

the relative peak height, as the peak current becomes smaller compared to the steady state current and the resolution of the peak becomes more difficult.

Consequently, a parallel resistance to the device under test has the same influence on the transient signal as the discussed doping. The voltage at the device is not influenced by this resistance and therefore, there is no influence on the transit time. If the transient peak is visible despite the parallel resistance, the determined mobility from the current peak is not influenced.

6.5.3 Influence of built-in field on transient SCLC

Because of technological reasons, it is not possible to use the same contact materials for charge carrier injection and ejection of a semiconductor layer. Typically, this results in a built-in field within the active layer. Therefore, the influence of such a built-in field on the transient SCLC signal is simulated here as described in chapter 3.2. The built-in field is described by the voltage V_{b-in} , which is the difference of the contact material work functions divided by q .

Figure 6.23 shows the effect of different built-in field on the simulated devices (solid lines) in comparison to the basic device (thick, gray line). For high built-in field strength, the measured mobility is reduced in comparison to the basic device. In case of $V_{b-in} = 0.2 \text{ V}$, there is no influence and for $V_{b-in} = 0.5 \text{ V}$, the reduction of the normalized mobility is only relevant below 150 nm. In case of $V_{b-in} = 1 \text{ V}$, the influence becomes large and causes further reduction. This reduction is caused by the different direction of built-in and external field. Consequently, the external field has to compensate the built-in field resulting in a reduced total field strength. For calculating the mobility with equation 2.27, the effective voltage is lower compared to the applied voltage.

As the built-in field is defined by the contact work functions and decreases with thicker layers, there is no influence on the mobility visible for the $1 \mu\text{m}$ thick devices. Furthermore, the influence of the constant built-in field decreases with higher voltages.

A typical correction for the built-in influence is $V_S - V_{b-in}$ for V_S in equation 2.27 [22]. This correction is used for the simulated data and shown as the dashed lines in figure 6.23. The correction results in a built-in field independent value, but the mobility is overestimated compared to the basic device. This might be caused by the smaller space charge region at the ejection contact compared to the basic device. Furthermore, the usefulness of this correction is limited for real devices, as the built-in field is strongly dependent on surface charges and usually not exactly known for a device [22].

In this thesis, the mobility of devices with similar thicknesses are compared to each

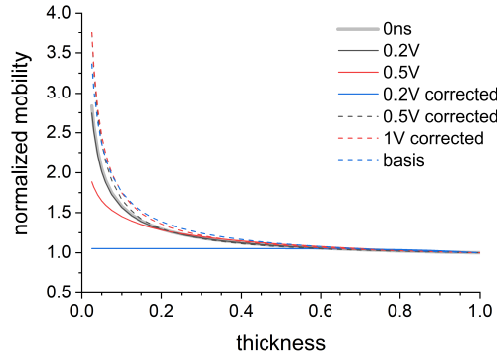


Figure 6.23: Different built-in fields (solid lines) and their corrected values (dashed lines). The thick, gray line is from the basic device. This basic signal is identical to the signal with a built-in field of 0.2 V.

other, which have the same contact materials. Thus, the influence of the built-in field is similar for all devices and V_{b-in} is probably in the range 0.3 eV to 0.5 eV (Fig. 4.4). In this range, the difference to the basic device is small compared to a higher built-in field. Consequently, a correction of mobility data for built-in field influences is not reasonable in this thesis.

6.5.4 Influence of injection barrier on transient SCLC

Depending on the quality of the injection contact, there is a barrier causing a voltage drop at this interface [9, 59, 89, 180]. Consequently, the average electric field strength is reduced within the semiconductor layer and as discussed before for the built-in field (Chap. 6.5.3), the mobility is reduced compared to the basic device.

The influence of the injection barrier on the mobility determined from transient SCLC is shown in figure 6.24. Up to 0.3 eV, the mobility reduction is small which is in agreement with the literature [9, 59, 89, 180]. This decrease is much stronger for a larger injection barrier of 0.5 eV. At this value, the determined mobility for thin layers is smaller than for the 1 μm thick layer.

As the injection barriers of the measured devices are smaller than 0.1 eV, considering the work functions of the electrodes and HOMO or LUMO levels (Fig. 4.4), the influence of an injection barrier is probably small. Furthermore, in case of high injection barriers and thus non ohmic contacts, the peak at the transit time in the transient SCLC signal is not visible in measurements of real devices [62, 89]. Consequently, injection barrier influences do not need consideration in the analysis done in this thesis.

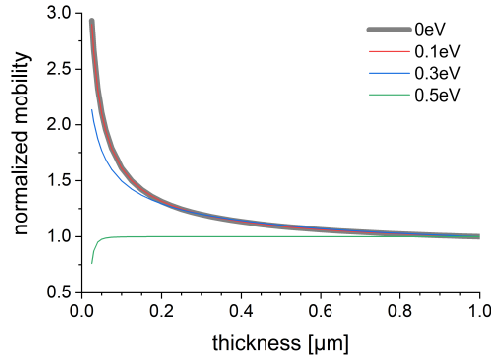


Figure 6.24: Normalized mobility for different injection barriers. The thick, gray line is from the basic device. This basic signal is identical to the signal with 0.1 eV injection barrier.

6.5.5 Influence of a non-ideal voltage step on the transient SCLC mobility

The shape of the voltage step is influenced by two factors. First, for real measurements, there is a rise time of the voltage step and no ideal, rectangular step function. Second, the RC time constant for sample charging causes a slow voltage increase at the device under test.

For the first factor, considering a non-ideal voltage step function, devices with a linear ramp instead of an ideal voltage step are simulated as described in chapter 3.2. Figure 6.25 shows the influence of different rise times on the normalized mobility in comparison to the basic device. It is obvious, that a longer rise time causes a lower determined mobility. Here, $t_{rise} = 20$ ns has almost no effect and $t_{rise} = 100$ ns shows a large decrease by factor 1.5. This lower mobility is caused by the lower electrical field strength at $t = 0$ at the beginning of the measurement compared to an ideal, rectangular voltage step function. Therefore, the transit time increases.

The mobility difference can be quantified with the relation shown in equation 6.9. The factor f_{rise} is the quotient of μ_r (determined with a non-zero rise time) and μ_0 (theoretically determined with an ideal voltage step). For substitution of μ_i , equation 2.27 is used, where t_{trans} is the transit time of the non-ideal voltage step function. The ideal transit time is considered to be a correction time t_{corr} shorter compared the device with rise time. As the devices of the two transient measurements have the same thickness d and voltage V_G , those contributions are cut and f_{rise} depends only on the measured t_{trans} and t_{corr} . Consequently, μ_0 is not needed to calculate f_{rise} .

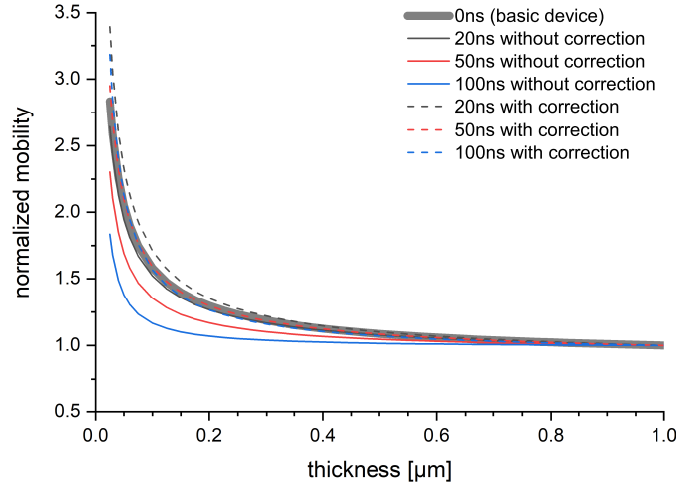


Figure 6.25: The normalized mobility in depends of different voltage rise times (solid lines) and corrected data (dashed lines). The thick, gray line is from the basic device. This basic signal is identical to the signal with 20 ns rise time.

$$f_{rise} = \frac{\mu_r}{\mu_0} = \frac{0.786 \frac{d^2}{t_{trans} V_S}}{0.786 \frac{d^2}{(t_{trans} - t_{corr}) V_S}} = 1 - \frac{t_{corr}}{t_{trans}} \quad (6.9)$$

For the correction in figure 6.25, $t_{corr} = t_{rise}$ is assumed. The corrected curves are the dashed lines. For $t_{trans} > 2 \cdot t_{corr}$, the corrected values are in good agreement with the data of the perfect voltage pulse. Otherwise, this correction is not sufficient.

As this correction depends only on the rise time and the transit time, it is used for the measured transient SCLC data in this thesis (Chap. 6.6.3).

For the second factor (the RC time constant) influencing the voltage rise time at the device under test, $t_{rise} = 20$ ns and a parasitic parallel capacitance of $13.33 \frac{\text{pF}}{\text{mm}^2}$ to the device is used. This parasitic capacitance is the estimated parasitic capacitance in the measurement circuit introduced in chapter 6.3 normalized to the device area of the real samples (Chap. 4) investigated in this thesis. The use of $t_{rise} > 0$ is important here as the non-ideal step function interacts with the RC time constant. Thus, in case of a serial resistance, t_{rise} can not be neglected as discussed in the following.

First, the RC time constant is estimated for different semiconductor thicknesses. The total capacitance important for the RC time constant is the sum of sample capacitance

and parasitic capacitance. The area dependent sample capacitance can be calculated with equation 6.8 for different thicknesses d with the permittivity $\epsilon_r = 3$. E. g., in case of $d = 100$ nm, $\frac{C_{samp}}{A} = 26.6 \frac{\text{nF}}{\text{cm}^2}$ results. Therefore, the total areal capacitance including the parasitic one is $28 \frac{\text{nF}}{\text{cm}^2}$. With the serial resistances from chapter 3.2, the resulting RC time constants t_{RC} are 2.1 ns ($7.5 \Omega\text{mm}^2$), 21 ns ($75 \Omega\text{mm}^2$), 525 ns ($1875 \Omega\text{mm}^2$) and 1.05 μs ($3750 \Omega\text{mm}^2$). The effect of the sample charging is neglectable for the lowest resistance compared to the voltage rise time. In case of $1875 \Omega\text{mm}^2$ and $3750 \Omega\text{mm}^2$, the rise time correction is dominated by t_{RC} , which actually becomes larger than t_{trans} .

For using the correction (Equ. 6.9) discussed for only rise time influences, t_{corr} has to be estimated. A simple assumption is $t_{corr} = t_{RC} + t_{rise}$ for considering the RC time constant and the voltage rise time if either value can not be neglected. For validation of this assumption, the following analytical estimation is done, where a serial resistance to a capacitance is assumed.

The derivation starts with the general relation between voltage $v_C(t)$ and charge $q_C(t)$ of the capacitance C : $q_C(t) = C \cdot v_C(t)$. The time derivation leads to equation 6.10 with $i_C(t)$ as the charging current, which is related to the serial resistance R_s by equation 6.11 with $v_0(t)$ as the total applied voltage.

$$i_C(t) = \frac{dq_C(t)}{dt} = C \cdot \frac{dv_C(t)}{dt} \quad (6.10)$$

$$i_C(t) = \frac{v_0(t) - v_C(t)}{R_s} \quad (6.11)$$

Equations 6.10 and 6.11 lead to equation 6.12.

$$R_s C \cdot \frac{dv_C(t)}{dt} = v_0(t) - v_C(t) \quad (6.12)$$

In case of $v_0(t) = a_{ramp} \cdot t$ is used for the ramping of the voltage step (Chap. 3.2), equation 6.12 can be solved by equation 6.13.

$$v_C(t) = a_{ramp} \cdot t - a_{ramp} R_s C + k \cdot e^{-\frac{t}{R_s C}} \text{ for } t \leq t_{rise} \quad (6.13)$$

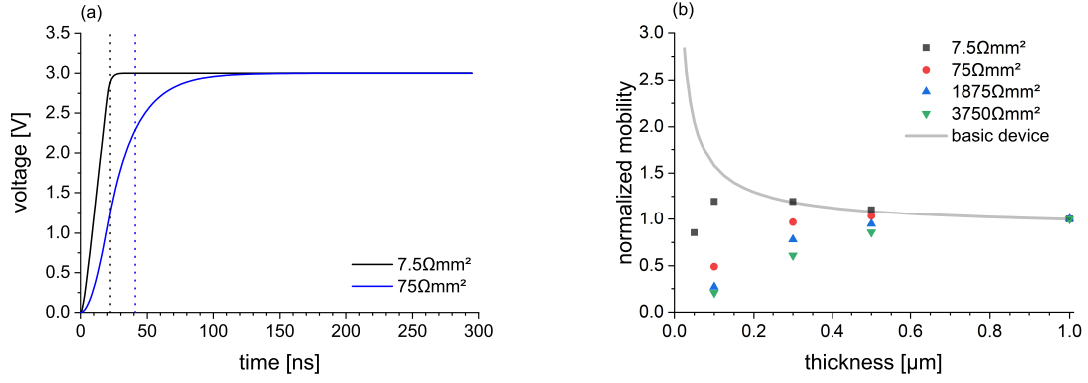


Figure 6.26: (a) Analytical voltage rise of a capacitance with two different serial resistances and a voltage rise time of 20 ns. The dashed lines mark the sum $t_{RC} + t_{rise}$. (b) Normalized mobility for different serial resistances. The thick, gray line is from the basic device.

The boundary condition $v_C(t = 0) = 0$ leads to $k = a_{ramp}R_sC$ and thus to equation 6.14.

$$v_C(t) = a_{ramp} \cdot t - a_{ramp}R_sC + a_{ramp}R_sC \cdot e^{-\frac{t}{R_sC}} \text{ for } t \leq t_{rise} \quad (6.14)$$

For $t > t_{rise}$, $v_0(t) = V_S$ is valid as the maximum of the voltage step is reached. Thus, equation 6.12 can be solved by equation 6.15.

$$v_C(t) = k \cdot e^{-\frac{t-t_{rise}}{R_sC}} + V_S \text{ for } t > t_{rise} \quad (6.15)$$

The equations 6.14 and 6.15 must have the same result at $t = t_{rise}$, which leads to $k = v_C(t = t_{rise}) - V_S$.

Figure 6.26a shows $v_C(t)$ for $7.5 \Omega\text{mm}^2$ and $75 \Omega\text{mm}^2$ ($d = 100 \text{ nm}$). The vertical, dashed lines are the assumed $t_{corr} = t_{rise} + t_{RC}$. For $7.5 \Omega\text{mm}^2$, the maximum voltage is reached only 3 ns later compared to t_{corr} , which corresponds to an error of 10%. However, because of the low influence of such short rise time, the correction factor f_{rise} (Equ. 6.9) has an error of only 2% ($t_{trans} = 300 \text{ ns}$). In case of $75 \Omega\text{mm}^2$, the effect of rise time increase is significantly larger, as t_{corr} is underestimated by factor 2. Consequently, the correction is not sufficient for this serial resistance which corresponds to 10Ω for the real devices in this thesis. As the total serial resistance in the developed circuit is 17Ω (Chap. 6.3), the effect of the rise time increase will be even larger.

Another influence of the serial resistance is the voltage drop over this resistance,

causing an overestimation of the voltage over the semiconductor and consequently a too low mobility (Equ. 2.27). This voltage drop depends on the relation between serial resistance R_s and device resistance R_{sample} . With estimated $\eta = 10^{17} \frac{1}{\text{cm}^3}$ and $\mu = 7 \cdot 10^{-5} \frac{\text{cm}^2}{\text{Vs}}$, R_{sample} can be calculated with equation 6.16. For $d = 100 \text{ nm}$, $R_{sample} \cdot A = 750 \Omega \text{mm}^2$ results. This is only valid for $F = 0.03 \frac{\text{kV}}{\mu\text{m}}$ and $f_{atj} = 10^{12} \text{ Hz}$, as those parameters strongly influence μ and η . Compared to $R_s = 7.5 \Omega \text{mm}^2$, R_{sample} is much larger and the voltage drop over the serial resistance is neglectable with a maximum error of 1%. Both, the voltage drop and the voltage rise time would lead to an underestimated mobility of 3% for a 100 nm thick layer.

$$R_{sample} \cdot A = \frac{1}{q\eta\mu} \cdot d \quad (6.16)$$

Figure 6.26b shows the device voltage rise time corrected normalized mobility (with $t_{corr} = t_{rise} + t_{RC}$) for the different serial resistances. The discussed fit (Chap. 3.2) is not applicable, as R_{sample} changes strongly with $\mu(F, f_{atj})$ and $\eta(F)$, which changes the voltage drop over R_s . Consequently, the fit can not account for the influence of F and f_{atj} .

As the discussed correction is applied for the data points in figure 6.26b, it is obviously not sufficient for accounting for a serial resistance. For the 100 nm thick layer and $R_{sample} \cdot A = 7.5 \Omega \text{mm}^2$, the mobility is 15% lower compared to the basic device. As discussed before, the influence of serial resistance and RC time on the mobility should be neglectable for this device even without correction. However, this is not possible with a 15% deviation.

This is caused by another effect, which is explained in the following. For ideal transient SCLC, infinite charge carrier injection is assumed. However, this assumption is not true in case of a serial resistance.

Considering the first injected charge carrier package into the semiconductor, the sample capacitance increases, as the distance between this charge carrier package and the ejection electrode decreases. Assuming a very high RC time constant, there is a negligible change in the total charge Q within the semiconductor. Consequently, the relation $Q = C \cdot V$ leads to a decrease of V if C is increased. This voltage decrease causes a lower electrical field strength during the charge carrier transit in contrast to the increase which is present in the ideal theory (Chap. 2.3.2). This leads to a reduced transit time compared to an ideal measurement and consequently an underestimation of the mobility.

This effect generally takes place if there is a large enough time delay caused by t_{RC} for the injection of additional charge into the semiconductor. The effect is stronger for thin layers, as C and t_{RC} of the sample is larger and the transit time is shorter. Additionally, the mobility reduction caused by slow charge injection is stronger for higher serial resistance as the RC time increases. As this is also true for the voltage rise time and voltage drop, there are three effects which lead to a decreased mobility in case of a high serial resistance.

The lowest assumed serial resistance of $7.5\Omega\text{mm}^2$, which correlates to 1Ω for the samples investigated in this thesis, has already a considerable effect on the determined mobility. The mobility decrease is larger than any effect caused by the other non-ideal influences discussed before. Consequently, the serial resistance generally dominates the non-ideal effects on the transient SCLC signal, causing a too low mobility. This confirms the need for a low serial resistance for transient SCLC measurements. Nonetheless, comparing devices with similar semiconductor thickness and applied electrical field strength is still sensible for analyzing the influence of trap states on the mobility as it is the objective in this thesis. A reduction of the mobility caused by introduced trap states will still be visible despite the serial resistance influences.

6.6 Analysis of universal trap levels

The objective of this thesis is the analysis of the proposed universal trap states as described in chapter 2.1.3. Nicolai et al. [111] and Zuo et al. [183] used steady state SCLC measurements to determine mobility and simulated the devices to calculate universal trap levels from these curves. As described in chapter 6.5, the steady state SCLC is difficult to interpret for thin devices. Additionally, a direct measurement of the trap distribution is missing. Consequently, if there are several different trap levels in the material, a differentiation is not possible. This makes the interpretation of Nicolai et al. unclear, as they think that these universal trap states are responsible for the generally lower electron mobility compared to holes. Furthermore, only pristine samples were analyzed. Thus, water or oxygen is not proved to be the origin of these universal trap states.

Therefore, the questions for the following analysis are: Are there universal trap levels, either in reference to HOMO/ LUMO or vacuum level? Do these trap states depend on oxygen or water? Can these trap states be responsible for the difference in electron and hole mobility?

To answer these questions, the three polymers P3HT, PCPDTBT and MDMO-PPV are investigated in pristine and degraded state, using oxygen, water and UV light as described in chapter 4.4.3. The trap distributions of these materials, whether pristine or aged, are directly measured with the MIS-TSC method developed in chapter 6.1. The results are correlated to the charge carrier mobility determined by transient SCLC with the developed measurement circuit (Chap. 6.3). Here, only the amplification $184 \frac{\text{V}}{\text{A}}$ with $R_m = 10 \Omega$ is suitable for the polymer devices.

6.6.1 Difference of electron and hole mobility in pristine semiconductors

Nicolai et al. [112] suggested that the electron and hole mobilities are about equal, if the specific electron trap states can be avoided. In figure 6.27, transient mobility values for electrons (empty symbols) and holes (full symbols) at comparable film thicknesses are displayed for all pristine materials determined with the transient SCLC method described in chapter 6.4.2.

A good agreement between electron and hole mobility is visible for PCPDTBT. For MDMO-PPV and P3HT, the mobilities of electrons and holes are about equal within the error bars. The differences can be caused by thickness dependent effects, as the semiconductor thicknesses of electron and hole only devices are not equal. Thus, a high similarity between electron and hole mobility can be assumed for all materials.

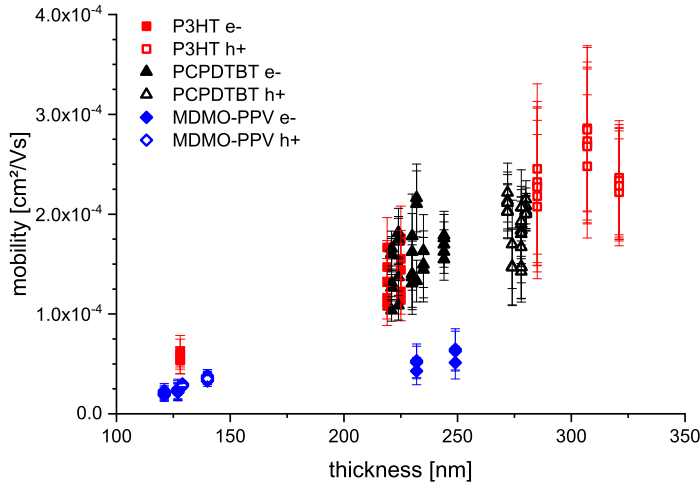


Figure 6.27: Mobilities from the transient SCLC measurement for all pristine materials: Comparison of electron and hole mobility.

As these transient mobility values have a small dependency on trap states [95, 103, 120], especially on slowly filled trap states, the assumption of equal mobility for electrons and holes for trap free materials is confirmed.

Consequently, the difference of hole and electron mobility depends on the method applied for mobility determination. E. g., the steady state SCLC method will show significantly different values compared to the transient SCLC method, as slowly filled trap states are occupied in the steady state, which is not the case for the transient measurement.

6.6.2 MIS-TSC Measurements

In this chapter, the trap distributions of the pristine and aged polymers are measured. The measurement procedure is described in chapter 6.1.4. The first question is, if the aging treatments actually introduce additional trap states. For this purpose, the enveloping MIS-TSC signals are suitable.

Figure 6.28 shows an enveloping MIS-TSC example for pristine and aged P3HT. The signals of oxygen and water treatments are generally larger than the pristine one. This is especially true for the electron trap peak between 50 K and 100 K and for the hole signals above 100 K. The increase of the signal by only UV light can be caused by residual oxygen or water in the pristine material or other chemical changes in the molecular structure.

Generally, this result verifies the degradation effect discussed in the literature [68, 101, 140, 161], which is photo oxidation caused by UV light in combination with oxygen or water. The results for MDMO-PPV and PCPDTBT are similar as shown in the appendix (App. 8.6). This is expected, as photo oxidation happens in all organic semiconductors.

As new oxygen and water dependent trap states are introduced into the materials, the trap distribution determined with the fractional MIS-TSC method can show the energetic depth of these trap states.

The hole trap distributions of pristine and aged P3HT, PCPDTBT and MDMO-PPV, determined from fractional MIS-TSC measurements, are given in figure 6.29. For all graphs, the bottom axis sets the determined activation energy (equal to trap levels (Chap. 2.1.3)) in relation to the HOMO level, while the top axis shows the relation to the vacuum level. The deviation of the top axis results from the uncertainty of the HOMO level (App. 8.2). The original fractional measurements are given in the appendix 8.6. The water traps (dark yellow dotted line), relative to the HOMO level as listed in table 2.1, are marked in all figures. A range of a possible universal relative trap level (to the HOMO level) determined in this thesis is marked with a green area.

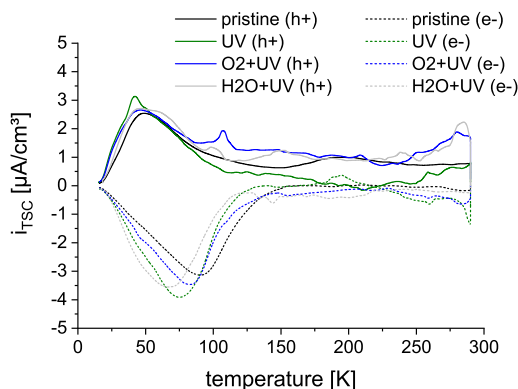


Figure 6.28: Enveloping MIS-TSC measurement of pristine and aged P3HT. The shift of the electron peaks of aged P3HT may be caused by retrapping, as additional shallow trap levels are introduced by the aging.

Furthermore, black arrows at the top axis mark possible universal absolute trap levels, in respect to the vacuum level, which are determined in this thesis.

At first, hole trap states caused by oxygen and water treatments are analyzed. For all materials, the water treatment has the largest effect on the hole trap distribution, although the oxygen treatment has a very similar effect. In the range 0.15 eV to 0.5 eV in relation to the HOMO level, there is always an increase of the trap density caused by the water treatment. This range correlates to the water trap levels suggested by Zuo et al. [183]. As the result with the oxygen treatment is similar, but perhaps less effective, it is not possible to determine if the origin of this universal trap level is the incorporation of water or the existence of oxygen groups.

Considering a universal absolute trap level, trap peaks at $-4.8 \text{ eV} \pm 0.1 \text{ eV}$ and $-4.4 \text{ eV} \pm 0.1 \text{ eV}$ are visible for holes, where the uncertainty of 0.1 eV correlates with the HOMO uncertainty. For P3HT and -4.8 eV, no increase with any treatment is visible. Possibly, another type of trap dominates here. The -4.4 eV peak is not visible for PCPDTBT, as the HOMO of this material is probably too far away from this trap to be measurable with the used MIS-TSC method. To measure deeper trap levels, an increase of the temperature above 300 K would be necessary. However, there is another pronounced peak at -5.3 eV visible, which is not relevant for the other materials and no conclusion is possible about the universal nature of this trap state.

Considering the UV treatment, the trap distribution is in most cases similar to the pristine material. A light increase of the trap amount might be caused by residual oxygen or water in the pristine materials.

For all polymers, there are individual trap levels which are not explained with a

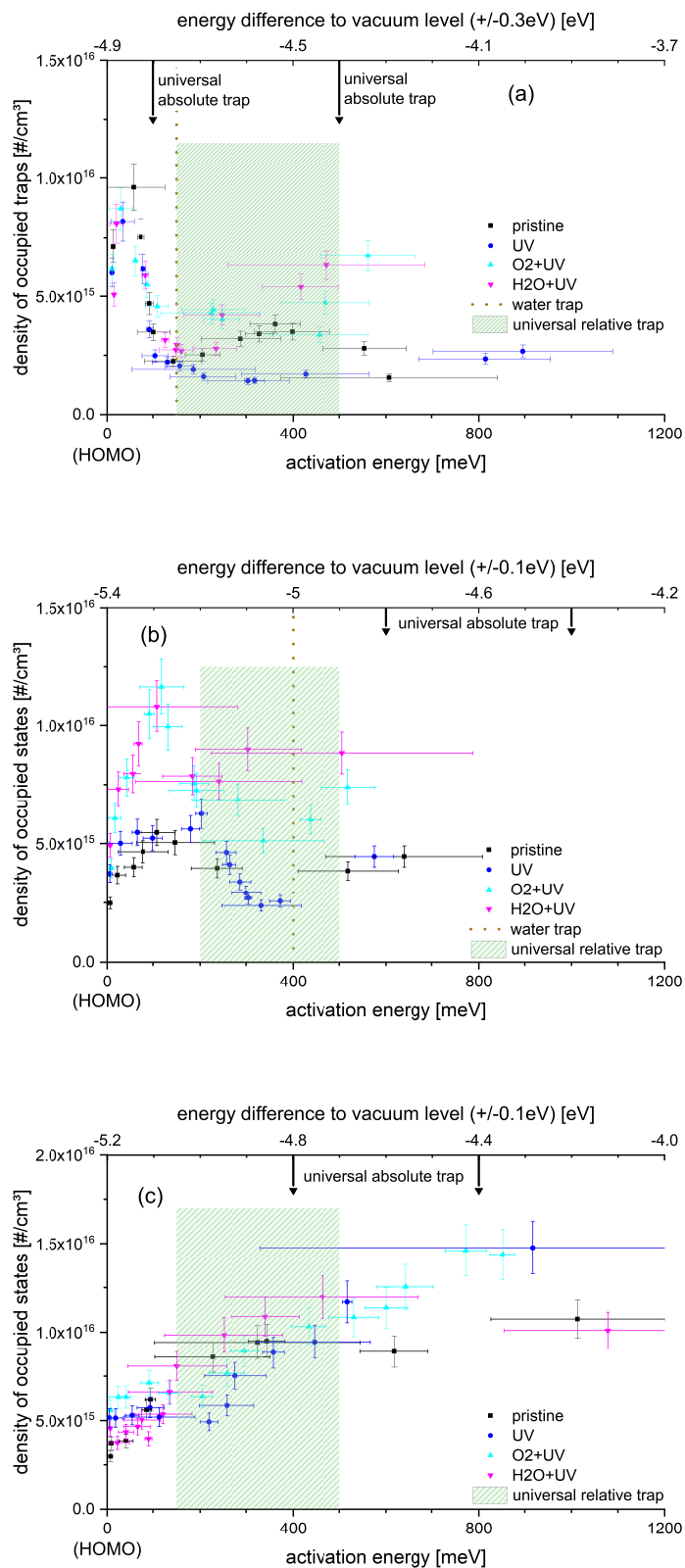


Figure 6.29:
Distribution of hole trap levels of pristine and aged polymers:
(a) P3HT,
(b) PCPDTBT,
(c) MDMO-PPV.

Vertical dotted lines show the universal trap levels determined by Zuo et al. [183] as given in table 2.1. The green area is the range of a universal relative trap level determined in this thesis. The black arrows at the top are locations for a universal absolute trap level determined in this thesis. The left side of the top and bottom axis mark the HOMO level (Fig. 4.4). The uncertainty of the HOMO level is given in braces at the top axis.

universal trap level. E. g. for P3HT, a large peak is at 0.1 eV below the HOMO level, which is present in the pristine material and not increased by any treatment (Fig. 6.29a). Thus, the largest amount of trap states are not caused by water or oxygen.

For MDMO-PPV, in contrast to the other two materials, the maximum trap density is not in the shallow range (Fig. 6.29c). There is little increase of the hole trap amount for shallow trap levels up to 0.1 eV below the HOMO level. Consequently, these trap states seem not dependent on oxygen or water. The oxygen treatment causes deeper trap levels in the range of 0.5 eV to 0.8 eV, which might be similar to the UV treated sample. However, the UV measurement lacks on precision which is visible at the large error bars at the single data point for deep trap levels. Thus, there are probably different types of trap states introduced by water and oxygen treatment in this case.

Figure 6.30 illustrates the trap distribution results for electrons with the same layout as in figure 6.29 with the left axis as the LUMO level. Additionally, the oxygen trap levels are marked with red dotted lines (Tab. 2.1) relative to the LUMO level. As for holes, there is always an increase of the trap density caused by the water and a smaller effect by the oxygen treatment. A universal relative trap level (green area) is found for electrons in the region 0 eV to 0.25 eV below the LUMO level, although the increase in trap density is small for MDMO-PPV. This range is lower than the water trap level suggested by Zuo et al. [183].

In relation to the vacuum level, there are peaks in the electron trap distributions at $-3.6\text{ eV} \pm 0.1\text{ eV}$ for all materials, eventually caused by aging treatments. This universal absolute trap level correlates to oxygen traps and therefore to the universal trap proposed by Nicolai et al. [112] if the LUMO uncertainties are considered.

Again, there are unique observations for each material, which can not be accounted to the universal trap levels. For P3HT (Fig. 6.30a), the trap level at -3.6 eV in respect to the vacuum level is possibly too deep to be measured accurately, thus showing only a shallow peak. For the pristine sample, there are no measurable deep trap levels as the TSC signal is in the noise range.

In case of PCPDTBT, the trap density is strongly increased for shallow electron trap levels of 0 eV to 0.05 eV (Fig. 6.30b) independent on the type of aging treatment. Thus, these trap states are probably caused by the UV light. For the range 0.05 eV to 0.25 eV, the amount of trap states is increased only by the water treatment, which correlates with the proposed oxygen trap.

Again, as for holes, the maximum trap density of MDMO-PPV is not in the shallow range for electrons (Fig. 6.30c). Generally, the effects of the aging treatments are

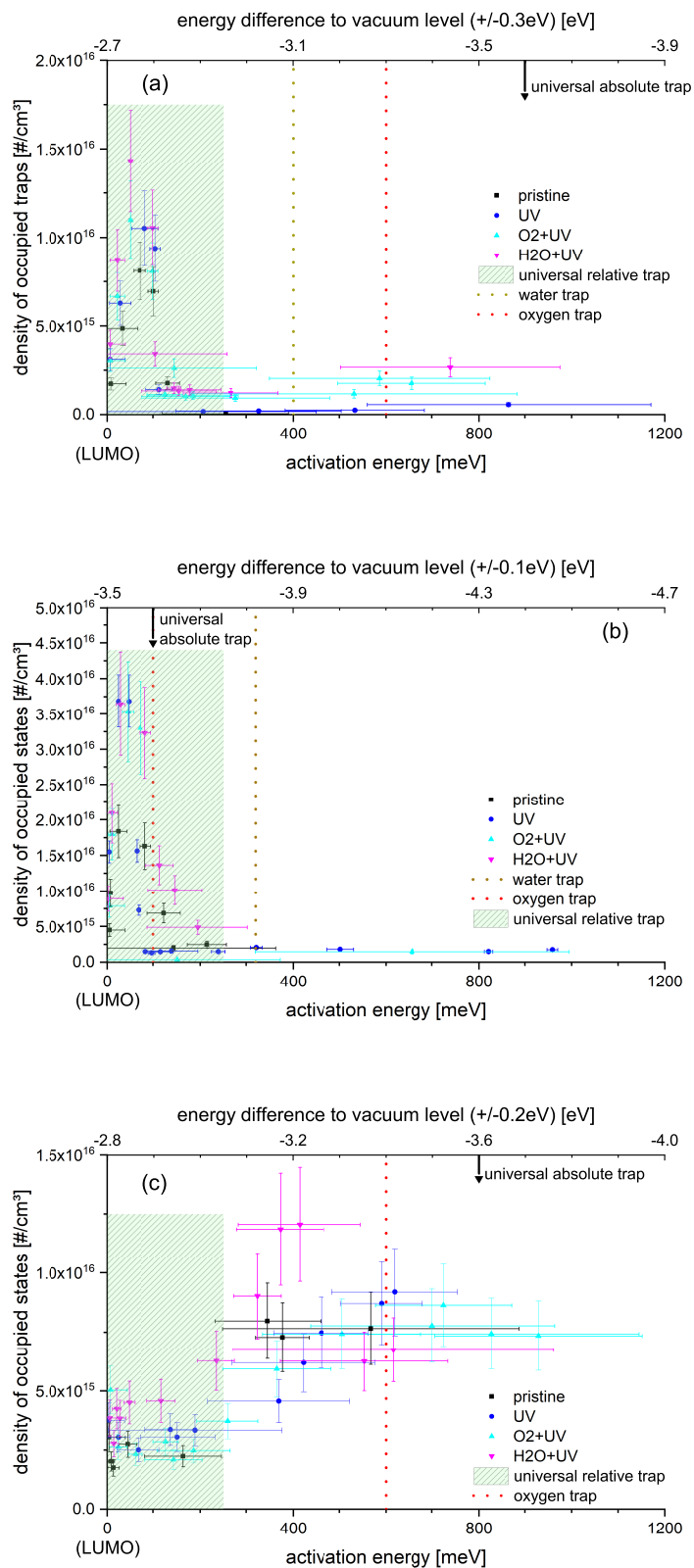


Figure 6.30: Distribution of electron trap levels of pristine and aged polymers: (a) P3HT, (b) PCPDTBT, (c) MDMO-PPV.

Vertical dotted lines show the universal trap levels determined by Nicolai et al. [111] and Zuo et al. [183] as given in table 2.1. The green area is the range of a universal relative trap level determined in this thesis. The black arrows at the top are the locations for a universal absolute trap level determined in this thesis. The left side of the top and bottom axis mark the LUMO level (Fig. 4.4). The uncertainty of the LUMO level is given in braces at the top axis.

smaller compared to the other materials. The major difference is the much broader trap distribution, as it is already visible for holes.

In the following, general conclusions for all materials are discussed. Comparing the electron and hole trap distributions of the pristine samples, shallow trap states are similar in both cases for all materials. This is in line with the equal mobility for electrons and holes discussed in chapter 6.6.1. A similar shallow and thus fast filled trap distribution has the same influence on both, the electron and hole mobility.

Considering the trap levels caused by oxygen and water treatments for both electrons and holes, there are potentially universal trap states. Additionally, there are similar trap levels caused by UV light, but there is always a lower increase, which can be caused by residual oxygen or water [112, 183]. The uncertainties of the universal trap levels are caused by the uncertainty of the HOMO and LUMO levels and error bars of the data points. However, as a wide distribution of different trap levels is visible in most cases, these universal trap states are not necessarily the dominant trap level influencing the charge carrier transport. Therefore and because of the wide trap distributions, the reduction of the distribution to a single level as suggested by Nicolai et al. [112] and Zuo et al. [183] is inaccurate and not a suitable model for the investigated materials.

Furthermore, apart from PCPDTBT, the trap distributions for holes and electrons are similar and a large difference of charge carrier mobility solely depending on differences caused by universal trap states seems unlikely. This is especially the case, as oxygen causes electron and hole trap states simultaneously. However, an influence of trap states on the mobility solely determined from the trap depth is inaccurate, as the dynamics of trap occupation has a major influence. Thus, the influence of the trap states introduced by the aging on the mobility has to be determined by separate mobility measurements.

6.6.3 Analysis of SCLC measurements

In chapter 6.6.2, the trap distributions caused by oxygen, water and UV light exposure are discussed, but the influence of these trap states on the charge carrier transport is still unclear. Therefore, the mobility of P3HT, PCPDTBT and MDMO-PPV (either pristine or aged) was measured with the transient SCLC method (Chap. 2.3) with the circuit developed in chapter 6.3 and the measurement procedure in chapter 6.4.2. The devices are described in chapter 4.2.

Figure 6.31 shows the determined transient mobilities for holes and electrons of P3HT for different film thicknesses and average electrical field strength [1, 21, 62, 182]. The error bars are the result of the uncertainties of film thickness and oscillation correction

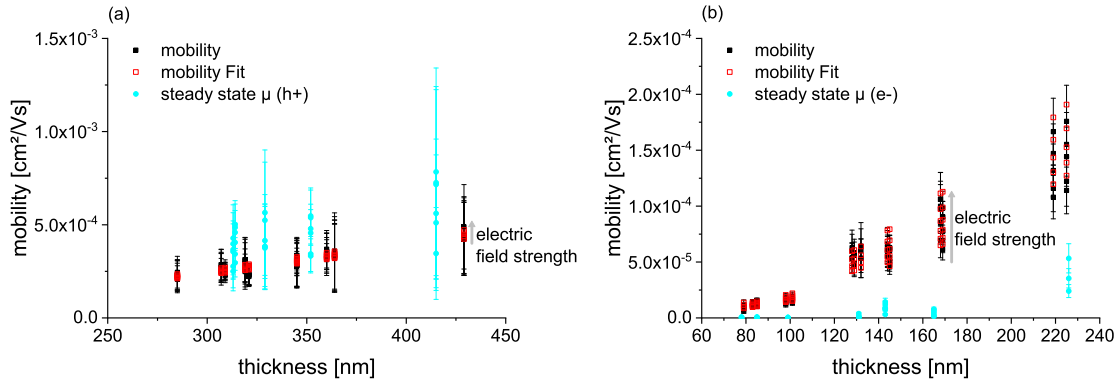


Figure 6.31: Transient and steady state mobility of (a) holes and (b) electrons for pristine P3HT. The vertical distribution of the transient SCLC mobility accounts to different electrical field strength.

(Chap. 6.4.2). As discussed in chapter 6.5.5, the determined mobility depends on the thickness and electrical field strength. Because of the large distribution, an analysis of these dependencies is necessary, so that different samples become comparable. The analysis for this purpose is explained in the following at P3HT as an example. For PCPDTBT and MDMP-PPV, the same procedure is done and the same figures as shown here for P3HT are given in the appendix (App. 8.7.2).

At first, the determined transient SCLC mobility is compared to the estimated mobility from steady state SCLC, which is plotted as reference values in figure 6.31. The hole only device has an almost ideal behavior, thus there is a good correlation between steady state and transient mobility. However, the steady state mobility suffers from large deviations caused by thickness uncertainty and standard deviation from measuring several devices. Because of this too large deviation, the comparison of pristine and aged samples is not possible with the steady state mobility. As expected in chapter 6.5.1, the steady state measurement is strongly influenced by non-ideal parameters, which causes the large difference between the steady state and transient mobility for the electron only devices. In agreement with the assumption of built-in and injection barrier influences, the steady state mobility is always lower or equal to the transient measurements.

Consequently, in the following, only the transient mobility is discussed. It is obvious, that there is a strong dependence of the mobility on the film thickness. Additionally, a weaker dependence on the electrical field strength is present. As discussed in chapter 6.5.5, this is primarily caused by serial resistance influences. This results in unprecise correlation between mobility data resulting from different film thicknesses and electrical field strength. Consequently, there is no fixed mobility value of the pristine sample which

can be used as reference value for aged samples. To make this comparison possible, an interpolation and extrapolation of the pristine mobility is necessary, in dependence of film thickness and electrical field strength.

Equation 6.17 is found to be a suitable choice for this purpose. Here, d is the semiconductor thickness in nm and F is the average electrical field strength in $\frac{\text{kV}}{\mu\text{m}}$. The fit variables a_{SCLC} , b_{SCLC} and c_{SCLC} can be found for all materials in table 8.11 (App. 8.7.1). The calculated mobility with this fit is also given in figure 6.31. Due to spreading of the mobility values and changing dependency on F with different thicknesses, a deviation between fit values and original data is present.

$$\frac{\mu}{1 \frac{\text{cm}^2}{\text{Vs}}} = c_{SCLC} \cdot \left(\frac{d}{1 \text{ nm}} \right)^{a_{SCLC}} \cdot \left(\frac{F}{1 \frac{\text{kV}}{\mu\text{m}}} \right)^{b_{SCLC}} \quad (6.17)$$

This deviation between fit and original data is visible in figure 6.32 for P3HT, where the mobility data of the pristine and aged samples is normalized to the fit. In case of the hole mobility, the dependence on the electrical field strength changes by aging. This causes a larger spreading of the normalized values compared to the pristine sample.

For comparison of the devices, the average of all normalized mobility values is used and the standard deviation of this average calculated. This deviation is added to the average deviation of the original mobility data depending on e.g. thickness uncertainty (Fig. 6.31). Both contribute about equally to the total error bars, which is given in figure 6.35a and 6.36a for the three polymers. The results visible in these figures are discussed in chapter 6.6.4. The resulting error bars are large but the trend of e.g. reduced mobility of aged samples is still evident considering figure 6.32, as almost all normalized mobility values of aged samples are located below the pristine reference. However, the difference between different aging treatments is less evident.

The found changes in mobility values can now be correlated to the energetic trap distribution determined with the MIS-TSC method in chapter 6.6.2. However, the type of the trap states causing mobility reduction is not clear, whether it is a deep or shallow trap (Chap. 2.1.3). Further information about the trap depth can be derived from the ratio between transient peak and steady state current. The ideal value for this ratio is 1.21 (Chap. 2.3.2). Usually, due to diffusion and the charging RC time constant, the ratio will be lower than the ideal value of 1.21. Shallow trap states will cause a further reduction for this ratio, as the trap states are fast filled and charge carriers removed from

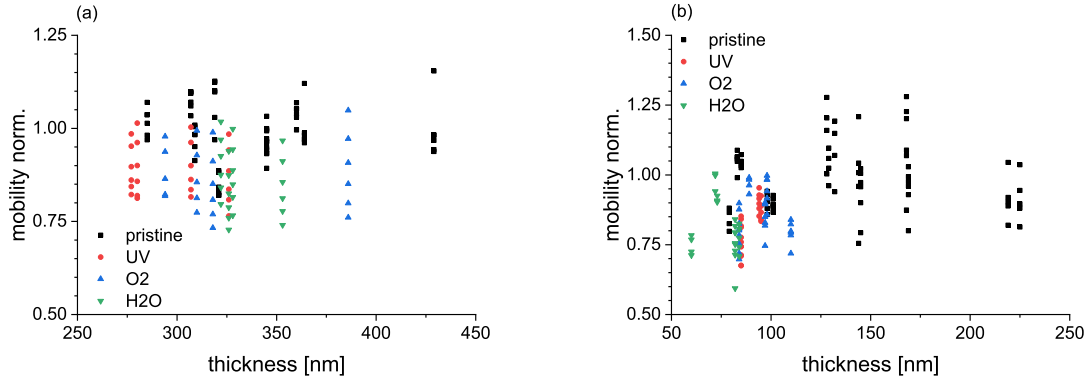


Figure 6.32: Normalized transient mobility of (a) holes and (b) electrons for pristine and aged P3HT.

the first injected charge carrier package. Deep trap states are usually filled slow, reducing the amount of charge contributing to the current, which causes a slow attenuation of the current. This will cause an increase of the ratio.

For this ratio, as a characteristic value, the ratio between the transient peak current and the current at $5\ \mu\text{s}$ is used. Because of $t_{trans} < 1\ \mu\text{s}$, a steady state mode can be assumed at $5\ \mu\text{s}$ as it is typically reached at $t = 2t_{trans}$ [67]. In case of further current decrease over time, the tendency of the ratio would not change.

Although the dependence of this ratio on the film thickness and average electrical field strength is lower compared to the mobility (Fig. 6.31), the same procedure for normalization is done (fig. 6.33 and 6.34 for P3HT) with the coefficients given in table 8.12 (App.8.7.1). The resulting normalized values are multiplied with the average ratio of the pristine data to create absolute values for comparison to the ideal value of 1.21.

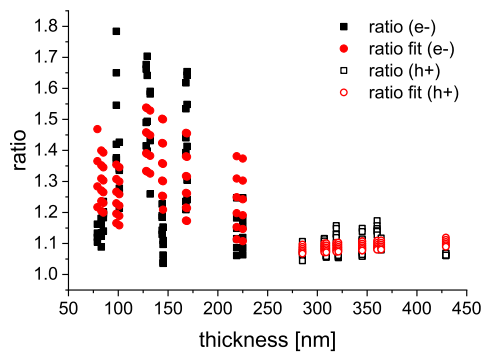


Figure 6.33: Ratio of the transient peak and steady state signals for P3HT devices.

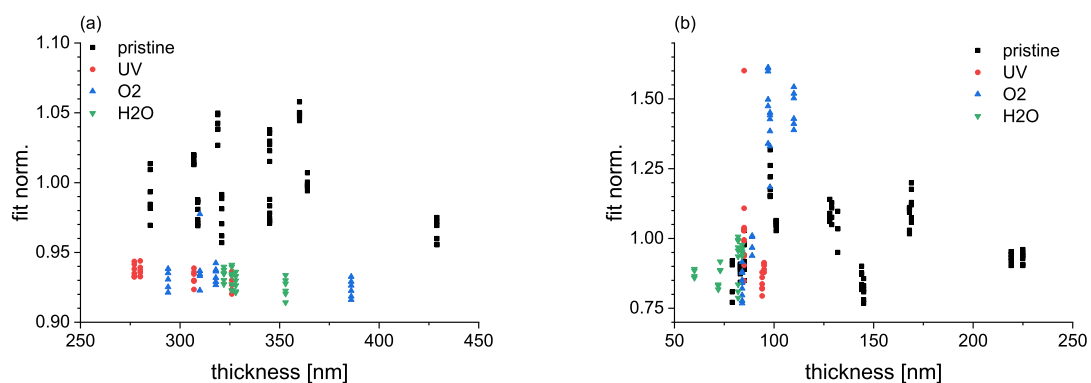


Figure 6.34: Normalized current ratio of (a) holes and (b) electrons for pristine and aged P3HT samples.

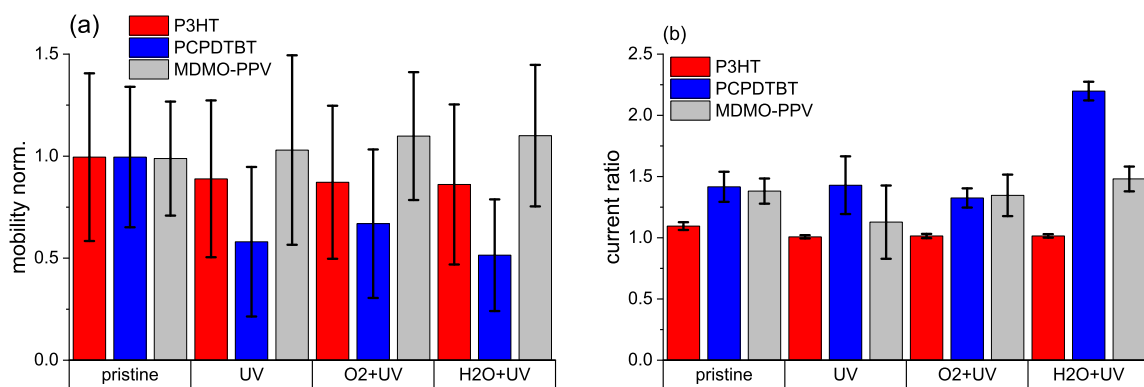


Figure 6.35: (a) Normalized hole mobility and (b) current ratio for all polymers.

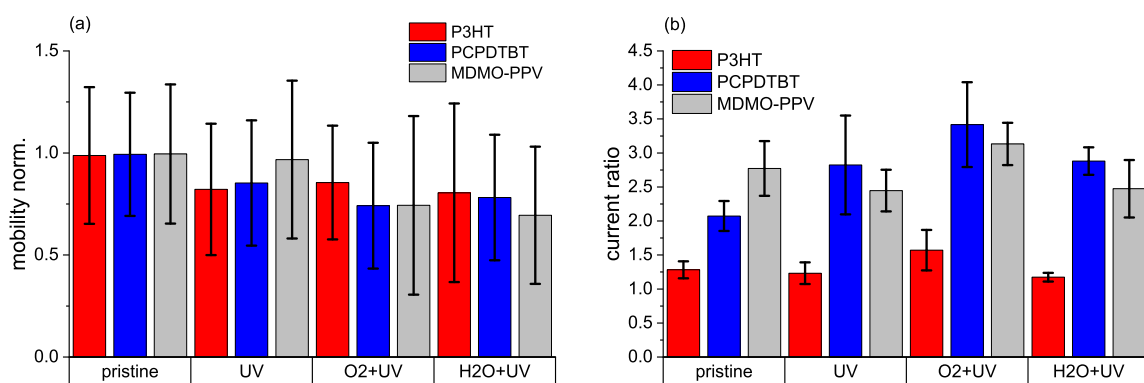


Figure 6.36: (a) Normalized electron mobility and (b) current ratio for all polymers.

6.6.4 Correlation of trap distribution and mobility

The evaluation of the transient SCLC measurement is explained in chapter 6.6.3, which results in the graphs of figure 6.35 and 6.36. Here, the mobility and current ratio are shown, which are normalized to the pristine samples for all aging treatments. Most variations are within the relatively large error bars. However, some tendencies, especially if there is the same tendency for all treatments, can be discussed.

These small changes for P3HT indicate, that the contact materials for SCLC devices are not sensitive to the aging treatments and that the stronger changes visible for PCPDTBT and MDMO-PPV are caused by degradation processes in these materials. This is in line with the literature where the used PEDOT:PSS [34] as well as the small molecules [27, 60, 142] are less sensitive to degradation.

In figure 6.35a, the hole mobility decreases for P3HT and PCPDTBT, while the effect is stronger for PCPDTBT. The decrease is similar for all treatments, also for the UV light treatment. This is either caused by residual oxygen or water reacting with UV light, or the degradation depends solely on UV light exposure. Considering the hole trap distribution in figure 6.29a, the dominating trap level for P3HT hole transport is shallow in the range 0 eV to 0.1 eV. These trap states show little change with any aging treatment. This explains the small hole mobility reduction. In case of PCPDTBT, there is a low intrinsic shallow (0 eV to 0.2 eV) trap density in the pristine state. It is reasonable, that there is a strong decrease of mobility caused by the additional trap states introduced by the aging treatments. For oxygen and water treatment, this is in line with the trap distribution in figure 6.29b, although the UV light treatment shows a lower effect.

In contrast to P3HT and PCPDTBT, the hole mobility of MDMD-PPV does slightly increase with the aging treatments. The amount of shallow trap levels changes only slightly by the treatments (fig. 6.29c). However, the slightly increased mobility can be a result of additional transport states, as the trap distribution directly at the HOMO level is increased by the aging processes.

Considering the current ratio for P3HT (Fig. 6.35b), the pristine value is almost ideal at 1.21, suggesting no slowly filled deep trap levels. The ratio decreases for all treatments similarly. This can be explained by an increased amount of fast filled trap states, which are typically shallow. However, considering the measured trap distribution in figure 6.29a, there are primarily deep trap levels in the range 0.2 eV to 0.6 eV caused by the aging processes. Thus, these deep trap levels seem to be filled fast and there is no slow trap filling.

In the case of PCPDTBT, the pristine current ratio is significantly above 1.21 which is well in line with existing deep trap states (0.4 eV to 0.8 eV) visible in figure 6.29b. Furthermore, the largest increase for the amount of deep trap levels is visible for water treatment. This is in agreement with the strongly increased ratio for the water treatment.

For MDMO-PPV, the current ratio is also almost constant. The pristine material has already a large amount of trap states (fig. 6.30c). Thus the slow filling of trap states is not considerably increased by the aging treatments. However, a slight increase of the ratio is visible for the water treatment, where the largest amount of deep trap levels is introduced as visible in figure 6.30c.

Considering the electron mobility in figure 6.36a, a similar effect for all materials is visible. The mobility is decreased similarly for all treatments while the effect is less pronounced for the UV light treatment. This correlates with the measured energetic trap distribution (Fig. 6.30), as for all materials shallow trap levels in the range 0 eV to 0.15 eV are introduced similarly for the aging treatments with the lowest effect caused by UV light.

The ratio of the P3HT measurements (Fig. 6.36b) is larger than ideal for the pristine material and all treatments, suggesting the existence of intrinsic, slowly filled deep trap states. Considering the energetic trap distribution in figure 6.30a, such an intrinsic trap level is not visible. In contrast to other treatments, the ratio increases only for oxygen treated samples. This is in line with the energetic trap distribution in figure 6.30a, where a considerable increase of deep trap states at 0.6 eV is visible for the oxygen treatment.

For PCPDTBT, there is a slight increase of deep trap states (0.4 eV to 1 eV) visible in figure 6.30b, as the deep trap levels of the pristine sample were not measurable because of a too low current signal. Thus, the increase of the current ratio is reasonable. However, the high ratio even for the pristine material, is not explainable. Consequently, either there are more trap states which were not measured by the MIS-TSC method or the filling mechanism is fundamentally different compared to e. g. P3HT, causing a slow filling of shallow trap levels.

Considering the current ratio of MDMO-PPV, there is no obvious trend. This is probably caused by the already existing large amount of trap states in the pristine sample (Fig. 6.30c). The small increase of the amount of trap states caused by aging treatments has therefore little effect on the current ratio.

Considering this transient SCLC analysis, the question whether a universal trap level can explain charge carrier transport parameters can now be answered. Different effects of additional oxygen and water dependent trap states on the electron and hole mobil-

ity are visible. E. g. for PCPDTBT, there is a similar mobility reduction visible for both charge carrier types. In contrast, for MDMO-PPV, the hole mobility is increased and the electron mobility is decreased. Thus, depending on the material, the electron and hole mobility in the presence of trap states can be equal or different. Although the electron mobility decrease is similar for all materials and assignable to the shallow universal relative trap level as discussed in chapter 6.6.2, the effect on the current ratio is significantly different for all materials. In contrast, the effect of the aging treatments is largely different for the hole mobility depending on the material, but the changes for the current ratio in case of hole only SCLC are small.

Generally, the different dependencies of electron and hole mobility on oxygen and water traps is caused by the different dynamics of trap filling depending on the material and charge carrier type. Although oxygen and water cause hole and electron trap states at the same time, this difference can be caused by different trap filling mechanism. Probably, this mechanism is not only depending on the energetic trap depth in relation to the HOMO and LUMO levels but also on the position within the molecules.

Because of the different effects for all polymers, the influence of the proposed universal absolute and relative trap levels is largely different depending on the material. Furthermore, intrinsic trap states which have other origins may have a larger influence on the charge carrier transport than the universal trap states. E. g., Sulfur oxidation causes unique trap states within P3HT as discussed by Manceau et. al [101]. Thus, describing an organic semiconductor device with a single mobility value or a single trap level can be wrong. E. g. for fast electron measurements, the shallow universal trap level can describe the mobility correctly. However, if a longer measurement time is chosen, it depends strongly on the amount of filled trap states and if the material is truly in the steady state mode.

7 Summary

The objective of this thesis is the investigation of universal oxygen and water dependent trap states within organic semiconductors suggested in recent literature [111, 114, 183]. Furthermore, the question if these universal trap states are responsible for lower electron mobility compared to holes is considered in this thesis. The challenges are the unipolar determination of the trap distribution as well as the charge carrier mobility. To investigate the origin of trap states, water and oxygen dependent trap states have to be introduced into the material under test.

For the purpose of determining the unipolar energetic distribution of trap states, the classical thermally stimulated current (TSC) method is modified and a metal insulator semiconductor (MIS) structure is measured instead of a diode. With *Poly(3-hexylthiophene-2,5-diyl)* (P3HT) as a benchmark material, the working principle of this method is demonstrated. By using the MIS structure, the trap state distributions of both, electrons and holes, can be determined at a single test sample. Beyond this, the MIS-TSC approach reduces recombination effects, which are one of the major disadvantages of the classical TSC method. Further, due to the high serial resistance of MIS structures, a noise level in the sub pA range can be obtained, resulting in a measurable TSC below 1 pA.

For determining the mobility, the space charge limited current (SCLC) is measured in steady state and transient mode. As non-ideal parameters have a significant influence on the mobility determination at thin film devices, the accuracy of both SCLC methods is analyzed with a device simulation. This simulation shows that the transient method is less sensitive to non-ideal device parameters and has a higher accuracy. However, the serial resistance, hence the RC time for device charging, has a major influence on the determined transient mobility. Even for a $10\ \Omega$ serial resistance (device area of $7.5\ \text{mm}^2$ and thickness of 50 nm), a mobility reduction of 20 % occurs in relation to a $1\ \mu\text{m}$ thick device.

Still, the transient method shows a lower dependence on film thickness by a factor up to 3 in relation to the steady state method. Because of the high RC time influence,

the minimization of the serial resistance for sample charging is crucial. Furthermore, a wide measurable current range for the analysis of devices with different conductivity is necessary. To fulfill these requirements, a circuit is developed, which allows for a low RC time constant for sample charging as well as for a wide current (0.1 μ A to 0.5 A) and voltage range (3.5 V to 50 V). This results in a high flexibility in terms of minimum measurable film thickness, which is necessary for the measurement of organic semiconductors in this thesis. However, the measurable minimum mobility depends strongly on the thickness of the semiconductor. Considering e. g. a minimum transit time of 300 ns and a thickness of 100 nm, the detectable minimum mobility is $1 \cdot 10^{-4} \frac{\text{cm}^2}{\text{Vs}}$. For a thick film of 1 μ m it is $1 \frac{\text{cm}^2}{\text{Vs}}$.

With these measurement methods, the trap distribution and the mobility of the three organic polymers P3HT, *Poly[2,6-(4,4-bis-(2-ethylhexyl)-4H-cyclopenta[2,1-b;3,4-b']dithiophene)-alt-4,7(2,1,3-benzothiadiazole)]* (PCPDTBT) and *Poly[2-methoxy-5-(3',7'-dimethyloctyloxy)-1,4-phenylenevinylene]* (MDMO-PPV) are measured in this thesis. Additionally, the influence of oxygen and water exposure on the trap distribution and mobility is considered.

Zuo et al. [183] discussed a universal water trap level 0.3 eV above HOMO and below LUMO level. Here, for the water treatment, only a minor general increase of the amount of trap states in respect to the HOMO or LUMO level is visible. This suggests, that this universal relative trap level, if present, is not relevant compared to other effects. In contrast, several potentially universal trap levels are found in relation to the vacuum level. These are: -4.8 eV and -4.4 eV for holes as well as -5.3 eV, -3.6 eV and -2.8 eV for electrons. For further proof, additional materials have to be investigated.

Nicolai et al. [111] suggested only the electron trap level at -3.6 eV. Although this trap level is one potential universal trap level measured in this thesis, several more trap levels are found. The influence of these trap states on the charge carrier transport depends on the HOMO and LUMO levels, thus the mobility reduction caused by oxygen defects can be different for electrons and holes.

The transient SCLC measurements show that the mobility does not completely correlate with the additionally introduced trap states. Thus, probably not only the trap depth is important for the charge carrier transport mechanism, but also the trap filling mechanism, which seems to be different for the materials. In case of P3HT, a fast trap filling is present, while it is slower for PCPDTBT and MDMO-PPV. This might be caused by the position of the functional oxygen groups within each polymer.

However, as the mobility from the transient SCLC has a low dependency on trap

states, the suggested similarity of electron and hole mobility is visible with this method. This result is in line with the assumption by Nicolai et al., that the electron and hole mobility should be similar to each other in case of a trap free material. Thus, the results confirm that trap states generally are the cause for mobility reduction, but also show a high dependency on the dynamics of the trap filling process.

In conclusion, possibly universal trap levels are found which depend on oxygen and water. Apart from these trap levels, each material has a unique trap distribution and different dependencies of the mobility on the universal trap states. Consequently, the reduction of the complex trap distribution to a single trap state is no accurate model for the description of the influence of trap states on the charge carrier transport in organic semiconductors.

8 Appendix

8.1 Theory: Equations for electrons

As only the equations for holes are given in the chapter 2 and 3, the corresponding equations for electrons are given in the following. The variable names are listed in table 8.1.

The charge carrier continuity for electrons (Equ. 8.1) is similar as for holes (Equ. 3.3), as it is the case for the equation hole (Equ. 3.4) and electron current density (Equ. 8.2).

$$\frac{\delta n}{\delta t} = \frac{1}{q} \cdot \text{div} \vec{J}_n + G_{gen,n} - R_{rec,n} \quad (8.1)$$

Table 8.1: Variables used in this chapter.

variable	decription
n	density of electrons contributing to the charge transport
\vec{J}_n	electron current density
$G_{gen,n}$	electron generation rate
$R_{rec,n}$	electron recombination rate
μ_n	electron mobility
D_n	diffusion coefficient for electrons
$E_{tr,n}$	effective transport energy for electrons
$g_L()$	Gauss profile of the LUMO
γ_n	hopping distance for electrons
$f_{atj,n}$	attempt to jump frequency for electrons

$$\vec{J}_n = qn\mu_n\vec{F} + qD_n\nabla n \quad (8.2)$$

Corresponding with equation 2.3, the transport energy for electrons can be determined with equation 8.3.

$$\int_{-\infty}^{E_{tr,n}} \frac{g_L(E') \cdot (E_{tr,n} - E')^3}{1 + e^{-\frac{E' - E_F}{k_B T}}} dE' = \frac{6}{\pi} \cdot (\gamma_n \cdot k_B T)^3 \quad (8.3)$$

Equally to equation 2.4, the electron mobility results from equation 8.4.

$$\mu_n = \underbrace{\frac{q \cdot f_{atj,n}}{k_B T n}}_{\text{frequency}} \cdot \underbrace{\left(\int_{-\infty}^{E_{tr,n}} g_L(E') dE' \right)^{-\frac{2}{3}}}_{\text{jump distance}} \cdot \underbrace{\int_{-\infty}^{E_{tr,n}} \frac{g_L(E') \cdot e^{-\frac{E' - E_{tr,n}}{k_B T}}}{1 + e^{-\frac{E' - E_F}{k_B T}}} dE'}_{\text{activation energy}} \quad (8.4)$$

The Einstein relation is also valid for electrons as given in equation 8.5 with the limits $c_{n,min}$ and $c_{n,max}$ in equation 8.6. Here, the same limits are valid as for holes described in chapter 3.1.

$$D_n = g_{3,n} \cdot \frac{\mu_n}{q} \quad (8.5)$$

$$g_{3,n} = \frac{n}{\frac{dn}{dE_F}} \text{ for } c_{n,min}N_H < p < c_{n,max}N_H \quad (8.6)$$

Table 8.2: Materials under examination

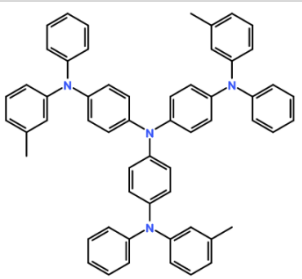
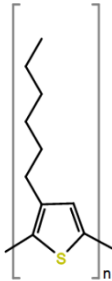
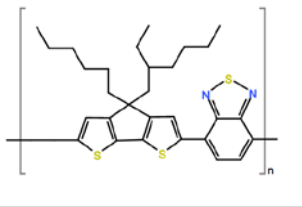
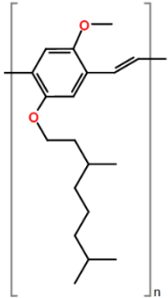
Abbreviation	chemical name	molecular formula	structure	molecular orbitals
MTDATA	4,4',4''-Tris[phenyl(m-tolyl)amino]triphenyl-amine	$C_{57}H_{48}N_4$		HOMO: 5-5.1 eV [2, 145, 174] LUMO: 1.9-2 eV [2, 174]
P3HT	Poly(3-hexylthiophene-2,5-diyl)	$(C_{10}H_{14}S)_n$		HOMO: 4.65-5.2 eV [71, 96, 98, 157, 173] LUMO: 2.13-3.2 eV [71, 96, 98, 157, 173]
PCPDTBT	Poly[2,6-(4,4-bis(2-ethylhexyl)-4H-cyclopenta[2,1-b;3,4-b']dithiophene)-alt-4,7(2,1,3-benzothiadiazole)]	$(C_{31}H_{38}N_2S_3)_n$		HOMO: 5.3-5.5 eV [87, 108, 173, 176] LUMO: 3.42-3.6 eV [87, 108, 173, 176]
MDMO-PPV	Poly[2-methoxy-5-(3',7'-dimethyloctyloxy)-1,4-phenylenevinylene]	$(C_{19}H_{28}O_2)_n$		HOMO: 5.1-5.33 eV [6, 72, 128, 173] LUMO: 2.7-2.97 eV [6, 72, 128, 173]

Table 8.3: Organic contact materials

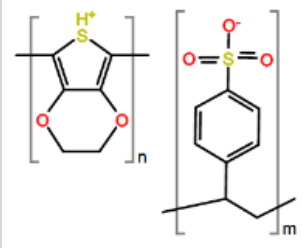
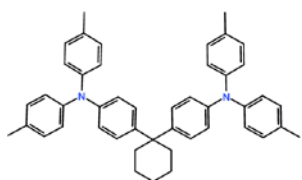
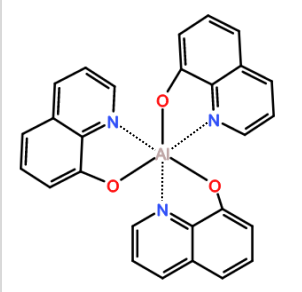
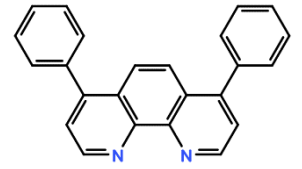
Abbreviation	chemical name	molecular formula	structure	molecular orbitals
PEDOT:PSS	poly(3,4-ethylenedioxythiophene): polystyrene sulfonate	$(C_7H_6SO_2^+)_n$: $(C_8H_9SO_3^-)_m$		HOMO: 5.15 eV [40, 145] LUMO: 3.66 eV [16, 99]
TAPC	4,4'-Cyclohexylidenebis[N,N-bis(4-methylphenyl)benzenamine]	$C_{46}H_{46}N_2$		HOMO: 5.5 eV [174] LUMO: 2 eV [174]
Alq3	Aluminium-tris(8-hydroxyquinolin)	$C_{27}H_{18}AlN_eO_3$		HOMO: 5.6-6.6 eV [3, 174] LUMO: 3.3 eV [3, 174]
Bphen	4,7-Diphenyl-1,10-phenanthroline	$C_{24}H_{16}N_2$		HOMO: 6.1-6.5 eV [97, 174] LUMO: 2.4-2.8 eV [97, 174]

Table 8.4: Cleaning process for substrates: The substrates are put sequentially into different solvents within an ultrasonic bath at 60 °C for a certain time and rinsed afterwards again with different solvents. After all steps the substrates are blown dry with nitrogen. For water is always twice distilled water used.

Step	duration	solvent	rinsing solvent
1	5 min	Aceton	Aceton
2	10 min	Mucosol:Water 1:19	water
3	10 min	water	water
4	10 min	Isopropanol:Aceton 1:1	isopropanol
5	10 min	Ethanol	water
6	5 min	water	water

Table 8.5: Spin coater Prozess for PEDOT:PSS

Step	execution
1	Mixing PEDOT:PSS (Hil-E100 from Haereus) with twice distilled water in relation of 1:1. The solution is kept for 30 min in a ultrasonic bath.
2	15 min at 110 °C UVO
3	Filtering of the solution through a 0.45 µm PVDF filter.
4	Spin coating (200 µl per sample): 1. 500 rpm; 5000 $\frac{\text{rpm}}{\text{s}}$; 5 s 2. 5000 rpm; 5000 $\frac{\text{rpm}}{\text{s}}$; 30 s
5	As the total substrate is covered, the bottom ITO contacts are wiped clean for the contacting of finished samples. A wet piece of cloth is used for that.
6	Tempering at 130 °C for 5 min
7	Tempering at 130 °C for 25 min inside the glovebox

Table 8.6: Spin coater Prozess for P3HT and PCPDTBT

Step	execution
1	Preparing the solution: It is set up with a concentration of $20 \frac{\text{mg}}{\text{ml}}$ Chlorbenzene within nitrogen atmosphere. The solution was shaken with the vortex Genie 2 (Scientific Industries, Inc) for at least 72 h. After dissolving all by eye visible particles, the solution is once heated up to 60°C .
2	Spin coating (50 μl per sample): 1. 200 rpm; ACL=1; 10 s 2. 75 rpm; ACL=1; 60 to 300 s 3. 200 rpm; ACL=1; 30 s 4. 75 rpm; ACL=1; 10 s 5. 500 rpm; ACL=1; 40 s 6. 3000 rpm; ACL=10; 20 s
3	As the total substrate is covered, the bottom ITO contacts are wiped clean for the contacting of finished samples. A piece of cloth soaked with Chlorbenzene is used for that.

Table 8.7: Spin coating process for MDMO-PPV

Step	execution
1	Preparing the solution: It is set up with a concentration of $5 \frac{\text{mg}}{\text{ml}}$ Chlorbenzene within nitrogen atmosphere. The solution was shaken with the vortex Genie 2 (Scientific Industries, Inc) for at least 72 h. After dissolving all by eye visible particles, the solution is once heated up to 60°C .
2	Spin coating (80 μl per sample): 1. 75 rpm; ACL= $120 \frac{\text{rpm}}{\text{s}}$; 180 to 480 s 2. 200 rpm; ACL= $120 \frac{\text{rpm}}{\text{s}}$; 20 s 1. 600 rpm; ACL= $120 \frac{\text{rpm}}{\text{s}}$; 30 s 1. 3000 rpm; ACL= $1200 \frac{\text{rpm}}{\text{s}}$; 20 s
3	As the total substrate is covered, the bottom ITO contacts are wiped clean for the contacting of finished samples. A piece of cloth soaked with Chlorbenzene is used for that.

8.3 Details of the SCLC simulation

For the simulation (Chap. 3), the software Atlas from Silvaco is used. The standard code for the simulation is given in chapter 8.3.1. This code allows for all described parameter variations as described in the code comments marked in green with # in front of the comment. The code itself is meant to use with the software deckbuild, also from Silvaco, which starts the Atlas simulation.

Because of the large amount of data, the determination of the transient peak position is automated with the criteria described in chapter 8.3.2. The algorithm for the applied fits is given in chapter 8.3.3. The results for the fit parameters (Chap. 3.2) are given in table 8.8. The standard deviation is calculated between the fit curve and the original data points.

Table 8.8: results for fit parameters

parameter	A_{simu}	B_{simu}	C_{simu}	deviation
basic	-3.243	-0.6372	-0.129	0.022
rise time (20 ns)	-0.07076	-1.12	-0.477	0.035
rise time (50 ns)	-1.973	-0.7319	-0.1442	0.02
rise time (100 ns)	-0.7502	-0.8667	-0.2039	0.026
built-in field (0.2 V)	-0.438	-0.9638	-0.4644	0.024
built-in field (0.5 V)	-0.845	-0.8658	-0.3846	0.013
built-in field (1 V)	-1.551	-0.7229	-0.3264	0.009
injection barrier (0.1 eV)	-2.898	-0.7164	-0.09371	0.021
injection barrier (0.3 eV)	-4.491	-0.4229	-0.1763	0.018
injection barrier (0.5 eV)	$9.906 \cdot 10^{-7}$	-3.4014	-0.9028	0.017
steady state SCLC ($10^{20} \frac{1}{\text{cm}^3}$)	0.7983	-0.833		0.067
steady state SCLC ($5 \cdot 10^{20} \frac{1}{\text{cm}^3}$)	1.7983	-0.283		0.018
steady state SCLC ($10^{21} \frac{1}{\text{cm}^3}$)	-6.907	0.069		0.031

8.3.1 Atlas program code

```
## Defining Atlas as default simulator:
deckbuild -as
go atlas
title simulation of steady state SCLC at an Organic hole only diode
## Change the material thickness here
set anode_thick=0.2
set Organic_thick=0.025
set cathode_thick=0.2
#thickness of contacts have no influence on the simulation

## Set Gaussian Profile
set Organic_h_width=0.1
set Organic_Nh=1e20
set Organic_h_width_1=0.1
set Organic_ELUMO=2
set Organic_E_HOMO=5
#standard values for ideal trap free SCLC are used in this file
#The position of HOMO and LUMO are important in respect to contact work functions
#positive shift values means a shift closer to the fermi level

## Set hole doping of organic layer
set acceptor=0
#defines the doping amount of the semiconductor

## Set permittivity for all materials (only used for the single organic layer)
set Epsilon=3

## set parameters for hopping mobility
set Organic_HopFreq_p=1e11
set Organic_HopGamma_p=3e7
#the gamma value is considered as constant

## set contact work functions
set anode_work=5
set cathode_work=5
#anode: injection electrode for holes
#cathode: ejection electrode for holes, here: perfect electron blocking electrode

## set simulation parameters
set V_step=$Organic_thick / 2
```

```

set ramptime=20e-9
set mesh_multi=3
#defines the speed and accuracy of the simulation

## set resistance
set contact_S=0.001
set contact_P=1e12
#defines a parallel and serial resistance to the organic layer by changing the mobility
# and width of a parallel silicon layer to the organic layer
#resistances are set here for layers of size 7.5 mm2 and recalculated within the program
# to match the simulated device area of 1e4 μm2
set Rthickness=$Organic_thick / 0.300
set Rmobility=9.35 / $contact_P * 2e-7

## set capacitance
set capacitance=0.1
#sets the parallel capacitance in [nF] set width_C=$capitance / 8.854e-9 * $Organic_thick * 0.00133
/ 10 #Last factor: permittivity of capacitance to reduce capacitance width
## set which parameter is changes
set Change=1e20

#### end of parameter settings ####

#calculation of layer thicknesses
set layer1_thick= $anode.thick
set layer2_middle= $anode.thick+$Organic_thick/2
set layer2_thick= $anode.thick+$Organic_thick
set layer3_thick= $anode.thick+$Organic_thick+$cathode.thick

## Defning 2D mesh; a width of 1μm is assumed by Atlas
mesh smooth=4 space.mult=$mesh_multi #space.multij1: more accuracy; j1: faster simulation
#locations are set in μm
x.mesh location= 0.0 spacing=100
x.mesh location= 1e4-$width_C / 100 spacing=100
x.mesh location= 1e4 spacing=1
x.mesh location= 1e4+$width_C / 100 spacing=1
x.mesh location= 1e4+$width_C * 0.99 spacing=1
x.mesh location= 1e4+$width_C spacing=0.1
x.mesh location= 1e4+$width_C+$Rthickness / 10 spacing=0.1
x.mesh location= 1e4+$width_C+$Rthickness spacing=0.1

```

```

y.mesh location=0 spacing=0.05
y.mesh location=$layer1_thick spacing=0.00005
y.mesh location=$layer1_thick+0.01 spacing=0.00005
y.mesh location=$layer1_thick+0.04 spacing=0.0001
y.mesh location=$layer2_middle spacing=0.0001
y.mesh location=$layer2_thick-0.04 spacing=0.0001
y.mesh location=$layer2_thick-0.01 spacing=0.00005
y.mesh location=$layer2_thick spacing=0.00005
y.mesh location=$layer3_thick spacing=0.05

## Defining materials and contacts:
#Organic
region num=1 name=Organic x.min=0 x.max=1e4 \
y.min=$layer1_thick y.max=$layer2_thick \
material=organic
#acceptor=$acceptor
#acceptor amount can be activated by including the corresponding statement
#isolator
region num=2 name=isolator x.min=1e4 x.max=1e4+$width_C \
y.min=$layer1_thick y.max=$layer2_thick \
material=vacuum

#parallel resistance
region num=3 name=silicon x.min=1e4+$width_C x.max=1e4+$width_C+$Rthickness \
y.min=$layer1_thick y.max=$layer2_thick \
material=silicon \
acceptor=1e20
#electrodes
electrode num=1 name=anode x.min=0 x.max=1e4 \
y.min=0 y.max=$layer1_thick \
material=ITO electrode num=2 name=cathode x.min=0 x.max=1e4 \
y.min=$layer2_thick y.max=$layer3_thick \
material=Nickel electrode num=3 name=anode x.min=1e4 x.max=1e4+$width_C+$Rthickness y.min=0
y.max=$layer1_thick \
material=Aluminum electrode num=4 name=cathode x.min=1e4 x.max=1e4+$width_C+$Rthickness
y.min=$layer2_thick y.max=$layer3_thick \
material=Aluminum
###End of device definition###

# Set parameters for Organic
material region=1\
paasch.gfi=1 profile.gauss="GaussProfile_basis"\

```

```

eg300=$Organic_E_HOMO-$Organic_E_LUMO permittivity=$Epsilon \
nc300=$Organic_Nh nv300=$Organic_Ne affinity=$Organic_E_LUMO \
HOPN.GAMMA=$Organic_HopGamma_n HOPN.V0=$Organic_HopFreq_n \
HOPP.GAMMA=$Organic_HopGamma_p HOPP.V0=$Organic_HopFreq_p \
NTV.GAUSS=$Organic_Nh NTC.GAUSS=$Organic_Ne \
SIGC.GAUSS=$Organic_e_width SIGV.GAUSS=$Organic_h_width
#"profile.gauss="GaussProfile"" saves the Gaussprofile in a text file

#set parameters for parallel capacitance
material region=2 permittivity=10

#set parameters for parallel resisatance
material region=3 eg300=4 affinity=5

## Defining defects
odefects hopping
#activates the hopping model for the mobility

## Defining work funtions in [eV]
# Nickel(Cathode)
contact num=2 workfunc=$cathode_work
# ITO (Anode)
contact num=1 workfunc=$anode_work
#con.resist=$contact_S * 0.075 * (1e4+$width_C+$Rthickness) / 1e4
#the contact resistance can be included by the above statement

# contacts for parallel resistance and capacitance (ohmic contacts)
contact num=3
contact num=4

## Defining physical models for the simulation
models hopmob print

## Defining mobility parameters
mobility material=Organic hopmob.p
mobility material=silicon mup=$Rmobility mun=1e-15
#the hopping mobility is activated for holes in the organic semiconductor
#the parallel resistance is defined by the hole mobility of silicon; the electron mobility is set
# low, so the electrons have no influence

output con.band val.band E.fielde e.mobility h.mobility

```

```

#For necessary initial guess:
method Newton
solve init
solve vanode=0
save outfile=steady_IV_P${Change}W_V0X_f${Organic_HopFreq_p}Y_d${Organic_thick}Z.str
## method
method newton carriers=1 hole clim.dd=1e4 em.Damping emd.max.iter=5 emd.skip.iter=0 \
itlimit=1000 itmin=1 tol.relax=2 nrcriter=0.1 xnorm rhsnorm maxtraps=10
#the parameters for the newton iteration are set here
#for including minority charge carriers (electrons) "carriers=2" without "hole" statement is necessary
#probably there is no need to change further parameters to obtain convergence

# Steady state simulation
# Ramping Vanode to 10V to plot the I-V Characteristics and get output at every voltage step

#for good initial guess; slow start of voltage ramp:
solve vanode=1e-5
solve vanode=5e-5
solve vanode=1e-4
solve vanode=5e-4
solve vanode=1e-3
solve vanode=5e-3
solve vanode=1e-2
log outfile=steady_LOG_JV.log
set vmax1=10*${Organic_thick}
solve vanode=${V_step} vstep=${V_step} vfinal=${Vmax1} vcathode=0 name=anode
save outfile=steady_IV_P${Change}W_V${Vmax1}X_f${Organic_HopFreq_p}Y_d${Organic_thick}Z.str
####
set vmax2=10*${Organic_thick}*2
solve vanode=${Vmax1}+${V_step} vstep=${V_step} vfinal=${Vmax2} vcathode=0 name=anode
save outfile=steady_IV_P${Change}W_V${Vmax2}X_f${Organic_HopFreq_p}Y_d${Organic_thick}Z.str
####
set vmax3=10*${Organic_thick}*3
solve vanode=${Vmax2}+${V_step} vstep=${V_step} vfinal=${Vmax3} vcathode=0 name=anode
save outfile=steady_IV_P${Change}W_V${Vmax3}X_f${Organic_HopFreq_p}Y_d${Organic_thick}Z.str
####
set vmax4=10*${Organic_thick}*4
solve vanode=${Vmax3}+${V_step} vstep=${V_step} vfinal=${Vmax4} vcathode=0 name=anode
save outfile=steady_IV_P${Change}W_V${Vmax4}X_f${Organic_HopFreq_p}Y_d${Organic_thick}Z.str
####
set vmax5=10*${Organic_thick}*5
solve vanode=${Vmax4}+${V_step} vstep=${V_step} vfinal=${Vmax5} vcathode=0 name=anode

```

```

save outfile=steady_IV_P${Change}W_V${Vmax5}X_f${Organic_HopFreq_p}Y_d${Organic_thick}Z.str
####

## Extracting Current Density versus Voltage
# Surface Area = 1um * 1e4um = 1e4 μm2 = 1e-4 cm2
# Current Density (in  $\frac{A}{cm^2}$ ) = Simulated current [in A] / (1e-4 cm2)
# = 1e8 * Simulated Current [in  $\frac{A}{cm^2}$ ]
extract name="J_vs_V" curve(v."anode", 1e4*i."anode") outfile= \
"JV_P${Change}W_f${Organic_HopFreq_p}Y_d${Organic_thick}Z.dat"
## Extracting Current Density versus electric field
# field strength = voltage / thicknes organic semiconductor
# field strength (in  $\frac{kV}{\mu m}$ ) = Simulated voltage [V] / thickness [nm] = Simulated Voltage / organic
thickness / 1000 [ $\frac{kV}{\mu m}$ ]
extract name="J_vs_E" curve(v."anode" / $Organic_thick / 1000, 1e4*i."anode") outfile=\
"JE_P${Change}W_f${Organic_HopFreq_p}Y_d${Organic_thick}Z.dat"

#saving data for intermediate voltage steps of the steady state simulation
set loop_voltage=0
set loop_var=0
loop steps=6
extract init infile=\
"steady_IV_P${Change}W_V${loop_voltage}X_f${Organic_HopFreq_p}Y_d${Organic_thick}Z.str"
extract name="Voltage_${loop_voltage}V_E" \
curve(depth, impurity="Electric Field" material="organic" x.val=1e2) \
outfile=\
"steady_ElectricField_P${Change}W_V${loop_voltage}X_f${Organic_HopFreq_p}Y_d${Organic_thick}Z.dat"
extract name="Voltage_${loop_voltage}V_Phi" \
curve(depth, impurity="Potential" material="organic" x.val=1e2) \
outfile=\
"steady_Potential_P${Change}W_V${loop_voltage}X_f${Organic_HopFreq_p}Y_d${Organic_thick}Z.dat"
extract name="Voltage_${loop_voltage}V_p" \
curve(depth, impurity="Hole Conc" material="organic" x.val=1e2) \
outfile=\
"steady_HoleConc_P${Change}W_V${loop_voltage}X_f${Organic_HopFreq_p}Y_d${Organic_thick}Z.dat"
extract name="Voltage_${loop_voltage}V_mup" \
curve(depth, p.mobility material="organic" x.val=1e2) \
outfile=\
"steady_Hmobility_P${Change}W_V${loop_voltage}X_f${Organic_HopFreq_p}Y_d${Organic_thick}Z.dat"
set loop_var=$loop_var+1
set loop_voltage=10*$Organic_thick*$loop_var
l.end

```

```

# transient simulation

method newton carriers=1 hole clim.dd=1e4 em.Damping emd.max.iter=5 emd.skip.iter=0 itlimit=1000
itmin=1 tol.relax=2 nrcriter=0.1 xnorm rhsnorm maxtraps=10 tol.time=1e-6
#the parameters for the newton iteration are set here

set looptrans_var = 1
loop steps=5
set Vtrans = 10 * $Organic_thick * $looptrans_var

solve init
solve vanode=0
log outfile=trans.LOG.${Vtrans}V_Jt.log

#####
solve vanode=$Vtrans ramptime=$ramptime tstop=100e-9 timestep=1e-10
save outfile=trans_V${Vtrans}X_Jt_t1_P${Change}W_f${Organic_HopFreq_p}Y_d${Organic_thick}Z.str
#####
solve vanode=$Vtrans ramptime=0 tstop=300e-9 timestep=3e-10
save outfile=trans_V${Vtrans}X_Jt_t2_P${Change}W_f${Organic_HopFreq_p}Y_d${Organic_thick}Z.str
#####
solve vanode=$Vtrans ramptime=0 tstop=500e-9 timestep=5e-10
save outfile=trans_V${Vtrans}X_Jt_t3_P${Change}W_f${Organic_HopFreq_p}Y_d${Organic_thick}Z.str
#####
solve vanode=$Vtrans ramptime=0 tstop=2000e-9 timestep=20e-10
save outfile=trans_V${Vtrans}X_Jt_t4_P${Change}W_f${Organic_HopFreq_p}Y_d${Organic_thick}Z.str
#####
solve vanode=$Vtrans ramptime=0 tstop=1e-3 timestep=100e-10
save outfile=trans_V${Vtrans}X_Jt_t5_P${Change}W_f${Organic_HopFreq_p}Y_d${Organic_thick}Z.str
#####

## Extracting Current Density versus time
# Surface Area = 1 μm * 1e4 μm = 1e4 μm2 = 1e-4 cm2
# Current Density (in  $\frac{A}{cm^2}$ ) = Simulated current [in A] / (1e-4 cm2) = 1e8 * Simulated Current [in  $\frac{A}{cm^2}$ ]
extract name="J_vs_t" curve(time, 1e4*i."anode") \
outfile="trans_Jt_V${Vtrans}X_Jt_P${Change}W_f${Organic_HopFreq_p}Y_d${Organic_thick}Z.dat"

#saving data for intermediate voltage steps of the steady state simulation
set loop_var=1
loop steps=5
extract init infile=\
"trans_V${Vtrans}X_Jt_t${loop_var}_P${Change}W_f${Organic_HopFreq_p}Y_d${Organic_thick}Z.str"

```

```

extract name="trans_V${Vtrans}X_t${loop_var}_E" \
curve(depth, impurity="Electric Field" material="organic" x.val=1e2) \
outfile=\
"trans_t${loop_var}_ElectricField_P${Change}W_V${Vtrans}X_f${Organic_HopFreq_p}Y_d${Organic_thick}Z.dat"
extract name="trans_V${Vtrans}X_t${loop_var}_Phi" \
curve(depth, impurity="Potential" material="organic" x.val=1e2) \
outfile=\
"trans_t${loop_var}_Potential_P${Change}W_V${Vtrans}X_f${Organic_HopFreq_p}Y_d${Organic_thick}Z.dat"
extract name="trans_V${Vtrans}X_t${loop_var}_p" \
curve(depth, impurity="Hole Conc" material="organic" x.val=1e2) \
outfile=\
"trans_t${loop_var}_HoleConc_P${Change}W_V${Vtrans}X_f${Organic_HopFreq_p}Y_d${Organic_thick}Z.dat"
extract name="trans_V${Vtrans}X_t${loop_var}_mup" \
curve(depth, p.mobility material="organic" x.val=1e2) \
outfile=\
"trans_t${loop_var}_Hmobility_P${Change}W_V${Vtrans}X_f${Organic_HopFreq_p}Y_d${Organic_thick}Z.dat"
set loop_var=${loop_var}+1
l.end
log off
set looptrans_var = $looptrans_var + 1
l.end

quit

```

8.3.2 Algorithm for finding transient peak

For the automated determination of the transient current peak, the minimum between charging and transient peak is determined first. By starting at $t = 0$, the first data point is defined as this minimum, which has a lower current than the five previous and five following data points. From this time on, following the time axis, the first data point is defined as the transient maximum, which has a higher current than the five previous and five following data points. Additionally, it is checked, if the current of this transient peak is higher than the steady state current. With this concept, the first maximum is determined. This is crucial because of the oscillation of the signal after this first peak [153].

8.3.3 Algorithm for fitting the simulated normalized mobility

The fitting (Chap. 3.2) is done using the algorithm shown in figure 8.2, which optimizes a single coefficient. Two functions F are created with a maximum and minimum coefficient c . The results for $F(d, c_{max})$ and $F(d, c_{min})$ are calculated and the squared difference of the calculated and original value is determined. The coefficient is determined with the precision of 0.001. As long as the difference between c_{max} and c_{min} is larger, the coefficients will be optimized further. The coefficient which results in the larger deviation is reduced (or increased) by $(c_{max} - c_{min})/10$. If the precision is reached, the average value between minimum and maximum coefficient is used as the result. Additionally, the deviation to the original data is calculated. As the deviation is zero at $1 \mu\text{m}$ due to normalization, the data at this thickness is excluded from the deviation calculation. The total deviation results from adding all squared deviations divided by the number of data points.

For the used fit (Equ. 3.15), there are more than one unknown coefficient. Thus, in case of two coefficients, the discussed algorithm is used within itself a second time. For each c_{max} and c_{min} , the optimal second coefficient is determined with this algorithm, before calculating the deviation of c_{max} and c_{min} . For three coefficients, three nested algorithms are used.

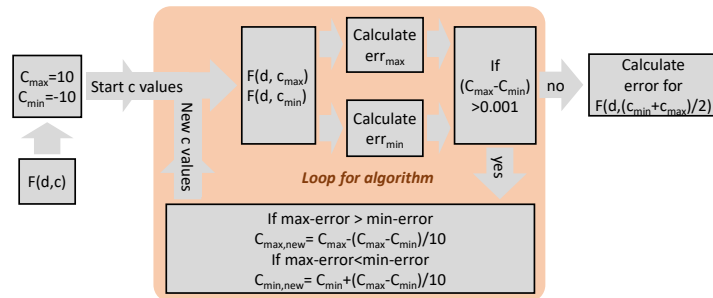


Figure 8.2: Algorithm used for fitting curves.

8.4 Details of the SCLC measurement and control circuits

Figure 8.4 shows the complete circuit for the transient space charge limited current measurements as described in chapter 6.3. The corresponding PCB layout is given in figure 8.3. The used elements, their explanations and the corresponding device names used in chapter 6.3 are listed in table 8.10.

The circuit is controlled by the manual switches in the external circuit (App. 8.5). This circuit has three voltage supplies, which have all the same ground potential: -15 V and 15 V for power supply of all elements and the pulse voltage supply $V_S = 3.5$ to 50 V. Deactivating the indicated switch starts the measurement by setting the gate potential of T1 or T2 to the ground potential. All SSR's are controlled by changeover switches, as well as T4 and T5. The capacitors are for additional input voltage stabilization.

Table 8.9 shows the calibration of the measurement circuit. This calibration was determined by putting a known resistance at the sample position in series with a multimeter. Thus, the current through the sample, the applied voltage and the voltage at the oscilloscope were measured. For this calibration, the complete step voltage range was used. The calibration function is a linear fit of the form $I [\text{in A}] = a \cdot V [\text{in V}] + b$ and the resulting accuracy was over 0.999 in all cases.

Table 8.9: Calibration parameters for the circuit shown in figure 8.3

$R_1 \rightarrow \infty$	$R_1 = 174 \Omega$	$R_1 = 34.8 \Omega$	$R_1 = 8.06 \Omega$	$R_1 = 2 \Omega$
for $R_m = 30 \Omega$:				
$a = 3.546 \cdot 10^{-3}$	$a = 7.201 \cdot 10^{-4}$	$a = 1.782 \cdot 10^{-4}$	$a = 4.345 \cdot 10^{-5}$	$a = 1.151 \cdot 10^{-5}$
$b = -2.769 \cdot 10^{-4}$	$b = 1.918 \cdot 10^{-6}$	$b = -8.678 \cdot 10^{-6}$	$b = -5.149 \cdot 10^{-6}$	$b = -4.392 \cdot 10^{-6}$
for $R_m = 300 \Omega$:				
$a = 8.822 \cdot 10^{-2}$	$a = 2.030 \cdot 10^{-2}$	$a = 4.935 \cdot 10^{-3}$	$a = 1.2144 \cdot 10^{-3}$	$a = 3.239 \cdot 10^{-4}$
$b = 5.463 \cdot 10^{-4}$	$b = -2.964 \cdot 10^{-4}$	$b = -4.708 \cdot 10^{-5}$	$b = -8.492 \cdot 10^{-5}$	$b = -7.018 \cdot 10^{-5}$

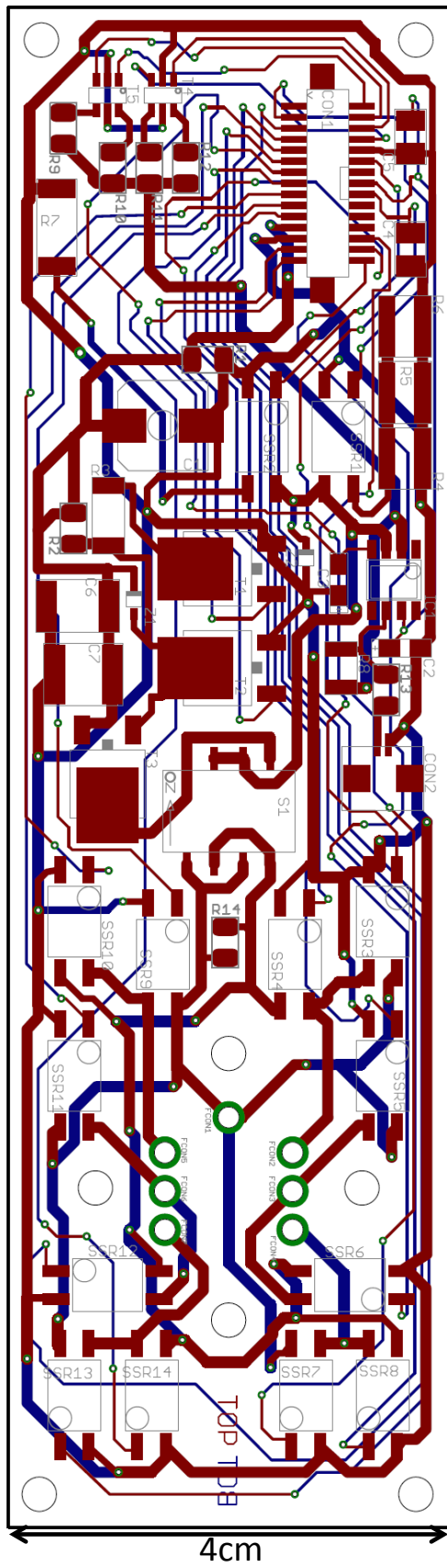


Figure 8.3: PCB: red lines are top wiring and blue are bottom wiring; all devices are on the top side and described in table 8.10

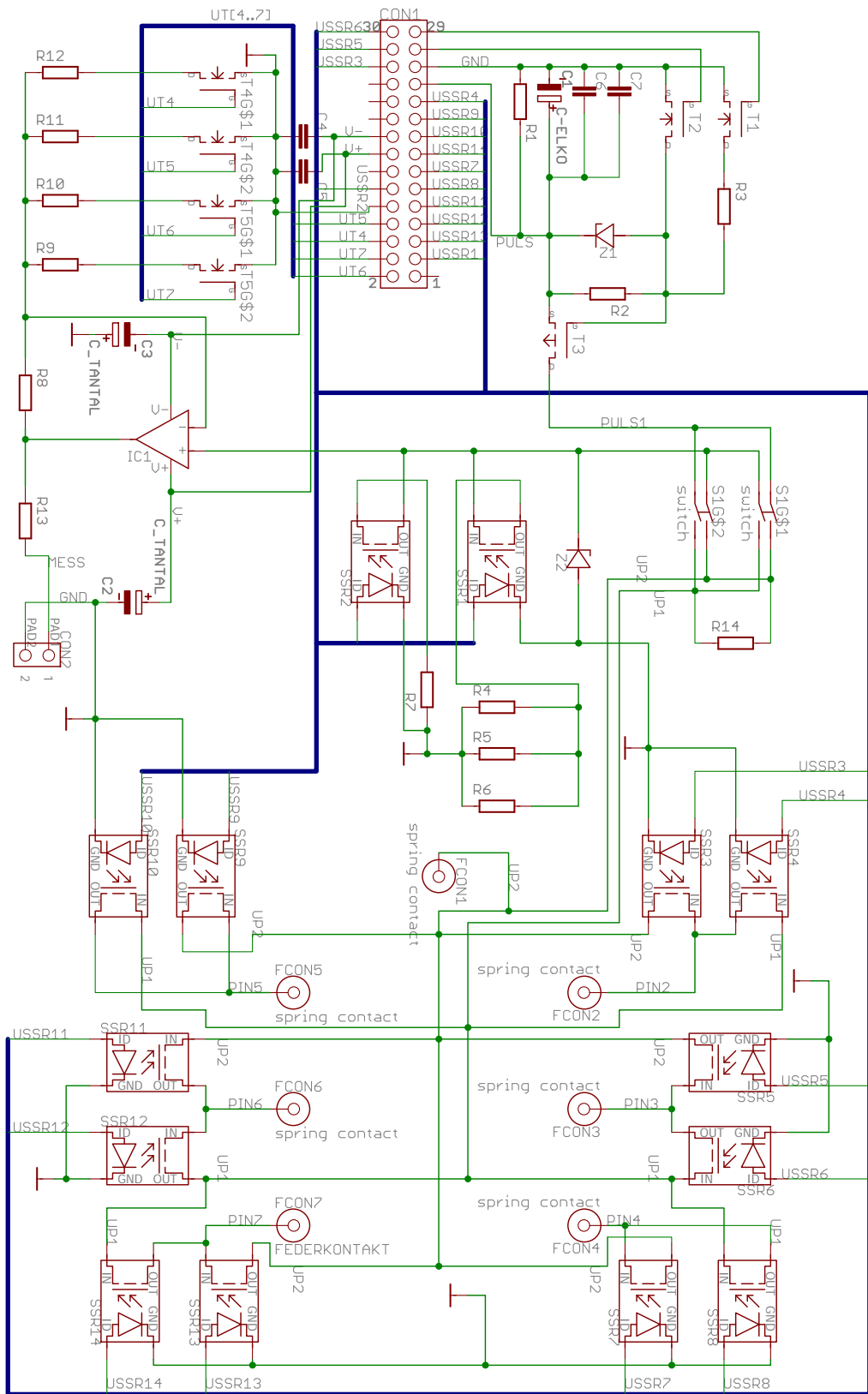


Figure 8.4: Complete circuit of the PCB, all devices are described in table 8.10.

Table 8.10: Description of all elements used in the circuit shown in figure 8.3

device	name in chapter 6.3	description	model	manufacturer	explanations	date sheet
R1	R_{dch1}	5.36 M Ω	MC0125W120615M36	Farnell (multicomp)	for discharging of capacitors if step voltage is turned off	[55]
R2	R_{step}	1 k Ω	WF12P1001FTL	Walsin	Voltage divider with R3 to protect T3 from too high voltages if step voltage is larger than 20V	[56]
R3	R_{50}	1.5 k Ω	MCPWR10FTEQ1501	Farnell (multicomp)	Voltage divider with R2 to protect T3 from too high voltages if step voltage is larger than 20V	[39]
R4 to 6	R_m	30 Ω	WK73R2HTTE30R0F	KAO Speer	combined in a parallel circuit: $R_m = 10 \Omega$	[49]
R7	R_m	300 Ω	MCPWR12FTEA3000	Farnell (multicomp)	alternative R_m	[39]
R8	R_2	604 Ω	ERJP14F6040U	Panasonic	R_2	[36]
R9	R_1	174 Ω	ERJP08F1740V	Panasonic	possible choice of R_1	[36]
R10	R_1	34.8 Ω	CRCW120634R8FKEA	Vishay	possible choice of R_1	[53]
R11	R_1	8.06 Ω	RK73H2BTTD8R06F	KAO Speer	possible choice of R_1	[48]
R12	R_1	2 Ω	RC1206FR-072RL	Yageo	possible choice of R_1	[42]
R13	R_{osci}	300 Ω	CRCW1206300RFKEA	Vishay	Reduces oscillations from coupling between Oscilloscope and op-amp	[53]
R14	R_{dch2}	5.36 M Ω	MC0125W120615M36	Multicomp	for discharging of sample if step voltage is turned off	[55]
Z1	Z_S	$V_{zener} = 20 \text{ V}$	BZX84J-B20,115	NXP	protection from over voltage	[51]
Z2	Z_M	$V_{zener} = 15 \text{ V}$	BZX84J-B15,115	NXP	protection from overvoltage	[51]
T1, T2	T20, T50	$V_{ds} = -55 \text{ V}$, $V_{gs} = -20 \text{ V}$, $t_{on} < 55 \text{ ns}$, $Q_g = 19 \text{ nC}$, $R_{on} = 60 \text{ m}\Omega$	BUK9277-55A,118	NXP	T2: for step voltages up to 20V; T3: 20V to 50V	[46]

Table 8.10: (continued) Description of all elements used in the circuit shown in figure 8.3

device	name in chapter 6.3	description	model	manufacturer	explanations	date sheet
T3	T _{PULS}	$V_{ds} = 55\text{ V}$, $V_{gs} = 15\text{ V}$, $t_{on} < 47\text{ ns}$, $C_{oss} = 90\text{ pF}$, $V_{th} = -2\text{ to } -4\text{ V}$, $R_{on} = 175\text{ m}\Omega$	IRFR9024	International Rectifier	switching transistor, generating voltage step	[44]
T4, T5	T _{ampl}	$V_{ds} = 20\text{ V}$, $V_{gs} = 12\text{ V}$, $C_{oss} < 73\text{ pF}$, $R_{on} < 0,04\Omega$	NTGD3148NT1G	ON semiconductor	Choosing of R_2	[47]
C1	$C_{P,e}$	100 μF , electrolyte	EEEFK1H101P	Panasonic	stabilizing step voltage (Cp)	[35]
C2, C3		2.2 μF , tantal	TPSA225K016R1800	AVX	causing less oscillation of the op-amp [45]	[57]
C4, C5		10 nF, ceramic	MC1210B103K201CT	Farnell (multicomp)	causing less oscillation of the op-amp[45]	[38]
C6	$C_{P,f}$	220 nF, foil	ECH-U1H224GX9	Panasonic	stabilizing step voltage (Cp)	[52]
C7	$C_{P,c}$	470 nF, ceramic	C2220X474J5GACTU	Kemet	stabilizing step voltage (Cp)	[54]
S1	mis	50 m Ω , $C = 5\text{ pF}$ when closed	204-212ST	CTS Electronic Components	choosing of voltage direction at the sample	[50]
SSR1 to 14	OC	0.85 Ω when open, 0.8 pF when closed	AQY212EHA	Panasonic	SSR1 and 2: choosing of R_m ; SSR3 to 14: Choosing of one of 6 spring contacts	[43]
IC1	op. amp.	$R_{input} = 4.9\text{ M}\Omega$, CMRR=80 dB, PSRR=85dB, Slew Rate>3000 V/ μs , band width=62 MHz at amplification=2, settling time=48 ns	LM6171AIM/NOBP	Texas Instruments	operational amplifier (op-amp)	[45]
CON2		30 terminals	DF50A-30P-1V(51)	HRS	Connection to Oscilloscope	[37]
CON1		2 terminals	DF50-2DP-1V(51)	HRS	Connection to control circuit	[37]

8.5 FFT filter for smoothing of the transient SCLC signal

The mathematical principle for the FFT filter used for smoothing of the transient SCLC signal in chapter 6.4.2 is explained in the following. Essentially, a linear fit to the signal between the start and the end of a user defined range Δt_{FFT} is performed in the time domain. The software subtracts this linear fit from the original data and performs a FFT on the result. The data in the frequency domain is filtered by a parabolic low pass filter with f_{cut} defined by equation 8.7. The parabolic form of this filter is defined by 1 at 0Hz (no deletion of frequency data) and 0 at f_{cut} (complete deletion of frequency data). Afterwards, the signal is transformed back into time space by reverse FFT and the linear fit is added.

$$\Delta t_{FFT} = \frac{1}{2f_{cut}} \quad (8.7)$$

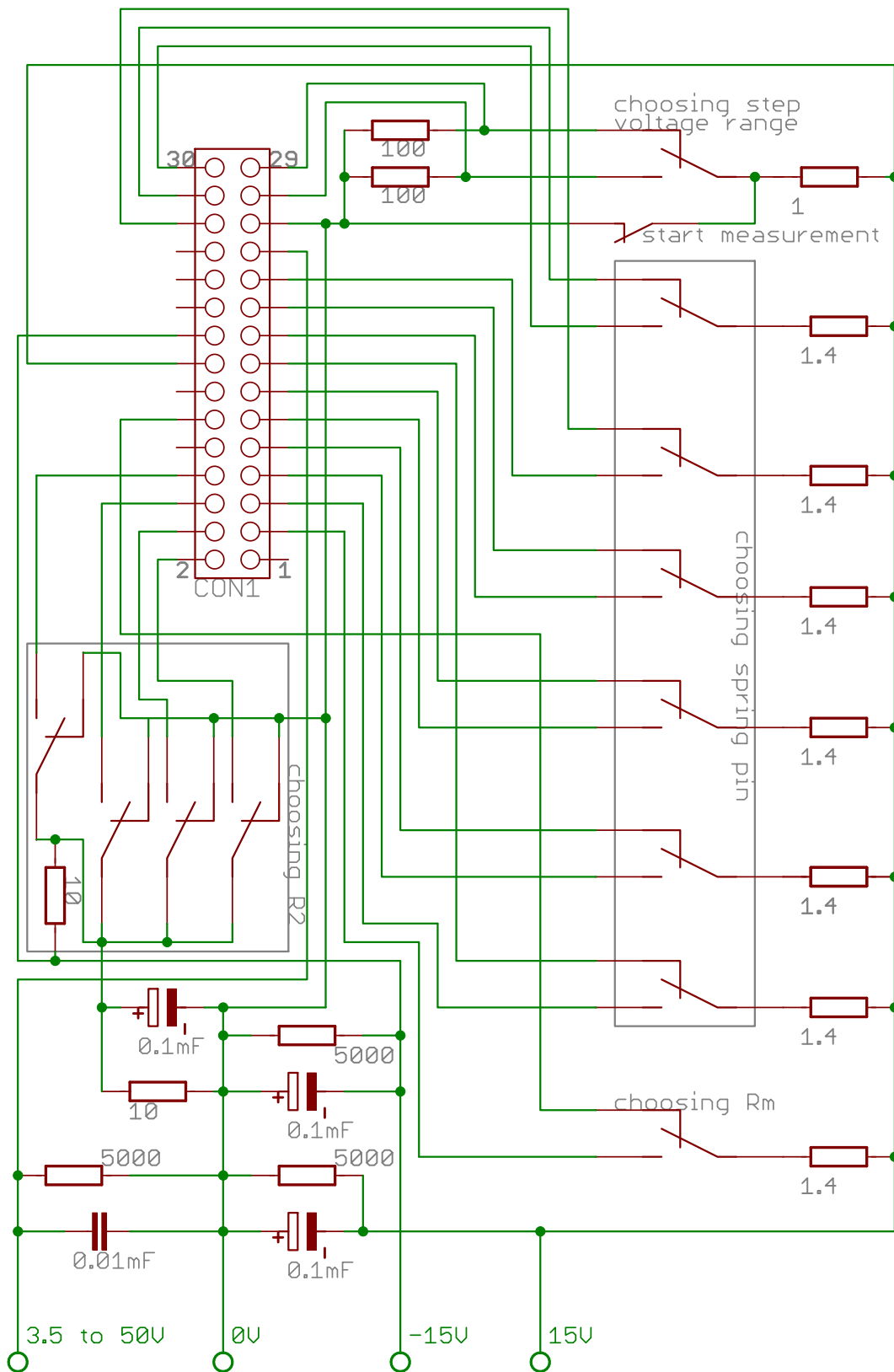


Figure 8.5: Control circuit for the circuit shown in figure 8.3 with all resistance values in kΩ

8.6 Enveloping TSC of PCPDTBT/ MDMO-PPV and original fractional TSC signals

In chapter 6.6.2, only the MIS-TSC measurement of P3HT was shown (Fig. 6.28). Here, figure 8.6 shows the corresponding enveloping measurements of PCPDTBT and MDMO-PPV. The figures 8.7 and 8.8 show the original data of the fractional MIS-TSC measurements for all polymers and aging procedures. The dashed lines are in each case the enveloping measurements. The fractional signals are always below the enveloping signal, as the total amount of trapped charge carriers is extracted over the longer measurement time. Only fractional measurements without measurement error (e.g. sudden current peaks or large noise) are used for calculating the trap distributions shown chapter 6.6.2.

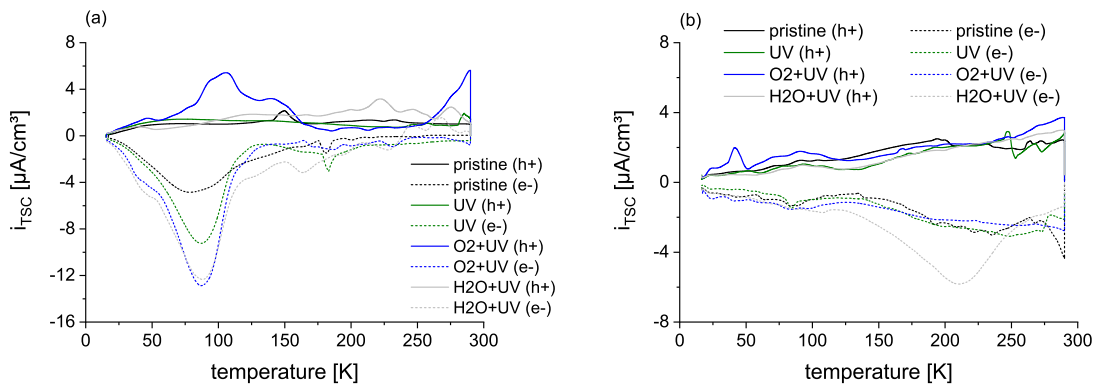


Figure 8.6: Enveloping MIS-TSC measurements of (a) PCPDTBT and (b) MDMO-PPV for pristine and aged samples.

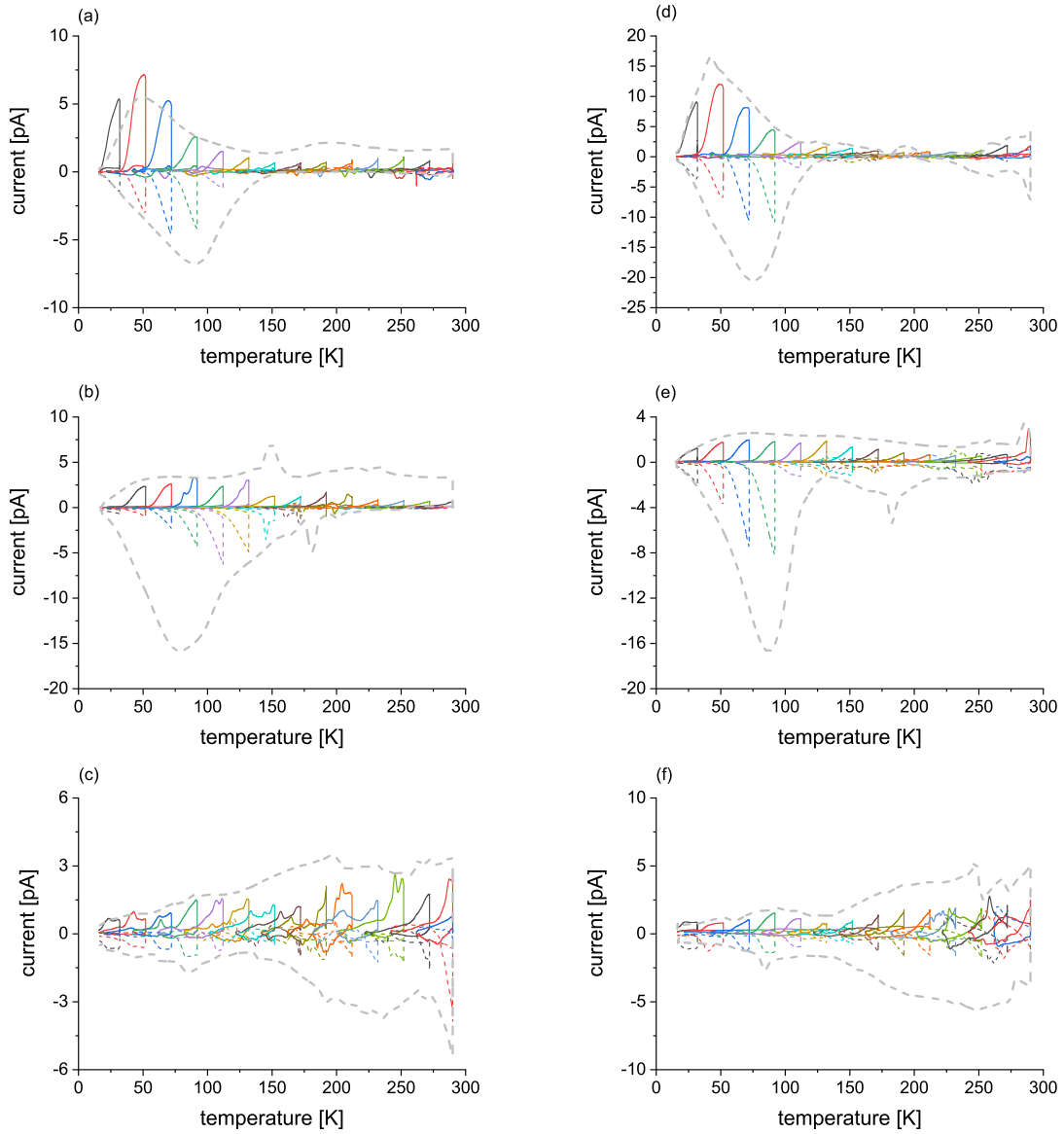


Figure 8.7: Enveloping and fractional MIS-TSC measurements of pristine (a) P3HT, (b) PCPDTBT, (c) MDMO-PPV and UV treated (d) P3HT, (e) PCPDTBT, (f) MDMO-PPV.

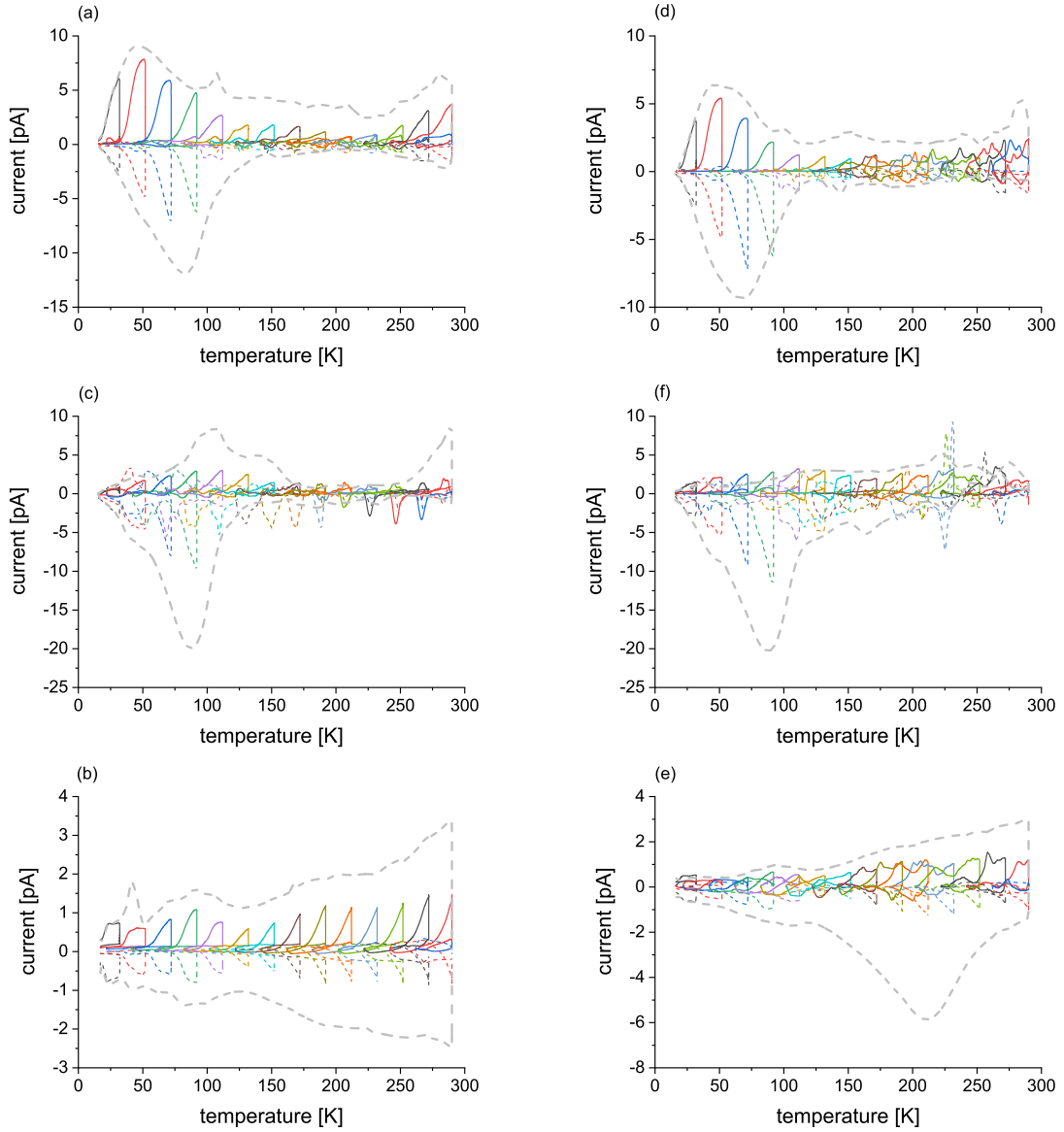


Figure 8.8: Enveloping and fractional MIS-TSC measurements of oxygen treated (a) P3HT, (b) PCPDTBT, (c) MDMO-PPV and water treated (d) P3HT, (e) PCPDTBT, (f) MDMO-PPV.

8.7 Appendix SCLC results

The coefficients determined for the fit (Equ. 6.17) used in chapter 6.6.3 are listed in chapter 8.7.1. This fit is only performed for the pristine samples. The calculation is done by simply testing all variations in the range -10 to 10. As only the P3HT original SCLC data is discussed in chapter 6.6.3, the data for PCPDTBT and MDMO-PPV is shown in chapter 8.7.2. Here, the same procedure and graphs are used as for P3HT.

8.7.1 Fits for mobility values determined with the transient SCLC method

Table 8.11: Mobility fit values for equation 6.17.

material	a_{SCLC}	b_{SCLC}	$c_{SCLC} \cdot 10^8$
P3HT (e-)	1.3	-1	0.297
P3HT (h+)	1.5	-0.2	2.03
PCPDTBT (e-)	1.7	0.2	3.35
PCPDTBT (h+)	5.1	-0.5	$9 \cdot 10^{-10}$
MDMO-PPV (e-)	0.95	-0.55	4.55
MDMO-PPV (h+)	1.3	-0.2	3.1

Table 8.12: Ratio fit values for equation 6.17.

material	a_{SCLC}	b_{SCLC}	c_{SCLC}
P3HT (e-)	-0.6	-0.4	6.7
P3HT (h+)	0	-0.05	0.88
PCPDTBT (e-)	-0.5	0.5	269
PCPDTBT (h+)	-0.2	-0.2	2
MDMO-PPV (e-)	-0.1	-0.4	1.9
MDMO-PPV (h+)	-0.3	-0.1	8.97

8.7.2 Original SCLC measurement results of PCPDTBT and MDMO-PPV without normalization

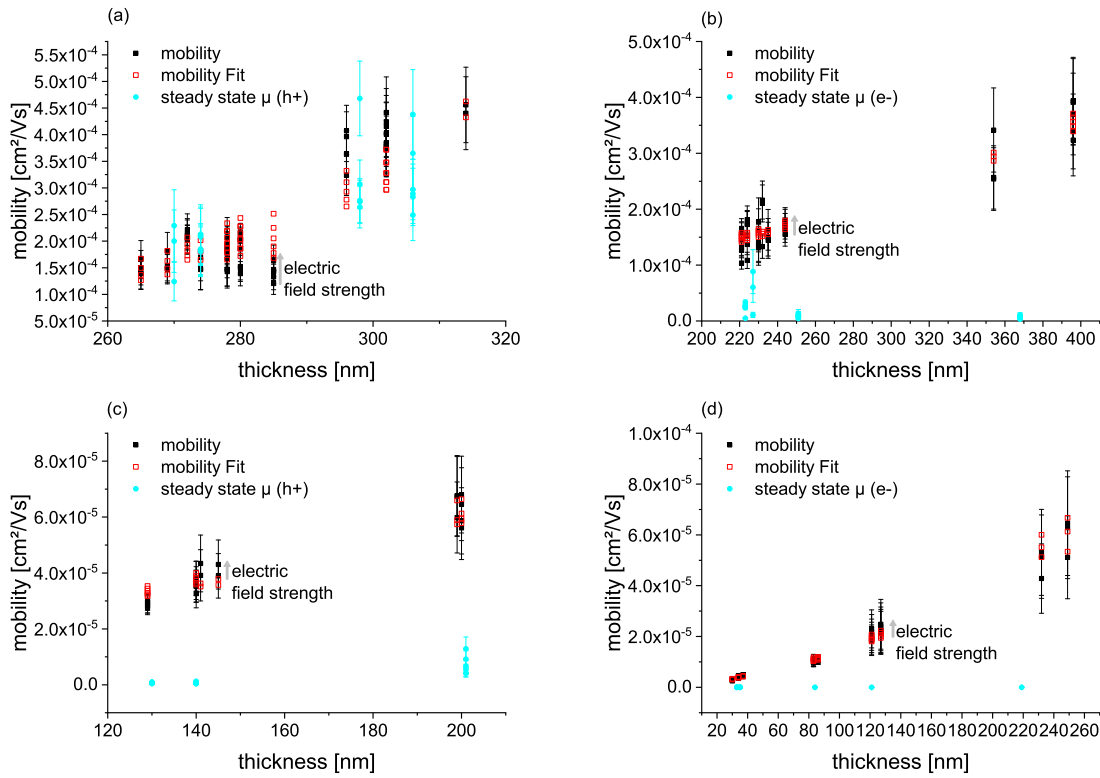


Figure 8.9: Transient and steady state mobility of (a) holes and (b) electrons for pristine PCPDTBT as well as (c) holes and (d) electrons for MDMO-PPV. The vertical distribution of the transient SCLC mobility accounts to different electrical field strength.

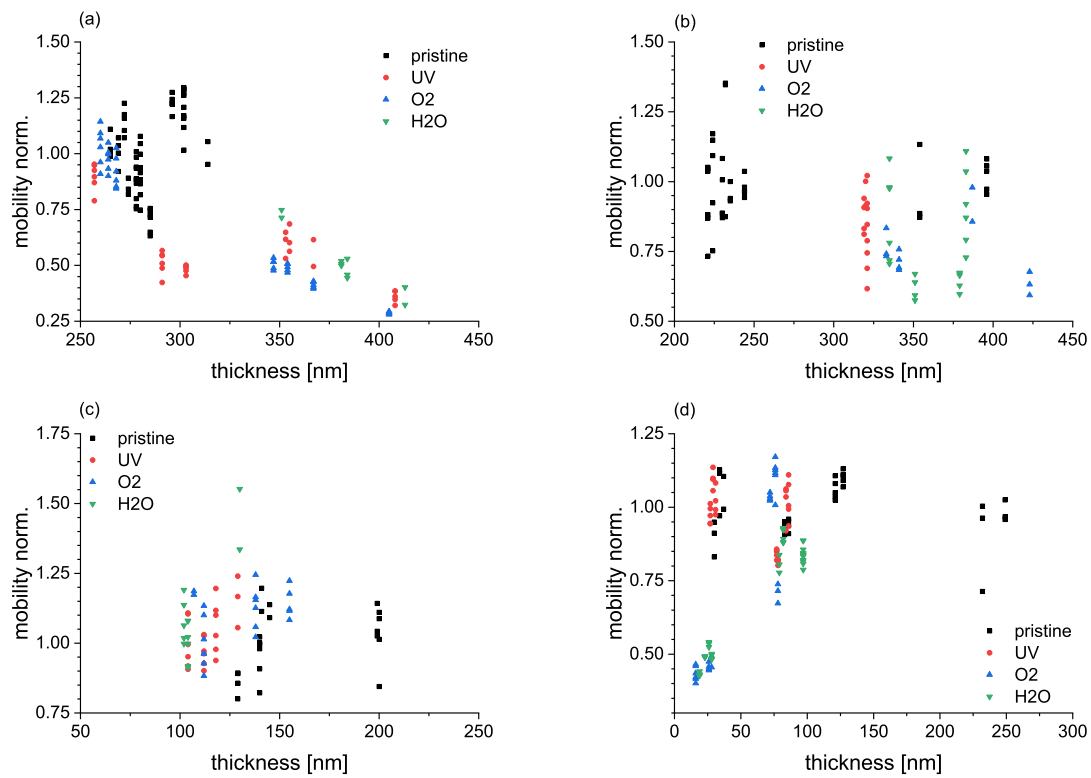


Figure 8.10: Normalized transient mobility of (a) holes and (b) electrons for pristine PCPDTBT as well as (c) holes and (d) electrons for MDMO-PPV.

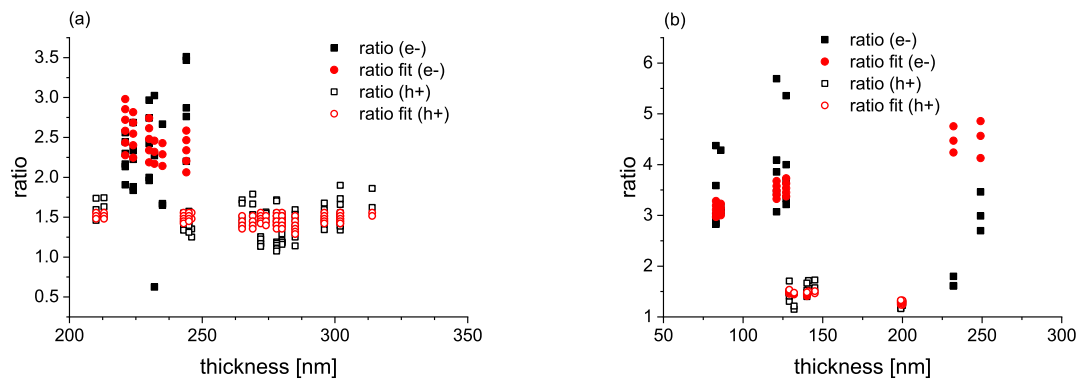


Figure 8.11: Ratio of the transient peak and steady state signals for (a) PCPDTBT and (b) MDMO-PPV SCLC devices.

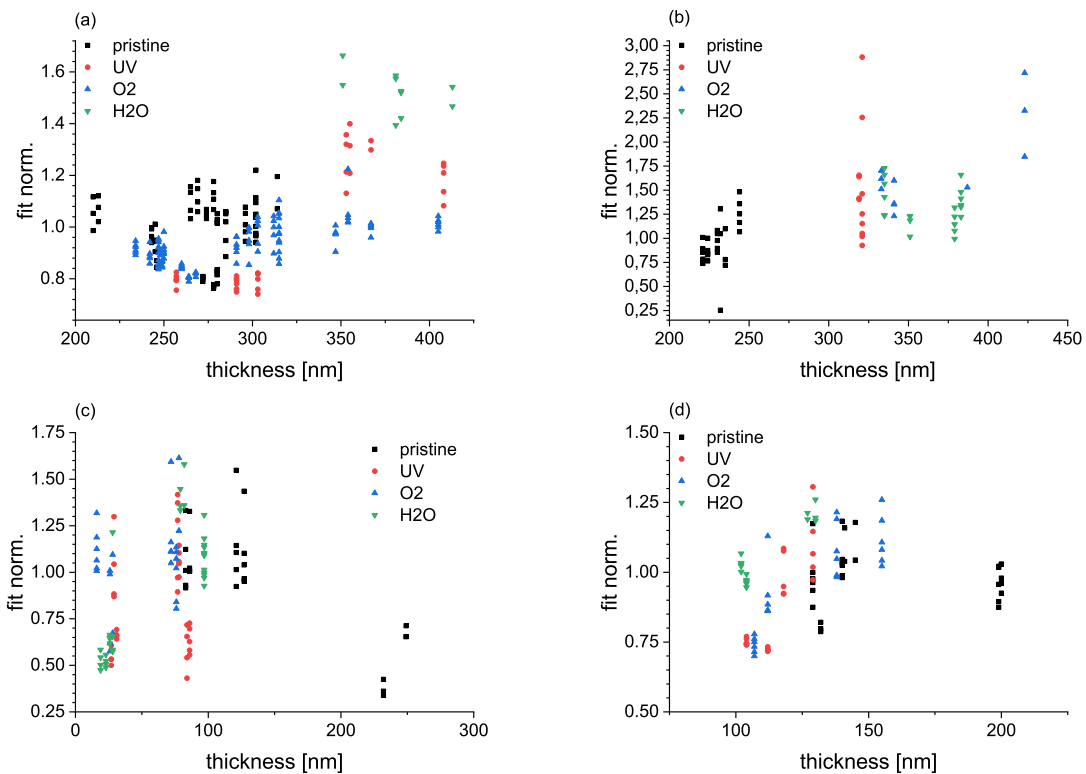


Figure 8.12: Normalized Current ratio of (a) holes and (b) electrons of pristine and aged PCPDTBT samples as well as (c) holes and (d) electrons of pristine and aged MDMO-PPV samples.

Abbreviations and variables

All abbreviations used in this thesis are listed in the following:

Ag	Silver
Al	Aluminum
Alq3	organic semiconductor (Tab. 8.3)
Bphen	organic semiconductor (Tab. 8.3)
Ca	Calcium
CV-curve	capacitance-voltage curve
DOS	density of states
FET	field effect transistor
FFT	fast Fourier transformation
HOMO	highest occupied molecular orbital
ITO	Indium Tin Oxide
IV-curve	current-voltage curve
JV-curve	current density-voltage curve
LUMO	lowest unoccupied molecular orbital
MDMO-PPV	organic semiconductor (Tab. 8.2)
MIS	metal insulator semiconductor
MIS-TSC	thermally stimulated current measurement at a MIS structure
MTDATA	organic semiconductor (Tab. 8.2)
Ni	Nickel
OLED	organic light emitting diode
op. amp.	operational amplifier
P3HT	organic semiconductor (Tab. 8.2)
PCB	printed circuit board
PCPDTBT	organic semiconductor (Tab. 8.2)
PEDOT:PSS	organic semiconductor (Tab. 8.3)
SCLC	space charge limited current
Si	Silicon
SiO ₂	Silicon Dioxide
TAPC	organic semiconductor (Tab. 8.3)
TSC	thermally stimulated current
TSDC	thermally stimulated depolarization current

Physical constants:

$\epsilon_0 = 8.854 \cdot 10^{-12} \frac{\text{As}}{\text{Vm}}$	permittivity constant
$k_B = 8.617 \cdot 10^{-5} \frac{\text{eV}}{\text{K}}$	Boltzmann constant
$q = 1.602 \cdot 10^{-19} \text{ C}$	elementary charge

All variables used in this thesis are listed in the following:

$A_{simu}, B_{simu}, C_{simu}$	parameter for fitting normalized mobility from the simulation (Chap. 3.2)
$a_{SCLC}, b_{SCLC}, c_{SCLC}$	fit variable for thickness dependent mobility fit (Chap. 6.6.3)
A	active area of a device under test
A_{amp}	amplitude of oscillating voltage for trap filling in a MIS device
a_{ramp}	slope of a linear voltage rise function
β	heating rate for TSC measurement
$c_{p,min}, c_{p,max}$	definition of allowed charge carrier density range for simulation
C	capacitance
C_{iso}	isolation capacitance of an opto coupler
C_{OSS}	output capacitance of a transistor
$C_{P,c}$	step voltage stabilizing capacitor (ceramic) (Chap. 6.3.1)
$C_{P,f}$	step voltage stabilizing capacitor (foil) (Chap. 6.3.1)
$C_{P,e}$	step voltage stabilizing capacitor (electrolyte) (Chap. 6.3.1)
C_S	step voltage stabilizing capacitor (Chap. 6.3)
C_{samp}	sample capacitance
$CMRR$	common mode rejection ratio of an op. amp.
c	a constant (e. g. from an integration)
c_{max}	coefficient maximum within the algorithm determining the coefficient (Fig. 8.2)
c_{min}	as c_{max} for the maximum
D_n	electron diffusion constant
D_p	hole diffusion constant
d	thickness of a semiconductor layer under test
d_{eff}	effective thickness of a device

γ	decay length of the wave function of a localized charge carrier
γ_n	decay length of the wave function of a localized electron
γ_p	decay length of the wave function of a localized hole
E	energy
E_a	activation Energy
E_{aff}	electron affinity
E_F	Fermi level
E_g	band gap or energetic distance between HOMO and LUMO
E_H	energetic position of the HOMO in relation to the vacuum level
E_L	energetic position of the LUMO in relation to the vacuum level
E_{tr}	effective transport energy
$E_{tr,n}$	effective transport energy of electrons
$E_{tr,p}$	effective transport energy of holes
E_{norm}	normalized energy within the Gaussian profile approximation
E'	integration variable in case integration over energy
ϵ	permittivity
ϵ_r	specific permittivity
F	electrical field
F_a	electric field at the anode
F_c	electric field at the cathode
f_{cut}	cut off frequency for FFT low pass filter (Chap. 8.5)
f_{atj}	attempt to jump frequency
$f_{atj,n}$	attempt to jump frequency for electrons
$f_{atj,p}$	attempt to jump frequency for holes
f_{fd}	Fermi-Dirac occupation probability
f_{rise}	factor between mobility with ideal and non ideal voltage step function (Chap. 6.5.5)
f_{-3dB}	3dB cut off Frequency of an op. amp.
G_a	approximation function of a Gaussian DOS
$G_{gen,n}$	generation rate of electrons
$G_{gen,p}$	generation rate of holes
$g(E)$	Gaussian profile/ DOS in dependents of the energy
$g_H(E)$	Gaussian DOS of HOMO levels
$g_L(E)$	Gaussian DOS of LUMO levels
H_a	factor within the Gaussian profile approximation (Chap. 3.1)

I	current
I_{leak}	leak current of an opto coupler
I_{load}	load current of an opto coupler
I_{max}	maximum current
I_{out}	max output current of an op. amp.
$I_{MIS-TSC,bipolar}$	bipolar MIS-TSC current
$I_{MIS-TSC,with(h+)}$	hole MIS-TSC with charging
$I_{MIS-TSC,without(h+)}$	hole MIS-TSC without charging
$I_{MIS-TSC,with(e-)}$	electron MIS-TSC with charging
$I_{MIS-TSC,without(e-)}$	electron MIS-TSC without charging
I_{TSC}	thermally stimulated current (TSC)
$I_{TSC,without}$	classical TSC of a diode without charging
$I_{TSC,with}$	classical TSC of a diode with charging
I_{TSC}	actual TSC on diode
$i(t)$	time dependent current
$i_C(t)$	charging or discharging current of a capacitance
$i_{c,s}(t)$	time dependent charging current of the sample capacitance
$i_m(t)$	time dependent current over the measuring resistance (Chap. 6.3)
$i_s(t)$	time dependent current through the sample
J	static current density
J_n	static electron current density
J_p	static hole current density
$j(t)$	time dependent current density
$j_{displ}(x, t)$	time dependent displacement current density
$j_{drift}(x, t)$	time dependent drift current density
K_a	variable within the approximation of a Gaussian profile (Chap. 3.1)
μ	charge carrier mobility
μ_n	electron mobility
μ_p	hole mobility

N	total density of states (DOS)
N_H	number of HOMO states
N_L	number of LUMO states
$N_{trap,occ}$	number of occupied trap states
n	electron density
$n_{trap,occ}$	density of occupied trap states
η	charge carrier density (electrons or holes)
ω	angular frequency
P_{max}	maximum power
$PSRR$	power supply rejection ratio of an op. amp.
p	hole density
Ψ_S	surface potential
φ	space charge density
Ψ	electric potential
Q	electrical charge
Q_G	gate charge of a transistor
R_{50}	Resistor used for 20V to 50V step (Chap. 6.3.1)
R_1	resistance 1 for amplification circuit (Chap. 6.3.3)
R_2	resistance 2 for amplification circuit (Chap. 6.3.3)
R_{dch1}	decharging resistor for puls capacitors (Chap. 6.3)
R_{dch2}	decharging sample after measurement (Chap. 6.3.2)
R_{in}	input resistance of an op. amp.
R_{iso}	isolation resistance of an opto coupler
R_m	measuring resistance in SCLC circuit (Chap. 6.3)
R_{osci}	Resistor for voltage step control (Chap. 6.3.1)
R_{ON}	resistance in on state of a transistor
$R_{rec,n}$	recombination rate of electrons
$R_{rec,p}$	recombination rate of holes
R_p	parallel resistance to the sample
R_s	serial resistance to the sample
R_{sample}	estimated device resistance
R_{step}	Resistor for voltage step control (Chap. 6.3.1)
ρ_{res}	specific resistance

Q_{max}	maximum charge
$Q_{max,MIS}$	maximum charge in a MIS device
$q_{area}(t)$	area dependent charge
$q_C(t)$	time dependent charge of a capacitance
s_{norm}	normalized Gaussian width within the approximation of a Gaussian profile (Chap. 3.1)
σ	width of Gaussian profile
σ_c	specific conductivity
σ_H	width of the Gaussian DOS (HOMO)
σ_L	width of the Gaussian DOS (LUMO)
T	temperature
T_1	start temperature of fractional TSC measurement step
T_2	maximum temperature of fractional TSC measurement step
T_3	end temperature of fractional TSC measurement step
T_{high}	highest temperature during TSC measurement
T_{low}	lowest temperature during TSC measurement
t	time
Δt_{FFT}	time range for FFT low pass filter (Chap. 8.5)
Δt_1	time prior to heating
Δt_2	time prior to cooling
Δt_{f1}	start waiting time of fractional TSC measurement step
Δt_{f2}	waiting time of fractional TSC measurement step at maximum temperature
Δt_{f3}	end waiting time of fractional TSC measurement step
t_{corr}	correction for the transit time (Chap. 6.5.5)
t_{ON}	turn on time of a transistor
t_{RC}	RC time constant
t_{rise}	time to reach the maximum voltage of a step function (Chap. 3.2)
t_{settle}	settling time of an op. amp.
t_{slew}	slew rate of an op. amp.
t_{trans}	transit time for first charge carriers for transient SCLC
τ_e	RC time constant for extracting charge carriers (TSC measurement)
τ_i	RC time constant for injecting charge carriers (TSC measurement)

V	voltage
V_{b-in}	build in voltage of a device
$V_{c,aver}$	average voltage of the capacitor between $t = 0$ and t_{trans}
V_{ch}	charging voltage for TSC method (constant)
V_{DS}	drain source voltage of a transistor
V_{GS}	gate source voltage of a transistor
V_{load}	load voltage of an opto coupler
V_{max}	maximum voltage
V_S	step voltage in SCLC circuit (Chap. 6.3)
V_{supply}	supply voltage of an op. amp.
V_{th}	threshold voltage of a transistor
V_{vol}	volume of a device under test
V_{zener}	Zener voltage of a Zener diode
$v(t)$	time dependent voltage
$v_0(t)$	externally applied time dependent voltage
$v_1(t)$	time dependent voltage over the device
$v_2(t)$	time dependent voltage over the device serial resistance
$v_{ampl}(t)$	time dependent amplified voltage, measured by the oscilloscope (Chap. 6.3.3)
$v_C(t)$	time dependent voltage of a capacitance
$v_{ch}(t)$	charging voltage for TSC method (oscillating)
v_{drift}	drift velocity
$v_m(t)$	time dependent voltage over measuring resistance (Chap. 6.3.3)
W	work function
Z_M	Zener Diode of the voltage step generation (SCLC circuit) (Chap. 6.3.1)
Z_S	Zener Diode of the amplification circuit (SCLC circuit) (Chap. 6.3.3)
z	slope of a double logarithmic plot of steady state SCLC (Chap. 2.3.1)

List of Figures

2.1	Schematic timing diagram of the enveloping TSC measurement sequence.	10
2.2	Schematic timing diagram of the fractional TSC measurement sequence .	12
2.3	Ideal SCLC JV curve	16
2.4	Ideal (depth dependent) electric field and hole concentration for steady state SCLC	16
2.5	Ideal time dependent current signal for transient SCLC	19
2.6	Time dependent electrical field and hole concentration (depth dependent) for ideal transient SCLC	20
3.1	Schematic presentation of non-ideal parameters analyzed with the simulation.	28
4.1	Sample layout for SCLC devices	32
4.2	Hole only devices (SCLC) and MTDATA energy alignments for hole only the device	33
4.3	Side view of the electron only SCLC device structure. The thickness of the organic semiconductor varies between 25 nm and 500 nm.	33
4.4	Produced SCLC samples for investigating the polymers	34
4.5	Samples layout for MIS TSC measurements	36
5.1	Setup for the TSC measurements.	42
6.1	Schematic timing diagram of the MIS-TSC measurement	46
6.2	MIS-TSC measurement of a Al/n-Si/SiO ₂ /Ag device	49
6.3	Classical TSC and MIS-TSC measurement of P3HT	50
6.4	Voltage dependent capacitance of MIS device	52
6.5	Fractional MIS-TSC measurement of P3HT for benchmarking purpose . .	53
6.6	Energetic trap distribution and determination method for P3HT (benchmark)	54

6.7	Charging voltage dependence and stability of the MIS-TSC method	56
6.8	Effect of oscillating charging voltage for the MIS-TSC method	57
6.9	Simplified transient SCLC measurement circuit	59
6.10	Picture of the transient SCLC measurement setup. The oscilloscope is the model UTD2052 from UNI-Trend.	60
6.11	Circuit part: Voltage step generation of the circuit shown in figure 6.9 . .	61
6.12	Circuit part: Device connection in the circuit shown in figure 6.9	61
6.13	Circuit part: current measurement in the circuit shown in figure 6.9 . . .	63
6.14	JV curves of MTDATA hole only devices with different film thicknesses of MTDATA in double logarithmic plot	65
6.15	Transient SCLC signal with oscillation	66
6.16	Oscillation correction for transient SCLC signals	67
6.17	Thickness dependent mobility from transient SCLC of MTDATA	69
6.18	Measurement limits of the transient SCLC circuit	70
6.19	Simulation: normalized transient and steady state mobility of the basic device	72
6.20	Simulation: depth dependent charge carrier density	73
6.21	Simulation: Influence of attempt to jump frequency and electric field strength	73
6.22	Simulation: Influence of doping	74
6.23	Simulation: Influence of built-in field	76
6.24	Simulation: Influence of Injection barrier	77
6.25	Simulation: Influence of voltage rise time	78
6.26	Simulation: Influence of serial resistance	80
6.27	Comparison of electron and hole mobility	83
6.28	Enveloping MIS-TSC measurement of pristine and aged P3HT. The shift of the electron peaks of aged P3HT may be caused by retrapping, as additional shallow trap levels are introduced by the aging.	85
6.29	Distribution of hole trap states of pristine and aged polymers	86
6.30	Distribution of hole and electron trap states of pristine and aged PCPDTBT	88
6.31	Mobility of holes and electrons for pristine and aged P3HT	90
6.32	Normalized transient mobility of holes and electrons for pristine and aged P3HT	92
6.33	Ratio of the transient peak and steady state signals for P3HT devices. . .	92

6.34	Normalized Current ratio of holes and electrons for pristine and aged P3HT samples	93
6.35	Normalized hole mobility and absolute ratio between peak and steady state current	93
6.36	Normalized electron mobility and absolute ratio between peak and steady state current	93
8.1	Substrate and device structure	103
8.2	Algorithm used for fitting curves.	117
8.3	PCB: red lines are top wiring and blue are bottom wiring; all devices are on the top side and described in table 8.10	119
8.4	Complete circuit of the PCB, all devices are described in table 8.10.	120
8.5	Control circuit for the circuit shown in figure 8.3 with all resistance values in $k\Omega$	124
8.6	Enveloping MIS-TSC measurements of pristine/ aged PCPDTBT and MDMO-PPV	125
8.7	Enveloping and fractional MIS-TSC measurements of polymers (pristine and UV light treated)	126
8.8	Enveloping and fractional MIS-TSC measurements of polymers (oxygen and water treated)	127
8.9	Transient and steady state mobility of PCPDTBT and MDMO-PPV	129
8.10	Normalized transient mobility of pristine PCPDTBT and MDMO-PPV	130
8.11	Ratio of the transient peak and steady state signals for PCPDTBT and MDMO-PPV	130
8.12	Normalized Current ratio of of pristine/ aged PCPDTBT and MDMO-PPV	131

List of Tables

2.1	Proposed universal traps (by literature)	8
3.1	Characteristic values of the simulated basic device.	27
4.1	Spincoating parameters for thick layers of P3HT and PCPDTBT used for SCLC samples.	37
4.2	Spincoating parameters for thick layers of MDMO-PPV used for SCLC samples.	38
4.3	Evaporation parameters of metals and small molecules.	38
4.4	Aging processes for the polymers (P3HT, PCPDTBT, MDMO-PPV). . .	39
5.1	Parameters for TSC measurements as they are described in chapter 2.2. .	43
6.1	Current range for all amplifications of the transient SCLC circuit.	64
8.1	Variables used in this chapter.	101
8.2	Materials under examination	104
8.3	Organic contact materials	105
8.4	Cleaning process for substrates	106
8.5	Spin coater Prozess for PEDOT:PSS	106
8.6	Spin coater Prozess for P3HT and PCPDTBT	107
8.7	Spin coating process for MDMO-PPV	107
8.8	results for fit parameters	108
8.9	Calibration of the SCLC measurement circuit	118
8.10	Description of all elements used in the SCLC measurement circuit	121
8.10	continued	122
8.11	Mobility fit values for equation 6.17.	128
8.12	Ratio fit values for equation 6.17.	128

Bibliography

- [1] M. Abkowitz, J. S. Facci, and M. Stolka. “Time-resolved space charge-limited injection in a trap-free glassy polymer”. In: *Chemical Physics* 177.3 (1993), pp. 783–792.
- [2] C. Adachi, R. Kwong, and S. R. Forrest. “Efficient electrophosphorescence using a doped ambipolar conductive molecular organic thin film”. In: *Organic Electronics: physics, materials, applications* 2.1 (2001), pp. 37–43.
- [3] V. I. Adamovich, S. R. Cordero, P. I. Djurovich, A. Tamayo, M. E. Thompson, B. W. D’Andrade, and S. R. Forrest. “New charge-carrier blocking materials for high efficiency OLEDs”. In: *Organic Electronics* 4.2-3 (2003), pp. 77–87.
- [4] R. Agrawal, P. Kumar, S. Ghosh, and A. K. Mahapatro. “Thickness dependence of space charge limited current and injection limited current in organic molecular semiconductors”. In: *Applied Physics Letters* 93.7 (2008), p. 073311.
- [5] M. Ahles, R. Schmechel, and H. Von Seggern. “N-type organic field-effect transistor based on interface-doped pentacene”. In: *Applied Physics Letters* 85.19 (2004), pp. 4499–4501.
- [6] M. Al-Ibrahim, A. Konkin, H. Roth, D. A. M. Egbe, E. Klemm, U. Zhokhavets, G. Gobsch, and S. Sensfuss. “Phenylene-ethynylene/phenylene-vinylene hybrid polymers: Optical and electrochemical characterization, comparison with poly[2-methoxy-5-(3',7'-dimethyloctyloxy)-1,4-phenylene vinylene] and application in flexible polymer solar cells”. In: *Thin Solid Films* 474.1-2 (2005), pp. 201–210.
- [7] I. V. Arkhipov, P. Heremans, E. V. Emelianova, G. J. Adriaenssens, and H. Bässler. “Weak-field carrier hopping in disordered organic semiconductors: The effects of deep traps and partly filled density-of-states distribution”. In: *Journal of Physics Condensed Matter* 14.42 (2002), pp. 9899–9911.

- [8] V. I. Arkhipov, E. V. Emelianova, and G. J. Adriaenssens. “Effective transport energy versus the energy of most probable jumps in disordered hopping systems”. In: *Physical Review B - Condensed Matter and Materials Physics* 64.12 (2001), p. 125125.
- [9] V. I. Arkhipov, H. Von Seggern, and E. V. Emelianova. “Charge injection versus space-charge-limited current in organic light-emitting diodes”. In: *Applied Physics Letters* 83.24 (2003), pp. 5074–5076.
- [10] V. I. Arkhipov, P. Heremans, E. V. Emelianova, G. J. Adriaenssens, and H. Bässler. “Charge carrier mobility in doped disordered organic semiconductors”. In: *Journal of Non-Crystalline Solids* 338-340.1 SPEC. ISS. (2004), pp. 603–606.
- [11] V. I. Arkhipov, P. Heremans, E. V. Emelianova, G. J. Adriaenssens, and H. Bässler. “Charge carrier mobility in doped semiconducting polymers”. In: *Applied Physics Letters* 82.19 (2003), pp. 3245–3247.
- [12] V. I. Arkhipov, P. Heremans, E. V. Emelianova, and H. Bässler. “Effect of doping on the density-of-states distribution and carrier hopping in disordered organic semiconductors”. In: *Physical Review B - Condensed Matter and Materials Physics* 71.4 (2005), p. 045214.
- [13] V. I. Arkhipov, P. Heremans, E. V. Emelianova, and G. J. Adriaenssens. “Space-charge-limited currents in materials with Gaussian energy distributions of localized states”. In: *Applied Physics Letters* 79.25 (2001), pp. 4154–4156.
- [14] V. I. Arkhipov, E. V. Emelianova, R. Schmechel, and H. Von Seggern. “Thermally stimulated luminescence versus thermally stimulated current in organic semiconductors”. In: *Journal of Non-Crystalline Solids* 338-340.1 SPEC. ISS. (2004), pp. 626–629.
- [15] V. Arkhipov, P. Heremans, E. Emelianova, and H. Bässler. “Effect of doping on the density-of-states distribution and carrier hopping in disordered organic semiconductors”. In: *Physical Review B* 4.71 (2005), p. 045214.
- [16] S. Ashizawa, R. Horikawa, and H. Okuzaki. “Effects of solvent on carrier transport in poly(3,4-ethylenedioxythiophene)/poly(4-styrenesulfonate)”. In: *Synthetic Metals* 153.1-3 (2005), pp. 5–8.
- [17] S. Baranovskii and M. Zhu. “Thermally stimulated conductivity in disordered semiconductors at low temperatures”. In: *Physical Review B - Condensed Matter and Materials Physics* 55.24 (1997), pp. 16226–16232.

- [18] S. D. Baranovskii. “Theoretical description of charge transport in disordered organic semiconductors”. In: *Physica Status Solidi (B) Basic Research* 251.3 (2014), pp. 487–525.
- [19] M. V. Basilevsky, A. V. Odinkov, and K. G. Komarova. “Charge-Transfer Mobility Parameters in Photoelectronic Devices: The Advanced Miller-Abrahams Computation”. In: *Journal of Physical Chemistry B* 119.24 (2015), pp. 7430–7438.
- [20] N. Benson, A. Gassmann, E. Mankel, T. Mayer, C. Melzer, R. Schmechel, and H. Von Seggern. “The role of Ca traces in the passivation of silicon dioxide dielectrics for electron transport in pentacene organic field effect transistors”. In: *Journal of Applied Physics* 104.5 (2008), p. 054505.
- [21] G. Bhattarai, A. N. Caruso, and M. M. Paquette. “Steady-state space-charge-limited current analysis of mobility with negative electric field dependence”. In: *Journal of Applied Physics* 124.4 (2018), p. 045701.
- [22] J. C. Blakesley, F. A. Castro, W. Kylberg, G. F. Dibb, C. Arantes, R. Valaski, M. Cremona, J. S. Kim, and J.-S. Kim. “Towards reliable charge-mobility benchmark measurements for organic semiconductors”. In: *Organic Electronics* 15.6 (2014), pp. 1263–1272.
- [23] P. W. M. Blom, M. J. M. De Jong, and S. Breedijk. “Temperature dependent electron-hole recombination in polymer light-emitting diodes”. In: *Applied Physics Letters* 71.7 (1997), pp. 930–932.
- [24] P. Blood and J. W. Orton. “The electrical characterisation of semiconductors”. In: *Reports on Progress in Physics* 41.2 (1978), pp. 157–257.
- [25] L. Bozano, S. A. Carter, J. C. Scott, G. G. Malliaras, and P. J. Brock. “Temperature- and field-dependent electron and hole mobilities in polymer light-emitting diodes”. In: *Applied Physics Letters* 74.8 (1999), pp. 1132–1134.
- [26] W. Brütting and C. Adachi, eds. *Physics of Organic Semiconductors*. Academic Press, 1970.
- [27] L. Chen, G. Dong, L. Duan, J. Qiao, D. Zhang, L. Wang, and Y. Qiu. “Positional disorder-induced mobility enhancement in rapidly cooled organic semiconductor melts”. In: *Journal of Physical Chemistry C* 114.19 (2010), pp. 9056–9061.

- [28] T. Chiba, K. Nakayama, Y. Pu, T. Nishina, M. Yokoyama, and J. Kido. “Hole mobility measurement of 4,4’-Bis[N-(1-naphthyl)-N-phenylamino]- biphenyl by dark injection method”. In: *Chemical Physics Letters* 502.1-3 (2011), pp. 118–120.
- [29] Z. Chiguvare and V. Dyakonov. “Trap-limited hole mobility in semiconducting poly(3-hexylthiophene)”. In: *Physical Review B - Condensed Matter and Materials Physics* 70.23 (2004), p. 235207.
- [30] L. Chua, J. Zaumseil, J. Chang, E. C. Ou, P. K. Ho, H. Sirringhaus, and R. H. Friend. “General observation of n-type field-effect behaviour in organic semiconductors”. In: *Nature* 434.7030 (2005), pp. 194–199.
- [31] R. Coehoorn and P. A. Bobbert. “Effects of Gaussian disorder on charge carrier transport and recombination in organic semiconductors”. In: *Physica Status Solidi (A) Applications and Materials Science* 209.12 (2012), pp. 2354–2377.
- [32] J. W. Cooley and J. W. Tukey. “An algorithm for the machine calculation of complex fourier series”. In: *Mathematics of Computation* 19.90 (1965), pp. 249–259.
- [33] T. A. T. Cowell and J. Woods. “The evaluation of thermally stimulated current curves”. In: *British Journal of Applied Physics* 18.8 (1967), pp. 1045–1051.
- [34] X. Crispin, S. Marciniak, W. Osikowicz, G. Zotti, A. W. Denier Van Der Gon, F. Louwet, M. Fahlman, L. Groenendaal, F. De Schryver, and W. R. Salaneck. “Conductivity, morphology, interfacial chemistry, and stability of poly(3,4-ethylene dioxythiophene)-poly(styrene sulfonate): A photoelectron spectroscopy study”. In: *Journal of Polymer Science, Part B: Polymer Physics* 41.21 (2003), pp. 2561–2583.
- [35] *data sheet: Aluminum Electrolytic Capacitors/ FK*. 1st ed. Panasonic Corporation. Winsbergring 15 22525 Hamburg Germany, Nov. 2012.
- [36] *data sheet: Anti-Surge Thick Film Chip Resistors 0603, 0805, 1206, 1210*. Panasonic Corporation. Winsbergring 15 22525 Hamburg Germany, June 2014.
- [37] *data sheet: Board to Cable Lock Connector*. Hirose Electric CO., LTD. 6-3 Nakagawa Chuoh-2-ChomeTsuzuki-Ku Yokohama-Shi 224-8540 Japan, Apr. 2013.
- [38] *data sheet: Ceramic Capacitors Middle and High Voltage*. 1.1. Farnell GmbH. Karl-Hammerschmidt-Str. 38 85609 Aschheim Germany, Feb. 2012.

- [39] *data sheet: Chip Resistors Pulse Withstanding*. 1st ed. Farnell GmbH. Karl-Hammerschmidt-Str. 38 85609 Aschheim Germany, June 2013.
- [40] *data sheet: Clevios HIL-E 100*. 81108992nd ed. Heraeus Deutschland GmbH & Co. KG. 51368 CHEMPARK Leverkusen Germany, May 2016.
- [41] *data sheet: electrically conductive, silver epoxy EPO-TEK H21D*. Epoxy Technology, Inc. 14 Fortune Drive Billerica MA USA, Apr. 2014.
- [42] *data sheet: GENERAL PURPOSE CHIP RESISTORS RC1206*. 4th ed. Yageo Corporation. 3F 233-1 Baoqiao Rd. Xindian Dist. New Taipei City 23145 Taiwan, July 2009.
- [43] *data sheet: GU-E PhotoMOS (AQY21 EH)*. Panasonic Corporation. Winsbergring 15 22525 Hamburg Germany, Dec. 2006.
- [44] *data sheet: HEXFET Power MOSFET PD-95015A*. International Rectifier. 233 Kansas St. El Segundo, California 90245 USA, Dec. 2004.
- [45] *data sheet LM6171: High Speed Low Power Low Distortion Voltage Feedback Amplifier*. SNOS745C. Texas Instruments. Post Office Box 655303 Dallas Texas 75265, Mar. 2013.
- [46] *data sheet: N-channel TrenchMOS logic level FET BUK9277-55A*. 1st ed. NXP Semiconductors B.V. High Tech Campus 60 Eindhoven Netherlands, June 2014.
- [47] *data sheet: Power MOSFET NTGD3148N*. NTGD3148N/D. ON Semiconductor Components Industries, LLC. Japan Customer Focus Center 2-9-1 Kamimeguro Meguro-ku Tokyo Japan, Apr. 2008.
- [48] *data sheet: resistors RK73H*. KOA Speer Electronics, Inc. 199 Bolivar Drive Bradford PA 16701 USA, Nov. 2016.
- [49] *data sheet: resistors WK73*. KOA Speer Electronics, Inc. 199 Bolivar Drive Bradford PA 16701 USA, Oct. 2015.
- [50] *data sheet: Series 204 SMD DIP Switch*. CTS Corporation. Unit 16 Third Road Blantyre Industrial Est. Glasgow Scotland G72 0XA, June 2014.
- [51] *data sheet: Single Zener diodes BZX84J series*. 2nd ed. NXP Semiconductors B.V. High Tech Campus 60 Eindhoven Netherlands, July 2011.
- [52] *data sheet: Stacked Metallized PPS Film Chip Capacitor ECHU(X)*. Panasonic Corporation. Winsbergring 15 22525 Hamburg Germany, Feb. 2016.

- [53] *data sheet: Standard Thick Film Chip Resistors D/CRCW e3*. 20035th ed. Vishay Intertechnology, Inc. 63 Lancaster Avenue Malvern PA 19355-2143 England, June 2012.
- [54] *data sheet: Surface Mount Multilayer Ceramic Chip Capacitors (SMD MLCCs)*. KEMET Electronics Corporation. P.O. Box 5928 Greenville SC 29606 USA, Sept. 2017.
- [55] *data sheet: Thick Film Chip Resistor1206*. 1st ed. Farnell GmbH. Karl-Hammerschmidt-Str. 38 85609 Aschheim Germany, July 2013.
- [56] *data sheet: Thick Film High Power Chip Resistors Size 2512 2W, 2010 1W, 1206 1/2W*. ASC_WF25-20-12P_V10. PSA Walsin Technology Corporation. 24F. No.1 Songzhi Rd. Xinyi Dist Taipei City 110 Taiwan, July 2011.
- [57] *data sheet: TPS Series, low EPR*. AVX Corporation. One AVX Boulevard Fountain Inn SC 29644 USA.
- [58] *data sheet: UV LED 260019 SERIES*. 30/99 Issue 02. Marl International Limited. Marl Business Park, Ulverston, Cumbria LA12 9BN, 2000.
- [59] P. S. Davids, I. H. Campbell, and D. L. Smith. “Device model for single carrier organic diodes”. In: *Journal of Applied Physics* 82.12 (1997), pp. 6319–6325.
- [60] A. B. Djurišić, T. W. Lau, L. S. M. Lam, and W. K. Chan. “Influence of atmospheric exposure of tris (8-hydroxyquinoline) aluminum (Alq3): A photoluminescence and absorption study”. In: *Applied Physics A: Materials Science and Processing* 78.3 (2004), pp. 375–380.
- [61] A. W. Dweydari and C. H. B. Mee. “Work function measurements on (100) and (110) surfaces of silver”. In: *physica status solidi (a)* 27.1 (1975), pp. 223–230.
- [62] T. Esward, S. Knox, H. Jones, P. Brewer, C. Murphy, L. Wright, and J. Williams. “A metrology perspective on the dark injection transient current method for charge mobility determination in organic semiconductors”. In: *Journal of Applied Physics* 109.9 (2011), p. 093707.
- [63] P. O. Fagerström and H. G. Grimmeiss. “TSC measurements and their correlation with photocurrent techniques”. In: *Solid State Communications* 26.4 (1978), pp. 261–263.
- [64] J. Feng, T. Okamoto, J. Simonen, and S. Kawata. “Color-tunable electroluminescence from white organic light-emitting devices through coupled surface plasmons”. In: *Applied Physics Letters* 90.8 (2007), p. 081106.

- [65] R. H. Friend, R. W. Gymer, A. B. Holmes, J. H. Burroughes, R. N. Marks, C. Taliani, D. D. C. Bradley, D. A. Dos Santos, J. L. Brédas, M. Lögdlund, and W. R. Salaneck. “Electroluminescence in conjugated polymers”. In: *Nature* 397.6715 (1999), pp. 121–128.
- [66] A. Girlando, M. Masino, G. Visentini, R. G. Della Valle, A. Brillante, and E. Venuti. “Lattice dynamics and electron-phonon coupling in the β -(BEDT-TTF)₂I₃ organic superconductor”. In: *Physical Review B - Condensed Matter and Materials Physics* 62.21 (2000), pp. 14476–14486.
- [67] D. M. Goldie. “Transient space-charge-limited current pulse shapes in molecularly doped polymers”. In: *Journal of Physics D: Applied Physics* 32.23 (1999), pp. 3058–3067.
- [68] G. Griffini, S. Turri, and M. Levi. “Degradation and stabilization of poly(3-hexylthiophene) thin films for photovoltaic applications”. In: *Polymer Bulletin* 66.2 (2011), pp. 211–222.
- [69] M. Grifoni and P. Hänggi. “Driven quantum tunneling”. In: *Physics Reports* 304.5 (1998), pp. 229–354.
- [70] Y. Gu, C. Wang, and T. P. Russell. “Multi-length-scale morphologies in PCPDTBT/PCBM bulk-heterojunction solar cells”. In: *Advanced Energy Materials* 2.6 (2012), pp. 683–690.
- [71] Z. Guan, J. B. Kim, H. Wang, C. Jaye, D. A. Fischer, Y. Loo, and A. Kahn. “Direct determination of the electronic structure of the poly(3-hexylthiophene):phenyl-[6,6]-C₆₁ butyric acid methyl ester blend”. In: *Organic Electronics: physics, materials, applications* 11.11 (2010), pp. 1779–1785.
- [72] B. Gündüz. “Optical properties of poly[2-methoxy-5-(3’,7’-dimethyloctyloxy)-1,4-phenylenevinylene] light-emitting polymer solutions: effects of molarities and solvents”. In: *Polymer Bulletin* 72.12 (2015), pp. 3241–3267.
- [73] R. R. Haering and E. N. Adams. “Theory and application of thermally stimulated currents in photoconductors”. In: *Physical Review* 117.2 (1960), pp. 451–454.
- [74] D. B. Hall, P. Underhill, and J. M. Torkelson. “Spin coating of thin and ultrathin polymer films”. In: *Polymer Engineering & Science* 38.12 (1998), pp. 2039–2045.
- [75] H. F. Haneef, A. M. Zeidell, and O. D. Jurchescu. “Charge carrier traps in organic semiconductors: a review on the underlying physics and impact on electronic devices”. In: *J. Mater. Chem. C* 8 (3 2020), pp. 759–787.

- [76] T. Hasegawa and J. Takeya. “Organic field-effect transistors using single crystals”. In: *Science and Technology of Advanced Materials* 10.2 (2009), p. 024314.
- [77] S. K. Hau, H. Yip, J. Zou, and A. K. Jen. “Indium tin oxide-free semi-transparent inverted polymer solar cells using conducting polymer as both bottom and top electrodes”. In: *Organic Electronics* 10.7 (2009), pp. 1401–1407.
- [78] A. Hepp, N. Von Malm, R. Schmechel, and H. Von Seggern. “Effects of process parameters on trap distributions in organic semiconductors”. In: *Synthetic Metals* 138.1-2 (2003), pp. 201–207.
- [79] J. Huijsing. *Operational Amplifiers, Theory and Design*. Springer Science Business Media B.V., 2011.
- [80] C. Hung and Y. Lin. “Surface properties of SiO₂ with and without H₂O₂ treatment as gate dielectrics for pentacene thin-film transistor applications”. In: *Chemical Physics Letters* 691 (2018), pp. 141–145.
- [81] M. Iwamoto and D. Taguchi. “Research trend in thermally stimulated current method for development of materials and devices in Japan”. In: *Japan Journal of Applied Physics*. 57 (2018), 03EA04.
- [82] I. Jurić and E. Tutiš. “Dark injection transient spectroscopy and density of states in amorphous organics”. In: *Organic Electronics: physics, materials, applications* 15.1 (2014), pp. 226–239.
- [83] A. Kadashchuk, Y. Skryshevskii, A. Vakhnin, N. Ostapenko, V. I. Arkhipov, E. V. Emelianova, and H. Bässler. “Thermally stimulated photoluminescence in disordered organic materials”. In: *Physical Review B - Condensed Matter and Materials Physics* 63.11 (2001), p. 115205.
- [84] S. Karg, J. Steiger, and H. Von Seggern. “Determination of trap energies in Alq₃ and TPD”. In: *Synthetic Metals* 111 (2000), pp. 277–280.
- [85] S. Khadir, M. Chakaroun, A. Belkhir, A. Fischer, O. Lamrous, and A. Boudrioua. “Localized surface plasmon enhanced emission of organic light emitting diode coupled to DBRcathode microcavity by using silver nanoclusters”. In: *Optics Express* 23.18 (2015), pp. 23647–23659.
- [86] M. Kielar, M. Daanoune, O. François-Martin, B. Flament, O. Dhez, A. K. Pandey, S. Chambon, R. Clerc, and L. Hirsch. “Insights into the Failure Mechanisms of Organic Photodetectors”. In: *Advanced Electronic Materials* 4.2 (2018), p. 1700526.

- [87] J. Kim, M. H. Yun, G. Kim, J. Lee, S. M. Lee, S. Ko, Y. Kim, G. K. Dutta, M. Moon, S. Y. Park, D. S. Kim, J. Y. Kim, and C. Yang. “Synthesis of PCDTBT-based fluorinated polymers for high open-circuit voltage in organic photovoltaics: Towards an understanding of relationships between polymer energy levels engineering and ideal morphology control”. In: *ACS Applied Materials and Interfaces* 6.10 (2014), pp. 7523–7534.
- [88] A. Köhler. “Organic semiconductors: No more breaks for electrons”. In: *Nature Materials* 11.10 (2012), pp. 836–837.
- [89] A. Kokil, K. Yang, and J. Kumar. “Techniques for characterization of charge carrier mobility in organic semiconductors”. English. In: *Journal of Polymer Science, Part B: Polymer Physics* 50.15 (2012), pp. 1130–1144.
- [90] M. Kuik, G. A. H. Wetzelaer, H. T. Nicolai, N. I. Craciun, D. M. De Leeuw, and P. W. M. Blom. “25th anniversary article: Charge transport and recombination in polymer light-emitting diodes”. In: *Advanced Materials* 26.4 (2014), pp. 512–531.
- [91] S. Kumar, D. C. Tripathi, and Y. N. Mohapatra. “Organic doped/undoped interface based diode structure: Distinct mechanisms underlying forward and reverse bias”. In: *Organic Electronics* 50 (2017), pp. 331–338.
- [92] M. A. Lampert and P. Mark. *Current Injection In Solids*. Ed. by H. G. Booker and N. DeClaris. Academic Press, 1970.
- [93] C. Laurent. “Charge dynamics in polymeric materials and its relation to electrical ageing”. In: *Annual Report - Conference on Electrical Insulation and Dielectric Phenomena, CEIDP*. 2012, pp. 1–20.
- [94] M. H. Lean and W. L. Chu. “Simulation of charge packet formation in layered polymer film”. In: *COMPEL - The International Journal for Computation and Mathematics in Electrical and Electronic Engineering* 33.4 (2014), pp. 1396–1415.
- [95] H. K. Lee, K. K. Chan, and S. So. “Role of electron blocking and trapping layers in transport characterization of a photovoltaic polymer poly(3-hexylthiophene)”. In: *Organic Electronics* 13.4 (2012), pp. 541–544.
- [96] J. U. Lee, Y. D. Kim, J. W. Jo, J. P. Kim, and W. H. Jo. “Efficiency enhancement of P3HT/PCBM bulk heterojunction solar cells by attaching zinc phthalocyanine to the chain-end of P3HT”. In: *Journal of Materials Chemistry* 21.43 (2011), pp. 17209–17218.

- [97] C. Li, M. Schwab, Y. Zhao, L. Chen, I. Bruder, I. Münster, P. Erk, and K. Müllen. “A phenanthroline derivative as exciton blocking material for organic solar cells”. In: *Dyes and Pigments* 97.1 (2013), pp. 258–261.
- [98] Y. Li. “Molecular design of photovoltaic materials for polymer solar cells: Toward suitable electronic energy levels and broad absorption”. In: *Accounts of Chemical Research* 45.5 (2012), pp. 723–733.
- [99] I. Lim, H. T. Bui, Y. S. Chan, N. K. Shrestha, C. Bathula, T. Lee, Y. Noh, and S. Han. “Study of PEDOT and analogous polymer film as back-electron injection barrier and electrical charge storing materials”. In: *RSC Advances* 211 (2017), pp. 1–4.
- [100] C. Liu, K. Wang, X. Gong, and A. J. Heeger. “Low bandgap semiconducting polymers for polymeric photovoltaics”. In: *Chemical Society Reviews* 45.17 (2016), pp. 4825–4846.
- [101] M. Manceau, A. Rivaton, J. Gardette, S. Guillerez, and N. Lemaître. “The mechanism of photo- and thermooxidation of poly(3-hexylthiophene) (P3HT) reconsidered”. In: *Polymer Degradation and Stability* 94.6 (2009), pp. 898–907.
- [102] M. M. Mandoc, B. de Boer, G. Paasch, and P. W. M. Blom. “Trap-limited electron transport in disordered semiconducting polymers”. In: *Phys. Rev. B* 75 (19 2007), p. 193202.
- [103] A. Many and G. Rakavy. “Theory of Transient Space-Charge-Limited Currents in Solids in the Presence of Trapping”. In: *Phys. Rev.* 126 (6 1962), pp. 1980–1988.
- [104] H. B. Michaelson. “Relation Between an Atomic Electronegativity Scale and the Work Function”. In: *IBM Journal of Research and Development* 22.1 (1978), pp. 72–80.
- [105] N. A. Minder, S. Ono, Z. Chen, A. Facchetti, and A. F. Morpurgo. “Band-Like Electron Transport in Organic Transistors and Implication of the Molecular Structure for Performance Optimization”. In: *Advanced Materials* 24.4 (2012), pp. 503–508.
- [106] D. Monroe. “Hopping in exponential band tails”. In: *Physical Review Letters* 54.2 (1985), pp. 146–149.
- [107] N. F. Mott and R. W. Gurney. *Electronic Processes in Ionic Crystals*. Clarendon Press: New York, 1940.

- [108] D. Mühlbacher, M. Scharber, M. Morana, Z. Zhu, D. Waller, R. Gaudiana, and C. Brabec. “High photovoltaic performance of a low-bandgap polymer”. In: *Advanced Materials* 18.21 (2006), pp. 2884–2889.
- [109] C. Müller, M. Aghamohammadi, S. Himmelberger, P. Sonar, M. Garriga, A. Salleo, and M. Campoy-Quiles. “One-step macroscopic alignment of conjugated polymer systems by epitaxial crystallization during spin-coating”. In: *Advanced Functional Materials* 23.19 (2013), pp. 2368–2377.
- [110] P. K. Nayak, R. Rosenberg, L. Barnea-Nehoshtan, and D. Cahen. “O₂ and organic semiconductors: Electronic effects”. In: *Organic Electronics* 14.3 (2013), pp. 966–972.
- [111] H. T. Nicolai, M. M. Mandoc, and P. W. M. Blom. “Electron traps in semiconducting polymers: Exponential versus Gaussian trap distribution”. In: *Physical Review B - Condensed Matter and Materials Physics* 83.19 (2011), p. 195204.
- [112] H. T. Nicolai, M. Kuik, G. A. H. Wetzelaer, B. De Boer, C. Campbell, C. Risko, J. L. Bredas, and P. W. M. Blom. “Unification of trap-limited electron transport in semiconducting polymers”. In: *Nature Materials* 11.10 (2012), pp. 882–887.
- [113] V. R. Nikitenko, A. Kadashchuk, R. Schmechel, H. Von Seggern, and Y. Korosko. “Effect of dispersive transport and partial trap filling on thermally stimulated current in conjugated polymers”. In: *Journal of Applied Physics* 98.10 (2005), p. 103702.
- [114] M. Nikolka. “A perspective on overcoming water-related stability challenges in molecular and hybrid semiconductors”. English. In: *MRS Communications* (2019).
- [115] M. Nikolka, G. Schweicher, J. Armitage, I. Nasrallah, C. Jellett, Z. Guo, M. Hurhangee, A. Sadhanala, I. McCulloch, C. B. Nielsen, and H. Sirringhaus. “Performance Improvements in Conjugated Polymer Devices by Removal of Water-Induced Traps”. In: *Advanced Materials* 30.36 (2018), p. 1801874.
- [116] J. O. Oelerich, D. Huemmer, and S. D. Baranovskii. “How to find out the density of states in disordered organic semiconductors”. In: *Physical Review Letters* 108.22 (2012), p. 226403.
- [117] O. Ostroverkhova. “Organic Optoelectronic Materials: Mechanisms and Applications”. In: *Chemical reviews* 116.22 (2016), pp. 13279–13412.

- [118] G. Paasch and S. Scheinert. “Charge carrier density of organics with Gaussian density of states: Analytical approximation for the Gauss-Fermi integral”. In: *Journal of Applied Physics* 107.10 (2010), p. 104501.
- [119] G. Paasch and S. Scheinert. “Space charge layers in organic field-effect transistors with Gaussian or exponential semiconductor density of states”. In: *Journal of Applied Physics* 101.2 (2007).
- [120] G. Paasch and S. Scheinert. “Space-charge-limited currents in organics with trap distributions: Analytical approximations versus numerical simulation”. In: *Journal of Applied Physics* 106.8 (2009), p. 084502.
- [121] F. Padinger, R. S. Rittberger, and N. S. Sariciftci. “Effects of postproduction treatment on plastic solar cells”. In: *Advanced Functional Materials* 13.1 (2003), pp. 85–88.
- [122] C. K. Pandey, M. Bajpai, R. Srivastava, R. Malik, G. P. Shukla, A. K. Katiyar, B. Narayan, and R. Dhar. “Effect of n-type doping on the electron transport of polyfluorene”. In: *AIP Conference Proceedings*. Vol. 2050. 2018.
- [123] V. Podzorov, E. Menard, J. A. Rogers, and M. E. Gershenson. “Hall Effect in the Accumulation Layers on the Surface of Organic Semiconductors”. In: *Phys. Rev. Lett.* 95.22 (2005), p. 226601.
- [124] C. Poelking, K. Daoulas, A. Troisi, and D. Andrienko. *Morphology and charge transport in P3HT: A theorist’s perspective*. Vol. 265. Advances in Polymer Science. 2014, pp. 139–180.
- [125] S. Raj Mohan, M. P. Joshi, C. Shalu, C. Ghosh, C. Mukharjee, and L. M. Kukreja. “Charge transport properties of MDMO PPV thin films cast in different solvents”. In: *Journal of Polymer Science, Part B: Polymer Physics* 53.20 (2015), pp. 1431–1439.
- [126] S. Rangan, A. Batarseh, K. P. Chitre, A. Kopecky, E. Galoppini, and R. A. Bartynski. “Tuning Energy Level Alignment At Organic/Semiconductor Interfaces Using a Built-In Dipole in Chromophore–Bridge–Anchor Compounds”. In: *The Journal of Physical Chemistry C* 118.24 (2014), pp. 12923–12928.
- [127] E. H. Rhoderick. “The physics of Schottky barriers”. In: *Journal of Physics D: Applied Physics* 3.8 (1970), pp. 1153–1167.

- [128] I. Riedel, E. Von Hauff, J. Parisi, N. Martín, F. Giacalone, and V. Dyakonov. “Diphenylmethanofullerenes: New and efficient acceptors in bulk-heterojunction solar cells”. In: *Advanced Functional Materials* 15.12 (2005), pp. 1979–1987.
- [129] J. A. Röhr, T. Kirchartz, and J. Nelson. “On the correct interpretation of the low voltage regime in intrinsic single-carrier devices”. In: *Journal of Physics Condensed Matter* 29.20 (2017), p. 205901.
- [130] J. A. Röhr, D. Moia, S. A. Haque, T. Kirchartz, and J. Nelson. “Exploring the validity and limitations of the Mott-Gurney law for charge-carrier mobility determination of semiconducting thin-films”. In: *Journal of Physics Condensed Matter* 30.10 (2018), p. 105901.
- [131] Y. Roichman and N. Tessler. “Generalized Einstein relation for disordered semiconductors - Implications for device performance”. In: *Applied Physics Letters* 80.11 (2002), pp. 1948–1950.
- [132] K. Rojek, R. Schmechel, and N. Benson. “MIS-TSC: A combination of the thermally stimulated current method and a metal-insulator-semiconductor device for unipolar trap spectroscopy”. In: *Applied Physics Letters* 114.15 (2019), p. 152104.
- [133] K. Rojek, R. Schmechel, and N. Benson. “Ultra-fast measurement circuit for transient space charge limited current in organic semiconductor thin films”. In: *Measurement Science and Technology* 31 (2020), p. 015901.
- [134] S. Sahu and A. J. Pal. “Multifunctionality of organic devices: Light emission, photovoltage generation, and photodetection”. In: *Journal of Physical Chemistry C* 112.22 (2008), pp. 8446–8451.
- [135] C. Scharsich, F. S. U. Fischer, K. Wilma, R. Hildner, S. Ludwigs, and A. Köhler. “Revealing structure formation in PCPDTBT by optical spectroscopy”. In: *Journal of Polymer Science, Part B: Polymer Physics* 53.20 (2015), pp. 1416–1430.
- [136] H. Scher and E. W. Montroll. “Anomalous transit-time dispersion in amorphous solids”. In: *Physical Review B* 12.6 (1975), pp. 2455–2477.
- [137] R. B. Schilling and H. Schachter. “Oscillatory modes associated with one carrier transient space-charge-limited currents”. In: *Journal of Applied Physics* 38.4 (1967), pp. 1643–1646.
- [138] R. Schmechel and H. Von Seggern. “Electronic traps in organic transport layers”. In: *Physica Status Solidi (A) Applied Research* 201.6 (2004), pp. 1215–1235.

- [139] G. Schweicher, G. Garbay, R. Jouclas, F. Vibert, F. Devaux, and Y. H. Geerts. “Molecular Semiconductors for Logic Operations: Dead-End or Bright Future?” In: *Advanced Materials* (2020), p. 1905909.
- [140] A. Seemann, T. Sauermann, C. Lungenschmied, O. Armbruster, S. Bauer, H. Egelhaaf, and J. Hauch. “Reversible and irreversible degradation of organic solar cell performance by oxygen”. In: *Solar Energy* 85.6 (2011), pp. 1238–1249.
- [141] R. C. Shallcross, T. Stubhan, E. L. Ratcliff, A. Kahn, C. J. Brabec, and N. R. Armstrong. “Quantifying the extent of contact doping at the interface between high work function electrical contacts and poly(3-hexylthiophene) (P3HT)”. In: *Journal of Physical Chemistry Letters* 6.8 (2015), pp. 1303–1309.
- [142] Y. Shirota and H. Kageyama. “Charge Carrier Transporting Molecular Materials and Their Applications in Devices”. In: *Chemical Reviews* 107.4 (2007), pp. 953–1010.
- [143] S. Shoaee and J. R. Durrant. “Oxygen diffusion dynamics in organic semiconductor films”. In: *Journal of Materials Chemistry C* 3.39 (2015), pp. 10079–10084.
- [144] M. Silver, P. Mark, D. Olness, W. Helfrich, and R. C. Jarnagin. “On the Observation of Transient Space-Charge-Limited Currents in Insulators”. In: *Journal of Applied Physics* 33.10 (1962), pp. 2988–2991.
- [145] S. K. So, S. C. Tse, and K. L. Tong. “Charge Transport and Injection to Phenylamine-Based Hole Transporters for OLEDs Applications”. In: *Journal of Display Technology* 3.2 (2007), pp. 225–232.
- [146] S. K. So, W. K. Choi, C. H. Cheng, L. M. Leung, and C. F. Kwong. “Surface preparation and characterization of indium tin oxide substrates for organic electroluminescent devices”. In: *Applied Physics A: Materials Science and Processing* 68.4 (1999), pp. 447–450.
- [147] Q. L. Song, F. Y. Li, H. Yang, H. R. Wu, X. Z. Wang, W. Zhou, J. M. Zhao, X. M. Ding, C. H. Huang, and X. Y. Hou. “Small-molecule organic solar cells with improved stability”. In: *Chemical Physics Letters* 416.1-3 (2005), pp. 42–46.
- [148] A. Y. Sosorev, D. R. Maslennikov, O. G. Kharlanov, I. Y. Chernyshov, V. V. Bruevich, and D. Y. Paraschuk. “Impact of Low-Frequency Vibrations on Charge Transport in High-Mobility Organic Semiconductors”. In: *Physica Status Solidi - Rapid Research Letters* 13.3 (2019), p. 1800485.

- [149] J. F. P. Souza, J. P. M. Serbena, E. L. Kowalski, and L. C. Akcelrud. “Determination of P3HT Trap Site Energies by Thermally Stimulated Current”. In: *Journal of Electronic Materials* 47.2 (2018), pp. 1611–1619.
- [150] J. Steiger, R. Schmechel, and H. Von Seggern. “Energetic trap distributions in organic semiconductors”. In: *Synthetic Metals* 129.1 (2002), pp. 1–7.
- [151] L. Sun, J. Sun, C. Xiong, and X. Shi. “Trap-assisted recombination in disordered organic semiconductors extended by considering density dependent mobility”. In: *Solar Energy* 135 (2016), pp. 308–316.
- [152] S. M. Sze and K. K. Ng. *Physics of Semiconductor Devices*. Wiley-VCH Verlag & Co. KGaA, 2012.
- [153] M. Z. Szymanski, I. Kulszewicz-Bajer, J. Faure-Vincent, and D. Djurado. “Comparison of simulations to experiment for a detailed analysis of space-charge-limited transient current measurements in organic semiconductors”. In: *Physical Review B - Condensed Matter and Materials Physics* 85.19 (2012), p. 105205.
- [154] M. Z. Szymanski, B. Luszczynska, J.-M. Verilhac, P. Reiss, and D. Djurado. “Simplified transient space-charge-limited current measurements of mobility using transimpedance amplifier”. In: *Organic Electronics* 14.1 (2013), pp. 230 – 235.
- [155] H. Tamura, A. Tanaka, K. Mita, and R. Furuichi. “Surface hydroxyl site densities on metal oxides as a measure for the ion-exchange capacity”. In: *Journal of colloid and interface science* 209.1 (1999), pp. 225–231.
- [156] N. Tessler, Y. Preezant, N. Rappaport, and Y. Roichman. “Charge transport in disordered organic materials and its relevance to thin-film devices: A tutorial review”. In: *Advanced Materials* 21.27 (2009), pp. 2741–2761.
- [157] A. K. Thakur, A. K. Mukherjee, D. M. G. Preethichandra, W. Takashima, and K. Kaneto. “Charge injection mechanism across the Au-poly(3-hexylthiophene-2,5-diyl) interface”. In: *Journal of Applied Physics* 101.10 (2007), p. 104508.
- [158] N. Thejokalyani and S. J. Dhoble. “Novel approaches for energy efficient solid state lighting by RGB organic light emitting diodes - A review”. In: *Renewable and Sustainable Energy Reviews* 32 (2014), pp. 448–467.
- [159] K. Tsai, T. Guo, A. K. Jen, and T. Wen. “Role of self-assembled tetraoctylammonium bromide on various conjugated polymers in polymer light-emitting diodes”. In: *Journal of Materials Chemistry C* 2.2 (2014), pp. 272–276.

- [160] M.-J. Tsai and H.-F. Meng. “Electron traps in organic light-emitting diodes”. In: *Journal of Applied Physics* 97.11 (2005), p. 114502.
- [161] V. Turkovic, S. Engmann, D. A. M. Egbe, M. Himmerlich, S. Krischok, G. Gobsch, and H. Hoppe. “Multiple stress degradation analysis of the active layer in organic photovoltaics”. In: *Solar Energy Materials and Solar Cells* 120.PART B (2014), pp. 654–668.
- [162] R. A. Vaia, B. B. Sauer, O. K. Tse, and E. P. Giannelis. “Relaxations of confined chains in polymer nanocomposites: Glass transition properties of poly(ethylene oxide) intercalated in montmorillonite”. In: *Journal of Polymer Science, Part B: Polymer Physics* 35.1 (1997), pp. 59–67.
- [163] M. Valadares, I. Silvestre, H. D. R. Calado, B. R. A. Neves, P. S. S. Guimarães, and L. A. Cury. “BEHP-PPV and P3HT blends for light emitting devices”. In: *Materials Science and Engineering C* 29.2 (2009), pp. 571–574.
- [164] S. L. M. Van Mensfoort and R. Coehoorn. “Effect of Gaussian disorder on the voltage dependence of the current density in sandwich-type devices based on organic semiconductors”. In: *Physical Review B - Condensed Matter and Materials Physics* 78.8 (2008), p. 085207.
- [165] S. L. M. Van Mensfoort, S. I. E. Vulto, R. A. J. Janssen, and R. Coehoorn. “Hole transport in polyfluorene-based sandwich-type devices: Quantitative analysis of the role of energetic disorder”. In: *Physical Review B - Condensed Matter and Materials Physics* 78.8 (2008), p. 085208.
- [166] P. Vigneshwara Raja and N. V. L. Narasimha Murty. “Thermally stimulated capacitance in gamma irradiated epitaxial 4H-SiC Schottky barrier diodes”. In: *Journal of Applied Physics* 123.16 (2018), p. 161536.
- [167] N. Von Malm, R. Schmechel, and H. Von Seggern. “Distribution of occupied states in doped organic hole transport materials”. In: *Synthetic Metals* 126.1 (2002), pp. 87–95.
- [168] N. Von Malm, J. Steiger, R. Schmechel, and H. Von Seggern. “Trap engineering in organic hole transport materials”. In: *Journal of Applied Physics* 89.10 (2001), pp. 5559–5563.
- [169] Y. Wang, F. Teng, Q. Zhou, and Y. Wang. “Multiple roles of bathocuproine employed as a buffer-layer in organic light-emitting diodes”. In: *Applied Surface Science* 252.6 (2006), pp. 2355–2359.

- [170] Z. Wang, M. A. Kamarudin, N. C. Huey, F. Yang, M. Pandey, G. Kapil, T. Ma, and S. Hayase. “Interfacial Sulfur Functionalization Anchoring SnO₂ and CH₃NH₃PbI₃ for Enhanced Stability and Trap Passivation in Perovskite Solar Cells”. In: *ChemSusChem* 11.22 (2018), pp. 3941–3948.
- [171] O. J. Weiß, R. K. Krause, and A. Hunze. “Hole mobility of 1-NaphDATA”. In: *Journal of Applied Physics* 103.4 (2008), p. 043709.
- [172] U. Wolf, V. I. Arkhipov, and H. Bässler. “Current injection from a metal to a disordered hopping system. I. Monte Carlo simulation”. In: *Phys. Rev. B* 59 (11 1999), pp. 7507–7513.
- [173] J. Yan and B. R. Saunders. “Third-generation solar cells: a review and comparison of polymer:fullerene, hybrid polymer and perovskite solar cells”. In: *RSC Advances* 4 (2014), pp. 43286–43314.
- [174] X. Yan, B. Chu, W. Li, Z. Su, T. Zhang, F. Jin, B. Zhao, F. Zhang, D. Fan, Y. Gao, T. Tsuboi, J. Wang, H. Pi, and J. Zhu. “Improved photovoltaic characteristics of organic cells with heterointerface layer as a hole-extraction layer inserted between ITO anode and donor layer”. In: *Organic Electronics: physics, materials, applications* 14.7 (2013), pp. 1805–1810.
- [175] J. Yang, F. Bussolotti, S. Kera, and N. Ueno. “Origin and role of gap states in organic semiconductor studied by UPS: As the nature of organic molecular crystals”. In: *Journal of Physics D: Applied Physics* 50.42 (2017), p. 423002.
- [176] H. Yi, S. Al-Faifi, A. Iraqi, D. C. Watters, J. Kingsley, and D. G. Lidzey. “Carbazole and thienyl benzo[1,2,5]thiadiazole based polymers with improved open circuit voltages and processability for application in solar cells”. In: *Journal of Materials Chemistry* 21.35 (2011), pp. 13649–13656.
- [177] T. Yildirim, N. M. Gasanly, and S. Tüzemen. “Characterization of defect states in Ga-rich gallium arsenide crystals by thermally stimulated current”. In: *Iranian Journal of Science and Technology, Transaction A: Science* 42.2 (2018), pp. 947–950.
- [178] C. Yu, T. Jen, and S. Chen. “Traps in regioregular poly(3-hexylthiophene) and its blend with [6,6]-Phenyl-C61-butyric acid methyl ester for polymer solar cells”. In: *ACS Applied Materials and Interfaces* 5.10 (2013), pp. 4086–4092.

- [179] Y. Zhang, B. De Boer, and P. W. M. Blom. “Trap-free electron transport in poly (p-phenylene vinylene) by deactivation of traps with n -type doping”. In: *Physical Review B - Condensed Matter and Materials Physics* 81.8 (2010), p. 085201.
- [180] Y. Zheng, A. T. S. Wee, C. Troadec, and N. Chandrasekhar. “Temperature-dependent transition from injection-limited to space-charge-limited current in metal-organic diodes”. In: *Applied Physics Letters* 95.14 (2009), p. 143303.
- [181] J. Zhu, F. Bebensee, W. Hieringer, W. Zhao, J. H. Baricuatro, J. A. Farmer, Y. Bai, H. Steinrück, J. M. Gottfried, and C. T. Campbell. “Formation of the calcium/poly(3-hexylthiophene) interface: Structure and energetics”. In: *Journal of the American Chemical Society* 131.37 (2009), pp. 13498–13507.
- [182] M. Zubair, Y. S. Ang, and L. K. Ang. “Thickness Dependence of Space-Charge-Limited Current in Spatially Disordered Organic Semiconductors”. In: *IEEE Transactions on Electron Devices* 65.8 (2018), pp. 3421–3429.
- [183] G. Zuo, M. Linares, T. Upreti, and M. Kemerik. “General rule for the energy of water-induced traps in organic semiconductors”. In: *Nature Materials* 18.6 (2019), pp. 588–593.

DuEPublico

Duisburg-Essen Publications online

UNIVERSITÄT
DUISBURG
ESSEN

Offen im Denken

ub | universitäts
bibliothek

Diese Dissertation wird via DuEPublico, dem Dokumenten- und Publikationsserver der Universität Duisburg-Essen, zur Verfügung gestellt und liegt auch als Print-Version vor.

DOI: 10.17185/duepublico/75262

URN: urn:nbn:de:hbz:464-20220118-145549-9

Alle Rechte vorbehalten.